X-CME: Integrating Flux-Rope Reconstruction Techniques into ICME Propagation Forecasting

NASA Goddard Space Flight Center

Heliophysics Science Division (HSD)

Universitat Politècnica de Catalunya

Degree in Aerospace Engineering & Engineering Physics

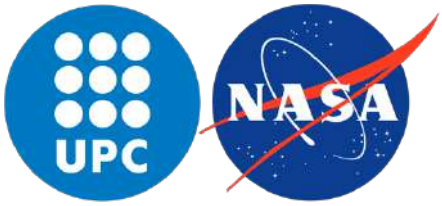

Martí Massó Moreno

Bachelor's Thesis

Supervisor (NASA GSFC): Teresa Nieves Chinchilla

Co-supervisor (UPC ETSETB): Jordi José Pont

May 2025

"Thoroughly conscious ignorance is the prelude to every real advance in science."

James Clerk Maxwell (1831–1879)

Abstract

English: Coronal mass ejections (CMEs) are considered one of the most aggressive events occurring daily in the solar system. Although Earth possesses a magnetosphere that shields us, we still experience their effects, making it crucial to predict their propagation before they reach our planet. This study proposes a new methodology to forecast how these ejections will propagate, based on in situ data detected by satellites in the interplanetary medium. The software used to carry out these studies is called X-CME, and it is currently undergoing validation by the NASA Goddard Space Weather Department, yielding so far satisfactory results and an error tolerance less than half of what had been achieved to date. Throughout this document, the methodology followed during the entire process will be detailed, as well as its application with real data for validation.

Català: Les emissions de massa coronal (CMEs) són considerades uns dels esdeveniments més agressius que es produeixen diàriament al sistema solar. Tot i que la Terra compta amb una magnetosfera que ens protegeix, en seguim notant els efectes, cosa que fa que sigui crucial poder predir-ne la propagació abans que arribin al nostre planeta. En aquest treball es proposa una nova metodologia per predir com es propagaran aquestes emissions, basant-se en dades in situ detectades per satèl·lits en el medi interplanetari. El programa en què es duen a terme aquests estudis s'ha batejat com X-CME, i actualment es troba en fase de validació pel Departament de Space Weather de la NASA Goddard, amb resultats de moment satisfactoris i una tolerància d'error inferior a la meitat de la que es registrava fins ara. Al llarg d'aquest document es detallarà quina ha estat la metodologia seguida durant tot el procés, així com la seva aplicació amb dades reals per a la seva validació.

Castellano: Las eyecciones de masa coronal (CMEs) son consideradas unos de los eventos más agresivos que se producen diariamente en el sistema solar. Aunque en la Tierra contemos con una magnetosfera que nos protege, seguimos percibiendo sus efectos, por lo que resulta crucial poder predecir su propagación antes de que alcancen nuestro planeta. En este trabajo se propone una nueva metodología para predecir cómo se propagarán dichas emisiones, basándose en datos in situ detectados por satélites en el medio interplanetario. El programa en el que se llevan a cabo estos estudios se ha bautizado como X-CME, y actualmente se encuentra en fase de validación por el Departamento de Space Weather de NASA Goddard, con resultados de momento satisfactorios y una tolerancia de error inferior a la mitad de la que se registraba hasta la fecha. A lo largo de este documento se detallará cuál ha sido la metodología seguida durante todo el proceso, así como su aplicación con datos reales para su validación.

Keywords— coronal mass ejections, CME propagation, magnetic flux-rope modeling, in situ data analysis, space-weather prediction, solar-wind drag

Paraules Clau— emissions de massa coronal, propagació de CMEs, modelatge de cordes de flux magnètic, dades in situ, predicció meteorològica espacial, arrossegament del vent solar

Palabras Clave— eyecciones de masa coronal, propagación de CMEs, modelado de cuerdas de flujo magnético, datos in situ, predicción meteorológica espacial, arrastre del viento solar

Acknowledgements

I would first like to express my sincere gratitude to Teresa Nieves Chinchilla for welcoming me this year at NASA Goddard and allowing me to carry out this project under her guidance, as well as for introducing me into the LASSOS group and making me feel like a valued and integrated member of this research team.

I also wish to convey my deep appreciation to Laura Balmaceda for her constant interest and support in my project, and for her ongoing supervision of my work. My thanks also go to Ayris Narock, Andreas Weiss, and Carlos Arturo for their valuable advice and shared expertise during the execution of my research.

Furthermore, I am profoundly grateful to the CFIS Mobility Program for the partial funding of this research work, particularly Fundació Privada Mir-Puig, CFIS partners, and donors of the crowdfunding program for giving me the opportunity to pursue the studies I wanted and for providing the financial support through the Mobility Program that made this stay in the U.S. possible. In particular, I thank Toni Pascual for navigating the countless procedures required for entry into NASA, and Miguel Ángel Barja and Juan José Rue Perna for their excellent leadership of this program. I also extend my heartfelt thanks to UPC and to Jordi José Pont for agreeing to serve as my mentor for this work.

I would like to give special thanks to Jesús Navas for his constant support and camaraderie throughout this project, as well as for the insightful discussions that were fundamental to its progress, and to Anastasis Anastasiadis for making this stay at NASA a more personable and welcoming experience.

Finally, I offer enormous gratitude to my family and friends for being present in spirit, even from across the ocean. Without all of you, none of this would have been possible. I am immensely thankful.

Contents

Introduction

The field of Space Weather has become increasingly important in recent decades, driven by a surge in space missions. With crewed voyages to Mars on the horizon, accurate forecasts of interplanetary conditions will be critical. Although the Sun produces a variety of phenomena, this work focuses on one of the most significant: coronal mass ejections (CMEs). These massive eruptions of magnetized plasma travel through space and, upon reaching Earth, can trigger severe geomagnetic storms, disrupting satellite electronics and posing risks to astronauts aboard the ISS.

Until now, CME-propagation forecasts have depended mainly on coronagraph observations which record eruptions as they exit the low solar corona region. Nonetheless, initial speed and direction measurements from the Sun lead to substantial timing errors of approximately 13.2 hours on average [8] because small uncertainties near the Sun grow significantly during the 1 AU journey.

This research presents a different forecasting method. The Flux-Rope model enables us to determine the CME internal magnetic structure and physical parameters through in-situ spacecraft measurements that operate between the Sun and Earth. The local solution gets embedded into a new global CME framework to solve its complete propagation dynamics for determining Earth or Mars orbit intersection times.

The program created to carry out these studies has been named X-CME, and is currently under the validation phase in the Space Weather department at NASA Goddard, to verify its accuracy and its operational functionality.

This first version of X-CME includes classical models for the definition of the interplanetary medium, as well as a geometry that is not overly complex for modeling the magnetic structure. The results obtained to date have been good, yielding predictions with errors on the order of between 1 h and 4 h; however, there is still much work ahead to continue refining the physical models and updating them based on new discoveries in this field.

1 . Coronal Mass Ejections

1.1 General properties of our Sun

In astronomy, stellar classification typically groups stars based on their spectral characteristics. This allows for the determination of the temperature of their photosphere and the abundance of ions in their atmosphere. According to the Morgan–Keenan (MK) system, the Sun is classified as a G2–V star, indicating that it is a main-sequence star ("V") with a spectral type "G2." This classifies it as a yellow dwarf with an effective temperature of approximately 5800 K, and a mass and radius very close to the solar unit [9].

Specifically, the Sun has a mass of approximately $M_\odot \approx 1.99 \cdot 10^{30}$ kg, a radius of $R_\odot \approx 6.96 \cdot 10^8$ m, and a luminosity of $L_\odot \approx 3.83 \cdot 10^{26}$ W. It is primarily composed of hydrogen ($\sim 74\%$ by mass) and helium ($\sim 24\%$), with the remaining $\sim 2\%$ consisting of heavier elements ("metals"). The Sun formed approximately 4.6 billion years ago. Since then, it has been fusing on the order of 600 billion kg of hydrogen in its interior every second [35], which can be approximated as consuming the equivalent in mass to Mount Everest every hour (see Appendix A).

The Sun does not have a well-defined boundary as such, but its density decreases exponentially with increasing altitude above the photosphere [35]. However, it is not until reaching one of the outermost layers of the atmosphere (the lower solar corona) that coronal mass emissions will be generated. The layers that make up the structure of our Sun will be explained in more detail below.

1.1.1 Structure of the Sun

The Sun is composed of a series of concentric layers in which energy is generated, transported and ultimately expelled into space. Inside, the high pressure and temperature due to gravity generate nuclear fusion in its core. The generated energy travels outwards through the radiative and convective zones. Then, in the atmosphere, this energy is expressed as heat, reaching over a million degrees in the corona, where coronal mass emissions will take place and where the solar wind will be born.

Solar Interior

- ◇ **Core**: This is the central region of the Sun, where nuclear fusion transforms hydrogen into helium. The temperature in this region is approximately 15M ^{o}C, and it has a density of about $150 g/cm^3$, about 10 times that of gold. It extends to approximately 25% of the distance to the surface, and after that fusion practically ceases and density and temperature drop drastically.
- ◇ **Radiative Zone**: This zone extends from the end of the core to approximately 0.7 R_s. It is called this because the characteristic method of energy transport in this region is radiation. The density goes from $20 g/cm^3$ after the core to only $0.2 g/cm^3$ at the end of this region. The temperature decreases throughout this region from 7,000,000^{o}C to about 2,000,000^{o}C.
- ◇ **Convection Zone**: The outermost layer of the solar interior is the convection zone, so named also for its primary method of energy transport. Convection occurs due to internal temperature gradients. This transport mechanism is relatively fast. The fluid expands and cools rapidly, reaching temperatures of about 5700K at the surface. In this region, the density is only about $0.0000002\, g/cm^3$. [6]

Solar Atmosphere

- ◇ **Photosphere**: Represents the deepest solar layer which extends from the visible solar surface up to 400 kilometers. The base of the photosphere reaches temperatures of 6 500 K while the top reaches 4 000 K and its grainy appearance emerges from convective cells known as granules.
- ◇ **Chromosphere**: The chromosphere exists between 400 km and 2 100 km above the photosphere. The temperature rises from 4 000 K at the base to 8 000 K at the top of this region which produces spicules and spectral emission lines.
- ◇ **Corona**: The outermost faintly glowing envelope of the Sun extends from 2 100 km above the photosphere all the way into interplanetary space. The temperature rises to several hundred thousand kelvins and reaches a few million degrees in this region which produces coronal mass ejections and accelerates the solar wind.

Below is a schematic of the different regions explained above, and how the coronal mass emissions can be seen.

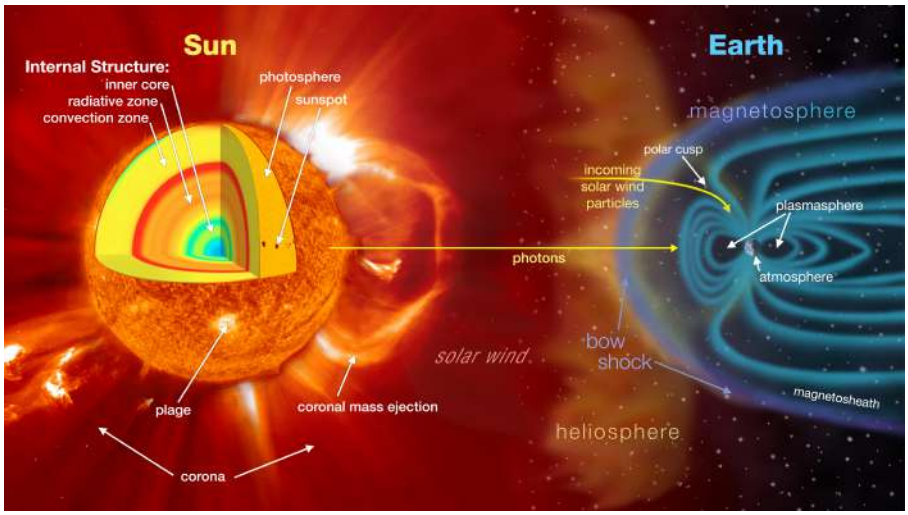

Figure 1.1: Earth-Sun System [1]

In this next section we will explain in more detail what CMEs are and how they are detected in the interplanetary medium.

1.2 Solar Wind and Coronal Mass Ejections

Coronal mass ejections (CMEs) are large expulsions of plasma and magnetic field from the solar corona. A single CME can release billions of tonnes of material and carries an embedded magnetic field significantly stronger than the background interplanetary magnetic field (IMF). CME speeds range from 250 km/s to 3 000 km/s, so the fastest events may reach Earth in as little as 15–18 h, whereas slower CMEs can take several days to arrive [23].

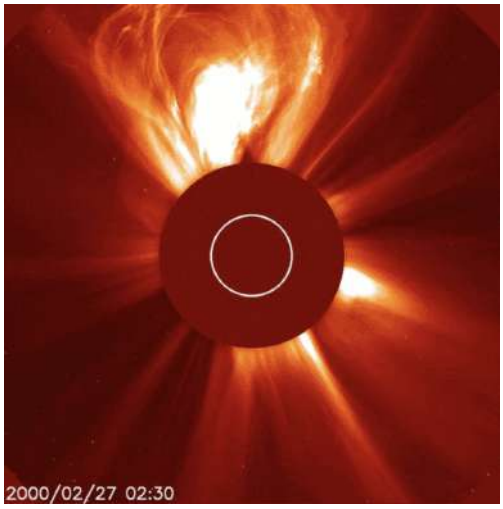

(a) Coronagraph during a CME, captured by SOHO.[16]

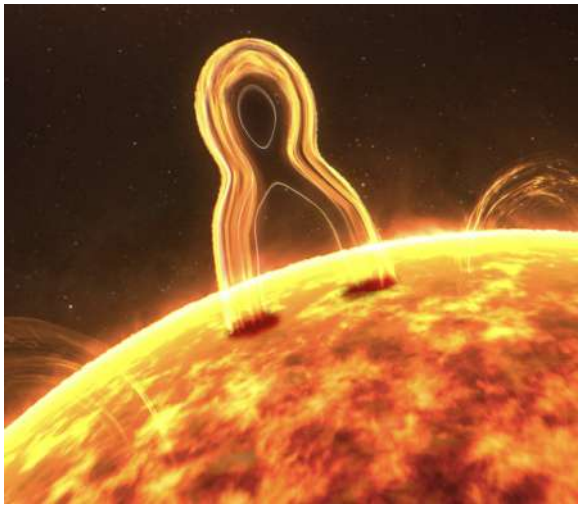

(b) Magnetic reconnection of a flux rope at the solar surface.

Figure 1.2: Generation of CMEs: observation (a) and modeling (b).

Viewed through a coronagraph, CMEs appear as bright, loop-shaped ejections much larger than

the quiescent corona.

As CMEs travel through the interplanetary medium, they expand to sizes of order 0.25 AU by the time they reach Earth. In the second part of this project, we will study how these structures propagate through the interplanetary medium and how their volume increases in the process.

1.2.1 Formation in the Corona

CMEs generally originate when highly twisted magnetic flux-rope structures in the low corona become unstable and undergo magnetic reconnection. This reconnection releases a burst of electromagnetic energy as a solar flare, typically accompanied by the rapid ejection of plasma (the CME). Such eruptions often occur in cool, dense active regions—visible as sunspots—where the magnetic field is strongest [24].

Figure 1.3 shows three typical solar diagnostics. The HMI magnetogram measures Zeeman splitting of the Fe I line at 617.3 nm, revealing field strength. The HMI continuum (∼617 nm) highlights sunspots in the photosphere. The AIA 193 Å channel images hot coronal loops, diffuse active regions, and bright arches above the photosphere. Together, these views locate eruption sites and correlate magnetic and thermal structures.

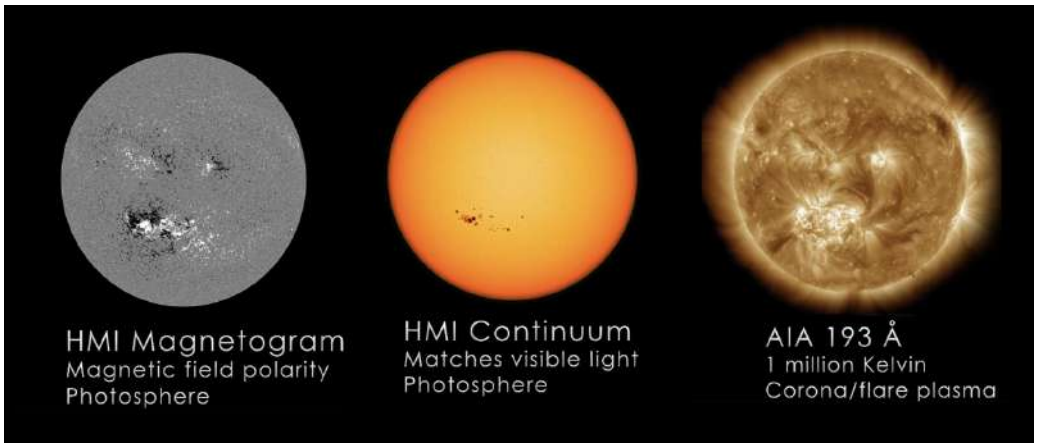

Figure 1.3: Multi-wavelength SDO view of the Sun: (a) HMI magnetogram of photospheric magnetic polarity, (b) HMI visible-light continuum, and (c) AIA 193 Å extreme-UV image of 1 MK coronal plasma.

Based on coronagraph observations, SWPC forecasters use CME size, speed and direction (typically from SOHO and STEREO-A) to estimate Earth-impact probability. However, only ∼10 % of such forecasts have corresponded to in-situ detections at Earth, due to limited viewing angles and early-stage data.

1.2.2 Propagation of CMEs

Tracking CME propagation in the interplanetary medium is challenging because only partial structures are observed; in-situ, they appear as magnetic perturbations. The DSCOVR spacecraft at L1 provides real-time warnings: a disturbance detected there will impact Earth within 15–60 minutes. However, this short reaction time ($\leq$1 h) limits preparedness and cannot be generalized to other targets.

On the other hand, the most frequently used method for tracking CME propagation relies on coronagraph data. However, since these observations capture only the early stages of propagation, it is difficult to make accurate predictions at distances around 1 AU. This issue is discussed in detail in [8], where it is noted that in recent years, the average absolute error in such predictions has been around 13.2 hours.

The methodology developed in this work aims to offer an alternative approach to ICME prediction methods, now based on in-situ data detected by satellites located at intermediate positions between the Sun and the Earth. The goal is to resolve the propagation dynamics of the Interplanetary CME (ICME) in order to predict its arrival time at Earth. The tool presented in this work, named X-CME, shows promising results, with prediction errors as low as 1–4 hours for forecasts made 1 to 2 days in advance.

1.2.3 Magnetic Clouds and Flux Ropes

In interplanetary meteorology, *magnetic clouds* (MCs) and *flux ropes* (FRs) are key concepts. MCs are solar-wind structures defined by an initial shock, enhanced field strength, a smooth magnetic-field rotation, low proton temperature, and plasma $\beta < 1$. FRs denote the internal helical magnetic configuration of MCs, modeled as field lines wound around a central axis. Not all FRs qualify as MCs: MCs satisfy additional observational criteria. Both are associated with CMEs, with MCs forming a subset of ICMEs. This work focuses on in situ FR signatures, although all the events studied have previously been classified as MCs. Below is a schematic representation of an ICME with its leading shock and associated magnetic structure.

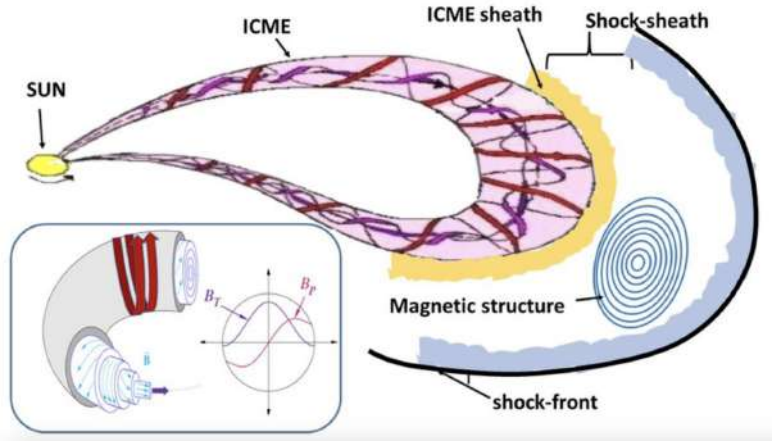

Figure 1.4: Schematic of an ICME, showing the shock front, sheath region, and internal flux-rope magnetic structure (with an embedded magnetic cloud).

The figure above illustrates the propagation of a CME through the interplanetary medium, showing a surrounding sheath (ICME sheath) and a shock front. It also depicts the internal magnetic structure, which exhibits the characteristic properties of a flux rope. [22, 27]

In this work, we will generally refer to the study of flux ropes, since we concentrate on the magnetic signatures detected. However, the events analyzed have all been previously classified as MCs based on additional plasma and thermal variables.

1.3 In-Situ detection of MOs and ICMEs

In the in situ data, the information provided is of the form showed in figure 1.5. Several parameters are distinguished in this example. The first panel shows the total magnetic-field magnitude measured at each instant. A black bar above indicates the full ICME interval, and a pink bar marks the Magnetic Obstacle (or magnetic cloud).

The first vertical line marks the ICME onset, where the interplanetary shock (IP shock) occurs. The two vertical green lines denote the start and end of the flux rope. [20]

The second panel displays the separate components of the magnetic field in the GSE coordinate system, in nT. Here one observes a smooth rotation, especially in the B_z component, indicative of a flux rope.

The next panel shows the proton density N_p in cm^{-3}. A strong perturbation is seen in the shock/sheath region, with a rapid rise followed by a drop upon entering the MO.

The proton thermal speed V_{th} decreases significantly inside the MO, indicating considerable cooling relative to the ambient solar wind. This is also reflected in the drop of β_p, which shows that magnetic pressure dominates over thermal pressure within the MO.

Another variable essential for our analysis is the solar-wind speed V_{sw}, which we observe to be

higher than the preceding ambient wind. This speed is assumed to be almost entirely in the radial propagation direction from the Sun, and it will help us not only determine the spatial dimensions of the observed magnetic structure, but also predict the subsequent propagation of the CME through the interplanetary medium.

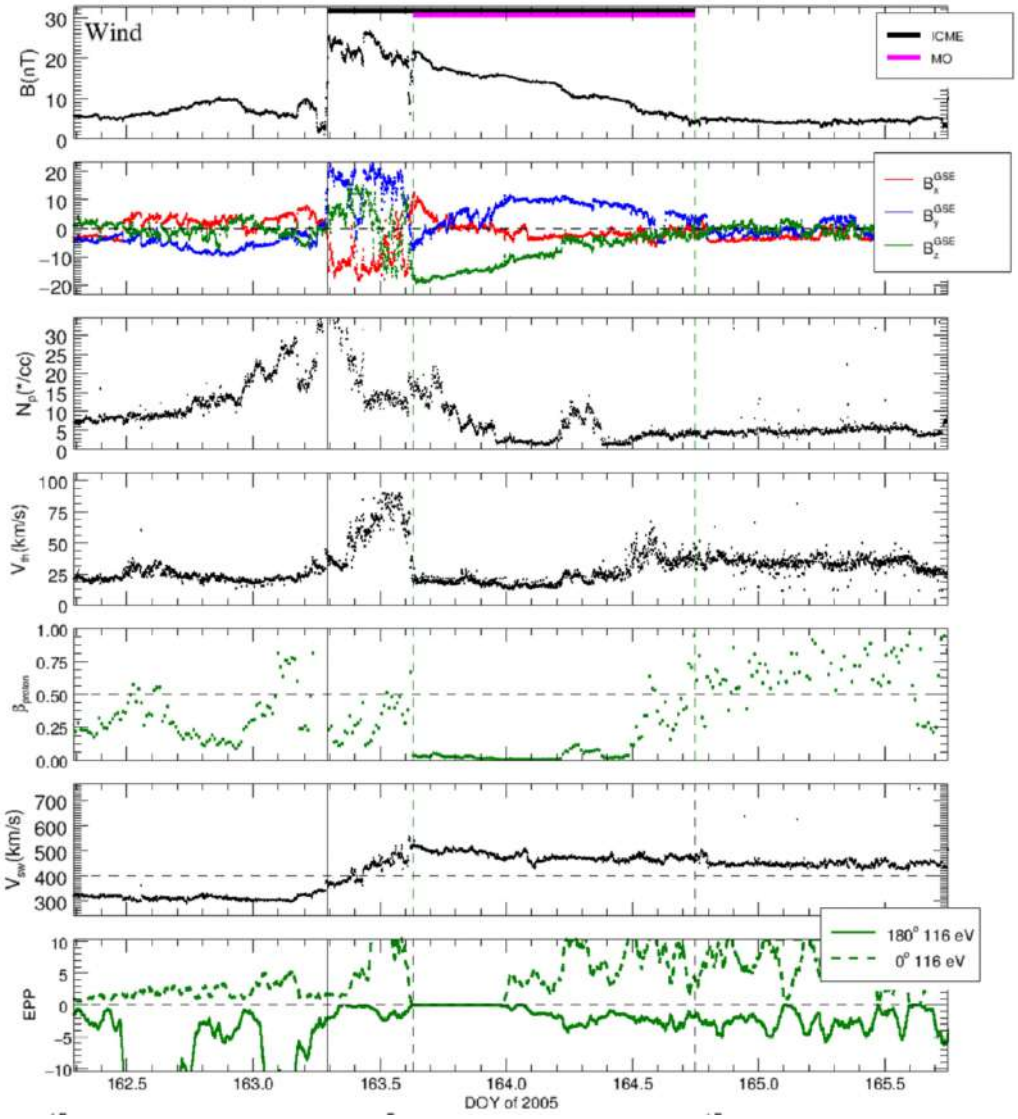

Figure 1.5: Wind spacecraft measurements for 2005/DOY 163–165. In situ ICME and MO detection [20].

Finally, the last parameter shown for this event is the electron pitch-angle distribution (EPP, at 116eV). A solid green line indicates the 180° flux, and a dashed line indicates the 0° flux. This variable is indicative of electron bidirectionality, revealing whether the internal flow is preferentially inbound or outbound along the flux-rope axis.

Altogether, the complete set of these parameters is used analytically to determine whether a given signature can be classified as an MO. For this work, however, we will not perform event detection and classification, but rather focus on the analysis of those events already identified as MOs.

The example shown was detected by the WIND probe, but there are several missions that carry out this type of in-situ detection.

1.3.1 Solar Orbiter

Solar Orbiter is an ESA mission with NASA contributions, launched on 10 February 2020. The spacecraft follows an elliptical orbit around the Sun which will reach a maximum tilt of 24° above the ecliptic plane. The combination of remote-sensing and in situ instruments on board enables the production of the most detailed Sun images (including polar region observations) while tracing solar wind sources on the solar surface [4, 32].

Figure 1.6: Solar Orbiter [5].

1.3.2 STEREO

STEREO consists of two identical spacecraft named STEREO-A and STEREO-B, launched on October 26 2006 into heliocentric orbits that move ahead of and behind Earth. This configuration enabled scientists to obtain the first-ever three-dimensional solar observations of coronal mass ejections as they move from the corona through interplanetary space [15, 33].

Figure 1.7: STEREO mission [7].

1.3.3 Parker Solar Probe

The Parker Solar Probe is by far the closest mission to the Sun's surface. NASA launched it the as a heliophysics mission on August 12th 2018. Through its carbon-composite heat shield and four instrument suites, this spacecraft enters the outer corona of the Sun to perform the first-ever direct measurement of stellar atmospheric properties for studying coronal heating and solar wind acceleration.

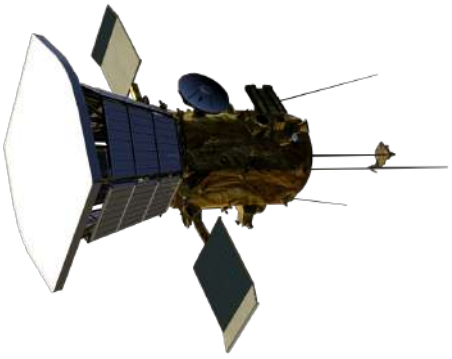

Figure 1.8: Parker Solar Probe [31].

1.3.4 WIND

Wind is a spin-stabilized NASA spacecraft launched on 1 November 1994 and placed into a halo orbit around the Sun–Earth L_1 Lagrange point. The spacecraft instruments analyze the unaltered solar wind plasma together with magnetic fields and high-energy particles which have not yet encountered Earth's magnetosphere [12, 14].

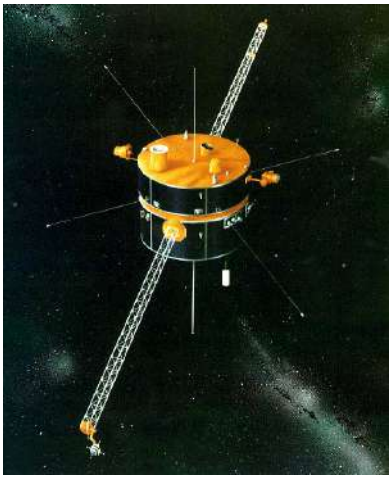

Figure 1.9: WIND [34].

2 . Modeling the Magnetic Field Configuration of CMEs

2.1 Historic background

The concept of “magnetic clouds” (MCs) emerged from space-based observations of smooth large-angle magnetic field rotations together with low proton temperature and enhanced field strength that followed CME-driven shocks. The term ”magnetic cloud” emerged in 1981 when Burlaga et al. observed these structures in the solar wind while noting their unique plasma characteristics [2].

The models used to explain these structures have developed progressively since their initial introduction. Goldstein in 1983 established that force-free flux ropes provided a suitable model for MCs because they satisfied the relation:

$$\nabla \times \mathbf{B} = \alpha \, \mathbf{B},$$

Lepping introduced the first automated least-squares fitting method in 1990 to match experimental data with analytic solutions for extracting the flux-rope radius and axial magnetic-field strength and impact parameter. [10]

Later, Hidalgo in 2002 proposed a more relaxed force-free assumption and introduced a model that did not require a force-free topology. However, the internal field description remained quite simplistic, and it was not until 2016 that Nieves-Chinchilla proposed a more general analytical form for the internal magnetic field within a circular-cylindrical flux-rope geometry.

2.2 Circular Cylindrical (CC) Model

The first model we will study is the Circular Cylindrical model without the *force-free* constraint, which means that the condition requiring the Lorentz forces to be always zero inside is not imposed. The scheme proposed by Nieves-Chinchilla in [17] is as follows:

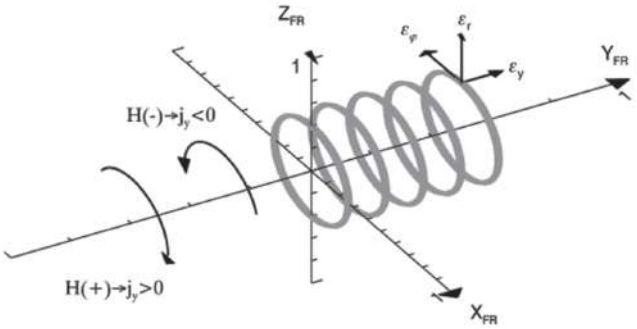

Figure 2.1: Circular Cylindrical Model of the Flux Rope – Retrieved from [18]

In this model, the magnetic field is assumed to be embedded in the shape of a cylinder, with a single sense of rotation of the poloidal component of the magnetic field, which will determine the chirality. The coordinate system used is cylindrical, with variables: (r, φ, y), where r is the radial distance from the cylinder axis, φ is the azimuthal angle, and y corresponds to the axial coordinate. The latter is taken as y instead of z as we might be accustomed to because in Geocentric Solar Ecliptic (GSE) coordinates, the y-axis is the one that is usually more aligned with the central axis of such structures.

For this model, the following hypotheses are considered:

- ◇ The radial component inside the cylinder is zero[1]: $B^r = 0$.
- ◇ Axial invariance within the FR for any physical property ($\partial_y = 0$).
- ◇ The cross section of the structure is circular, with constant radius R.
- ◇ The current density has a zero radial component $j^r = 0$, so that $\mathbf{j} = (0, j_\varphi, j_y)$.
- ◇ The free-force condition is not imposed.

The difference between Hidalgo's case and Teresa's lies in the fact that Hidalgo considered both components of the current density field j_φ and j_y to be constant, whereas Nieves considers both components variable, expressible as a series of polynomials in r. For this case, the components of the current density and the magnetic field can be expressed as shown below:

Flux and Field Equations for the CC Model

$$
\begin{array}{lll}
j_r = 0 & j_y(r) = \displaystyle\sum_{m=0}^{M} \beta_m \, r^m & j_\varphi(r) = -\displaystyle\sum_{n=1}^{N} \alpha_n \, r^n \\
B^r = 0 & B^y(r) = B_0^y \; - \; \mu_0 \displaystyle\sum_{n=1}^{N} \frac{\alpha_n}{n+1} \, r^{n+1} & B^\varphi(r) = -\,\mu_0 \displaystyle\sum_{m=0}^{M} \frac{\beta_m}{m+2} \, r^{m+1}
\end{array}
\tag{2.1}
$$

[1] In Chapter 3, this assumption is justified in more detail.

2.2.1 Reconstruction Process

The reconstruction methodology used for this model starts from a simplified form for the magnetic and current fields:

Magnetic Field for the Reconstruction Process of the CC Model

$$B^r = 0, \qquad B^y = \frac{\mu_0\,\alpha}{2}\left(\tau R^2 - r_{\text{sat}}^2\right) \qquad B^\varphi = -\frac{\mu_0\, j_y\, r_{\text{sat}}}{2} \tag{2.2}$$

Here, a new parameter has been introduced: τ, which is a dimensionless parameter introduced by Nieves–Chinchilla that regulates the distance between the axial field at the center of the cylinder ($r = 0$) and that at the boundary ($r = R$). This parameter refers to the magnetic field coefficients for each power of r, and can be defined as:

$$\tau_n = \frac{B_y^0\,(n+1)}{\mu_0\,\alpha_n\,R^{n+1}} \tag{2.3}$$

where n is the corresponding order of the j^φ polynomial. For his reconstruction model, j^φ was assumed to grow linearly with r, so we have $n = 1$.

The two angles are defined to describe the position of the cylinder with respect to the ecliptic plane. On one hand, θ represents the angle that the cylinder axis forms with the XY plane (i.e., the ecliptic plane itself), and the angle ϕ represents the angle that that axis forms with the YZ plane.

With this, two rotations are initially applied to locate the coordinate system in the local Cartesian system of the cylinder. The equivalence is as follows:

$$B_x^{\text{GSE}} = B_x^{\text{local}}\cos\phi - B_y^{\text{local}}\sin\phi\cos\theta + B_z^{\text{local}}\sin\phi\sin\theta, \tag{2.4}$$

$$B_y^{\text{GSE}} = B_x^{\text{local}}\sin\phi + B_y^{\text{local}}\cos\phi\cos\theta - B_z^{\text{local}}\cos\phi\sin\theta, \tag{2.5}$$

$$B_z^{\text{GSE}} = B_y^{\text{local}}\sin\theta + B_z^{\text{local}}\cos\theta, \tag{2.6}$$

A possible illustration to view these two coordinate systems is the following:

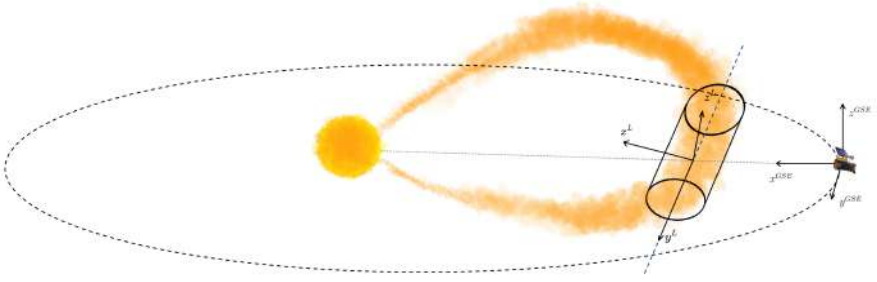

Figure 2.2: GSE and Local Cartesian Coordinate Systems.

Once here, these components are converted to the cylindrical system. In this case, the reference system is orthonormal, so this change can be made very directly, without needing to use the metric as is done later in other geometries. The equivalence between both systems is as follows:

$$B_x^{\text{local}} = B_r \cos\varphi_{\text{sat}} - B_\varphi \sin\varphi_{\text{sat}}, \tag{2.7}$$

$$B_y^{\text{local}} = B_y, \tag{2.8}$$

$$B_z^{\text{local}} = B_r \sin\varphi_{\text{sat}} + B_\varphi \cos\varphi_{\text{sat}}, \tag{2.9}$$

Finally, once located in this reference system, the satellite trajectory is parameterized using its position in Cartesian coordinates and converting it to cylindrical coordinates:

$$r_{\text{sat}} = \sqrt{x_{\text{sat}}^2 + z_{\text{sat}}^2} \qquad \sin\varphi_{\text{sat}} = \frac{z_{\text{sat}}}{r_{\text{sat}}} \tag{2.10}$$

Where x_{sat} and z_{sat} correspond to the local Cartesian coordinates through which the satellite passes:

$$x_{\text{sat}} = \left(v_{\text{sw}}\, t - x_0\right)\cos\varphi \qquad z_{\text{sat}} = \sin\varphi\, \sin\theta \left(v_{\text{sw}}\, t - x_0\right) \; - \; Z_0 \cos\theta. \tag{2.11}$$

Once the trajectory parameterization is obtained, the model can be fitted to the experimental data to see which shape is most likely to capture the FR.

2.2.2 Limitations of the Reconstruction Methodology

The article itself acknowledges that the reconstruction methodology used has several limitations. In the fitting model, it comments: *"Sometimes manual adjustments are needed to help the routine to converge to the best solution"*, which is caused by the fact that the solution algorithm used tries to minimize the squared error obtained by solving for all fit parameters simultaneously, comparing it with the in-situ values. However, the solution obtained with that algorithm need not be the system's optimal one. In general, one finds a solution that minimizes the error locally, but there is no way to verify that this solution is the absolute one.

On the other hand, beyond this, this reconstruction model does not take into account that when crossing the cylinder, if it is not oriented perpendicular to the x^{GSE} axis, the spacecraft will perceive an elliptical cross section instead of a circular one, and this will alter the parameterization of the components. To account for this, a correction factor should be applied: to adapt the horizontal distances, they should be divided by $\cos\phi$. On the other hand, to adapt the vertical distances, lengths should be divided by $\cos\theta$. The Annex C shows how this correction should be carried out.

2.3 Elliptical Cylindrical (EC) Model

The next evolutionary step of the previous model was a generalization of the flux rope cross section. Now, instead of being simply circular, it was allowed to take on an elliptical shape. The main consequence of this change is that the basis used is no longer orthogonal, and the necessary corrections must be applied to adapt the variables to this metric. This development is presented in more detail in the next chapter.

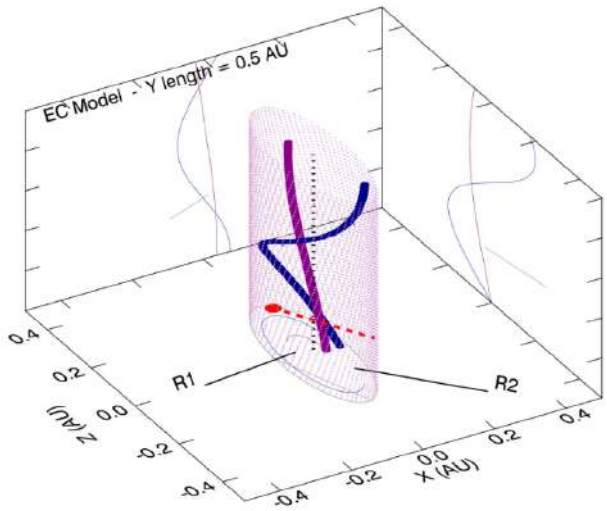

Figure 2.3: Elliptical Cylindrical Model of the Flux Rope – Teresa Nieves

This change is highly significant when fitting the results. Now, if the spacecraft crossed the flux rope, it no longer necessarily observed a symmetric magnitude of the magnetic field; the path could also be inclined. Visually, this can be seen in Figure 2.4, which compares the behavior of a fit performed with the circular model versus the elliptical model.

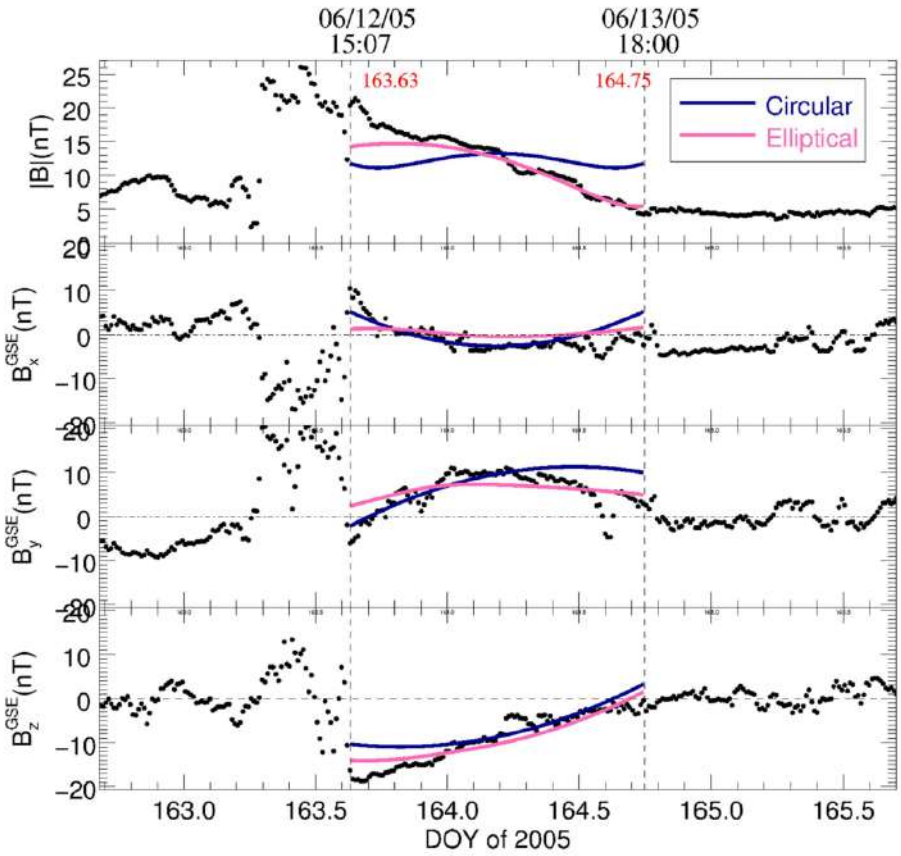

Figure 2.4: Comparison of fitting results using the CC and EC models [19].

2.3.1 Resulting Form of the Magnetic Field

For this model, the final analytic forms of both the magnetic field and the current density are summarized in Box 2.3.1.

Field and Current–Density Components for the EC Model

$$B^r = 0, \qquad B^y = \mu_0\,\delta \sum_{n=1}^{\infty} \frac{\alpha_n}{n+1}\left(\tau\, R^{n+1} - r^{n+1}\right), \qquad B^\varphi = -\,\mu_0\, h\,\delta \sum_{m=0}^{\infty} \beta_m \frac{r^{m+1}}{\delta^2 + m + 1},$$

$$j^r = 0, \qquad j^y = h^2 \sum_{m=0}^{\infty} \beta_m \frac{\chi + m}{\delta^2 + m + 1}\, r^m, \qquad j^\varphi = -\,h \sum_{n=1}^{\infty} \alpha_n\, r^n$$

Where δ is the ellipse distortion factor, α_n and β_m are the respective coefficients for each term of the polynomial series in B^y and B^φ (and hence in j^y, j^φ), τ is the same dimensionless parameter as shown in the previous model. μ_0 is the magnetic permeability of free space, and h is the metric scale–factor in the elliptical–cylindrical basis. Finally, χ is an auxiliary parameter arising in the current–density expressions, defined as follows:

$$h = \left(\delta^2 \sin^2\varphi + \cos^2\varphi\right)^{1/2}, \quad \chi = \frac{\delta^2 + 1}{h^2}$$

These are the generals expressions defined for this model. However, they will then be simplified in the reconstruction routine in order to reduce the number of free parameters.

2.3.2 Reconstruction Process

The simplified formulas used for the reconstruction process are the following:

Magnetic Field for the Reconstruction Process of the EC Model

$$B^r = 0, \qquad B^y = \delta B_1^0 \left[\tau - \bar{r}^2\right], \qquad B^\varphi = -\frac{2\,\delta\,h}{(\delta^2+1)}\,\frac{B_1^0}{C_{10}}\,\bar{r} \tag{2.12}$$

where $\bar{r} = r/R$ and B_1^0 is the axial magnetic field at the center of the flux rope with $m = 0$ and $n = 1$. Finally, C_{10} is the ratio of coefficients α_1 to β_0, multiplied by R:

$$C_{10} = \frac{\alpha_1}{\beta_0}\,R.$$

As in the circular-cylindrical case, one can see that these field forms represent a considerable simplification compared to the original theoretical expression. Essentially, the B^y component becomes a second-order polynomial without a first-order r term, while the B^φ component reduces to a coefficient multiplied by the radial variable r. By regrouping constants, it can be rewritten as:

$$B^y = A + B\,r^2, \qquad B^\varphi = C\,r \tag{2.13}$$

Where we define:

$$A = B_0^y = \delta\,B_1^0\,\tau, \qquad B = -\frac{\delta\,B_1^0}{R^2}, \qquad C = -\frac{2\,\delta\,h}{(\delta^2+1)}\,\frac{B_1^0}{C_{10}\,R}. \tag{2.14}$$

The combination of these parameters creates confusion which may lead to misleading results. The following chapter will demonstrate the complete derivation of physical validity constraints for our model. The derivation will extend integer polynomial orders to general orders and investigate exponential functional forms as potential model expressions.

The present work will employ this geometry but the model together with experimental fitting procedure will undergo complete reformulation. The following section presents additional models with advanced geometries but we will demonstrate that increased complexity does not necessarily result in better performance.

2.4 Distorted Toroidal Model

The second model presented by Nieves-Chinchilla in 2023 [21] brought two major modifications to the model. On the one hand, now the central axis of the flux rope now follows a torus shape with major radius ρ instead of being straight.

Additionally, now the cross-sectional area, despite also remaining constant, can be defined through any function $F(\varphi)$.

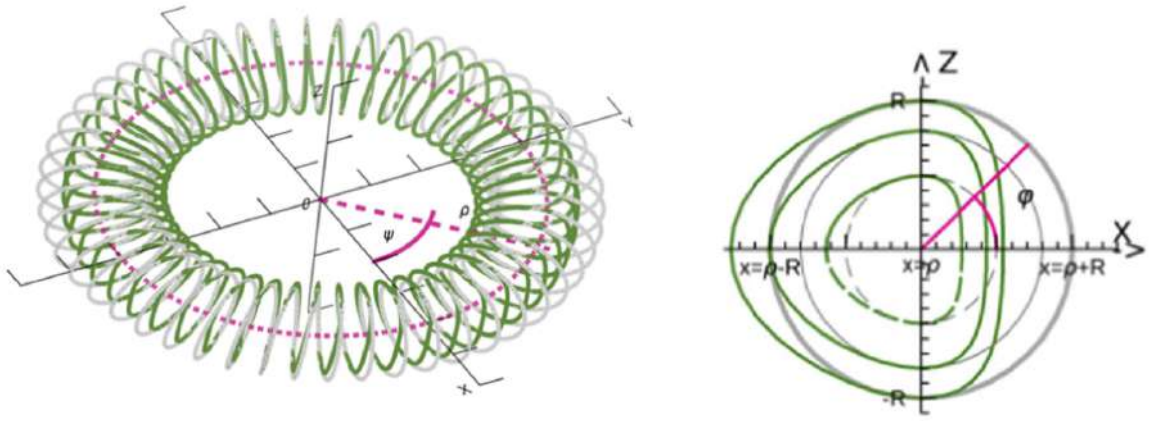

(a) Toroidal model **(b)** Cross section of the torus

Figure 2.5: Toroidal model and its cross section.

To implement these modifications, one must re-derive the metric components and adapt them to this geometry. Nevertheless, the final forms of the magnetic field remain essentially the same as in the previous models:

Magnetic Field for the Reconstruction Process of the Toroidal Model

$$B^y(r,\varphi) = B_1\left[\tau - \bar{r}^2\right], \qquad B^\varphi(r,\varphi) = -\frac{h}{h_y\,\bar{g}}\,\frac{B_1}{C_{10}}\,\bar{r} \tag{2.15}$$

Here, the parameters h, h_y, and $\bar{g}$ are derived from the chosen metric and may depend on both geometric parameters and the coordinates (r, φ).

This model can be extremely useful for defining more general behaviors of flux ropes associated with CMEs. Clearly, real in-situ cross sections are unlikely to be as perfectly circular or elliptical. While this approach has promising potential and its geometry is not overly complex, it has yet to be applied to actual spacecraft observations. To date, it has only been studied theoretically to predict the magnetic field signature a spacecraft would record when traversing the structure transversely, assuming no rotation in space. It would certainly be an interesting project to pursue in the future.

2.5 Tapered Torus Model

Finally, we arrive at the most geometry-free model to date. The aim of the author, Andreas Weiss in 2024 [30], was to define the entire CME structure from its roots at the Sun to the points where it is detected.

The main motivation was to avoid the magnetic field singularity that occurs if the ends terminate at a point. Until very recently, this was considered the best remedy for that issue. However, recent studies Teresa Nieves and Jesús Navas have shown that, for helicity to exist in such structures, one must impose an exponential decay of the axial component of the magnetic field along the CME's legs. Doing so allows closed-boundary geometries to exist and makes the internal magnetic field physically realizable.

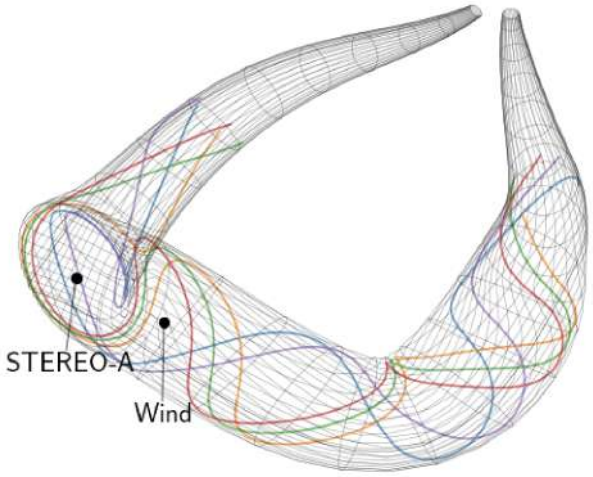

Figure 2.6: Tapered Torus Model of the Flux Rope – Andreas Weiss

The ultimate goal of this method was to provide as generic a geometry as possible, with distortion both in its cross section and along its internal axis, thereby explaining a wider variety of internal phenomena resulting from the compression or expansion of that geometry.

The components of the internal magnetic field still depended purely on the radial distance, and angular dependencies appeared only through the geometric deformation.

On paper, this methodology was very promising, but its implementation presented a significant practical drawback. The fitting routine, as with the models in Sections 2.2 and 2.3, used a global solver that included all geometric and physical parameters simultaneously. If we have 20 parameters with complex interdependencies, the final solution space will contain many combinations that locally minimize the error relative to the experimental data, but almost certainly none of these will be the true global minimum.

If this was already difficult to achieve in simpler models (sometimes requiring manual tweaks to force a solution) for this system the method becomes practically impossible. Indeed, to reach a solution within a few days, one can use only about 10 experimental points [29], thereby ne-

glecting the valuable information contained in the thousands of other accessible measurements.

As mentioned earlier, a possible workaround would be to iterate over the initial values for each parameter across its full domain. However, if we assume 20 parameters and want to perform just 4 iterations for each, this would require solving the entire system $4^{20} \sim 10^{12}$ times. Assuming optimistically that a single iteration takes 1 second, this method would take approximately 31.7 years to complete!

3 . Generalization of the EC Model

In the previous chapter, we saw that, over time, great emphasis has been placed on the variation of flux-rope geometry, but far less attention has been paid to whether the magnetic field inside them is as general as it could be.

The differential equations that govern magnetohydrodynamics can account for many physical phenomena, but it is only when specific boundary conditions are imposed that they describe a particular physical situation. In the case of cylindrical–elliptical flux ropes, a polynomial model for the magnetic-field components has been proposed until now. In this study, however, we will develop not only why that choice may or may not be valid, but also which alternative functions (and for what reasons) could be used to continue describing the magnetic field in the desired geometry.

3.1 Elliptical-Cilyndrical coordinate system

The structure of the Flux Rope consists of a cylinder with an elliptical cross-section, where we can define the coordinates as:

$$\begin{cases} x = a\, r\, \cos\varphi \\ y = y \\ z = \delta\, a\, r\, \sin\varphi \end{cases} \tag{3.1}$$

Here, a corresponds to the major semi-axis of the ellipse, r is the normalized radial coordinate, constrained to $r \in (0, 1)$, φ is the azimuthal angle, and δ is the distortion parameter of the ellipse ($\delta = b/a$, where b is the minor semi-axis).

This is a non-orthogonal basis, which requires special attention to the basis vectors to ensure that properties are preserved under coordinate transformations. In differential geometry, vectors and tensors can be represented in their covariant or contravariant forms. Covariant components transform in the same direction as their differentials (dx^i), making them suitable for defining the basis vectors. In contrast, contravariant components transform inversely to these coordinates. This compensates for the distortion that might arise from the covariant

components, ensuring that the result matches physical reality.

The vectors forming this non-orthogonal basis can be obtained by taking the partial derivatives of the Cartesian components with respect to the new coordinates:

$$\varepsilon_i = \frac{\partial \mathbf{r}}{\partial q^i} \tag{3.2}$$

where ε_i is the covariant basis vector, q^i is the contravariant coordinate (r, y, φ), and $\mathbf{r}$ represents the Cartesian coordinates (x, y, z). Thus, the following vectors are obtained for this basis:

$$\begin{cases} \varepsilon_r = a\,(\cos\varphi,\ 0,\ \delta\,\sin\varphi) \\ \varepsilon_y = (0,\ 1,\ 0) \\ \varepsilon_\varphi = a\,r\,(-\sin\varphi,\ 0,\ \delta\,\cos\varphi) \end{cases} \tag{3.3}$$

In a generic coordinate system, a metric tensor can be defined, which will act to account for possible stretching or twisting of coordinates. This is represented as a matrix whose components are the dot products of the basis vectors. We will use this object to ensure consistency in the transformation of properties within our non-orthogonal system. It is defined as follows:

$$g = \begin{pmatrix} g_{rr} & g_{ry} & g_{r\varphi} \\ g_{yr} & g_{yy} & g_{y\varphi} \\ g_{\varphi r} & g_{\varphi y} & g_{\varphi\varphi} \end{pmatrix} = \begin{pmatrix} \varepsilon_r \cdot \varepsilon_r & \varepsilon_r \cdot \varepsilon_y & \varepsilon_r \cdot \varepsilon_\varphi \\ \varepsilon_y \cdot \varepsilon_r & \varepsilon_y \cdot \varepsilon_y & \varepsilon_y \cdot \varepsilon_\varphi \\ \varepsilon_\varphi \cdot \varepsilon_r & \varepsilon_\varphi \cdot \varepsilon_y & \varepsilon_\varphi \cdot \varepsilon_\varphi \end{pmatrix}$$

For our case, the non-zero components of the metric tensor g_{ij} are:

$$g_{rr} = a^2(\cos^2\varphi + \delta^2 \sin^2\varphi)$$

$$g_{yy} = 1$$

$$g_{\varphi\varphi} = a^2 r^2(\sin^2\varphi + \delta^2 \cos^2\varphi)$$

$$g_{r\varphi} = g_{\varphi r} = a^2 r \sin\varphi\cos\varphi(\delta^2 - 1)$$

Thus, we obtain:

$$g = \begin{pmatrix} g_{rr} & 0 & g_{r\varphi} \\ 0 & g_{yy} & 0 \\ g_{\varphi r} & 0 & g_{\varphi\varphi} \end{pmatrix} = \begin{pmatrix} a^2(\cos^2\varphi + \delta^2\sin^2\varphi) & 0 & a^2 r\sin\varphi\cos\varphi(\delta^2-1) \\ 0 & 1 & 0 \\ a^2 r\sin\varphi\cos\varphi(\delta^2-1) & 0 & a^2 r^2(\sin^2\varphi + \delta^2\cos^2\varphi) \end{pmatrix}$$

For this metric, the magnitude of the magnetic field is given by the following form:

$$|\mathbf{B}| = \sqrt{g_{rr}(B^r)^2 + g_{yy}(B^y)^2 + g_{\varphi\varphi}(B^\varphi)^2 + 2g_{r\varphi}B^r B^\varphi} \tag{3.4}$$

Finally, for operations such as the curl in this space, it will also be necessary to know the determinant of this tensor and its squared root, which has been derived in Appendix B. It takes the following form:

$$\det(g) = a^4\, r^2\, \delta^2 \quad \longrightarrow \quad \sqrt{\det(g)} = a^2\, r\, \delta \tag{3.5}$$

With this, we now have the foundations on which to develop our model. However, we will see below that we cannot arbitrarily use just any model to define the magnetic field inside the flux rope. In order for such a structure to exist, the conditions outlined in the following sections must be met.

3.2 Magnetic Field Requirements

For the model to be valid, it must satisfy specific conditions governing both the magnetic field configuration and the associated current density field.

To ensure the magnetic field is physically realizable within the specified geometry, the primary condition is that its divergence must be zero, as mandated by Gauss's law for magnetic fields:

$$\nabla \cdot \mathbf{B} = \partial_r(rB^r) + \partial_\varphi(rB^\varphi) + \partial_y(rB^y) = 0 \tag{3.6}$$

We assume, consistent with prior models, that no physical properties vary along the axial direction of the flux rope (i.e., $\partial_y = 0$). Additionally, each magnetic field component is expressed as a product of separable functions of the radial coordinate r and azimuthal angle φ. Generally, we write:

$$\begin{cases} B^r(r,\varphi) = f_1(r)g_1(\varphi) + K_1 \\ B^y(r,\varphi) = f_2(r)g_2(\varphi) + K_2 \\ B^\varphi(r,\varphi) = f_3(r)g_3(\varphi) + K_3 \end{cases} \tag{3.7}$$

However, apart from satisfying the divergence-free condition, the magnetic field must also exhibit continuity with the external region outside the flux rope's volume to ensure physical consistency.

3.2.1 Compliance with Gauss's Law for Magnetism

Applying the functions in 3.7 to condition 3.6 yields the following partial-differential equation:

$$g_1(\varphi)\,\partial_r\big(r f_1(r)\big) \;+\; r f_3(r)\,\partial_\varphi\big(g_3(\varphi)\big) \;=\; 0 \tag{3.8}$$

This can also be written as

$$g_1(\varphi)\,\big[f_1(r) + r f_1'(r)\big] \;+\; r f_3(r)\,g_3'(\varphi) \;=\; 0.$$

Rearranging and separating variables, we obtain

$$\frac{f_1(r) + r f_1'(r)}{r f_3(r)} \;=\; -\frac{g_3'(\varphi)}{g_1(\varphi)} \;=\; k,$$

which leads to two separate ODEs, one for each variable:

- ◇ For φ: $g_3'(\varphi) = -k\,g_1(\varphi)$

$$g_3(\varphi) = C_1 \;-\; k\int g_1(\varphi)\,d\varphi \tag{3.9}$$

- ◇ For r: $f_1(r) + r f_1'(r) = k\,r\,f_3(r)$

$$f_1(r) = \frac{k}{r}\int r f_3(r)\,dr \;+\; \frac{C_2}{r} \tag{3.10}$$

Thus we arrive at the following expressions for the magnetic-field components:

$$\begin{cases} B^r(r,\varphi) &= \left[\dfrac{k}{r}\int r f_3(r)\,dr + \dfrac{C_2}{r}\right] g_1(\varphi) \;+\; K_1, \\ B^y(r,\varphi) &= f_2(r)\,g_2(\varphi) \;+\; K_2, \\ B^\varphi(r,\varphi) &= f_3(r)\,\left[C_1 - k\int g_1(\varphi)\,d\varphi\right] \;+\; K_3. \end{cases}$$

3.2.2 Continuity at the Boundary of the Flux Rope

The field must meet two essential requirements to be valid. The field must be continuous at the boundary of the flux rope with the exterior. The previous models will be used to determine that the flux rope is isolated and the external magnetic field is zero. The boundary does not have any field lines crossing it because the axial and azimuthal components are always tangential to it. The magnetic field component that needs to be considered is the radial component of the magnetic field, B^r. The condition to be satisfied is:

$$B^r(R,\varphi) = 0 = \left[\frac{k}{R}\int_0^R r\, f_3(r)\, dr + \frac{C_2}{R}\right] g_1(\varphi) + K_1 \tag{3.11}$$

We observe that this expression can be seen as a constant multiplied by $g_1(\varphi)$ plus an independent term.

Since the term multiplying $g_1(\varphi)$ is nonzero, the only solution is for both $g_1(\varphi)$ and K_1 to be identically zero. This implies that the poloidal component now takes the form:

$$B^\varphi(r,\varphi) = f_3(r)\, C_1 + K_3 \;\equiv\; f_3(r) \tag{3.12}$$

where, for simplicity, we have absorbed the constants C_1 and K_3 into the function $f_3(r)$.

This leaves us with the following form for the magnetic-field components:

Magnetic Field Components After Applying Physical Constraints

$$\begin{cases} B^r = 0 \\ B^y(r,\varphi) = f_2(r)\, g_2(\varphi) + K_2 \\ B^\varphi(r) = f_3(r) \end{cases} \tag{3.13}$$

However, we will see below that these functions also impose additional constraints.

3.3 Requirements for the Current Density Field

For the case of the current density vector $\mathbf{j}$ within the flux rope, it must be ensured that no singularities or discontinuities arise. This requires that all components be smooth throughout the volume and that the limits exist as $r \to 0$.

3.3.1 Derivation of the Current Density Formulas

The current density components are obtained via the generalized Ampère's law in the elliptical-cylindrical metric:

$$\nabla \times \mathbf{B} = \frac{\varepsilon^{ijk}}{\sqrt{\det(g)}}\, \partial_j\big(g_{kl} B^l\big) = \mu_0\, \mathbf{j}, \tag{3.14}$$

where ε^{ijk} is the Levi-Civita tensor in the coordinate basis $\{i,j,k\} = \{r, y, \varphi\}$, g_{kl} is the metric tensor, and $\sqrt{|g|} = a^2 r\delta$ is the square root of its determinant (see Appendix B). Here, $g_{kl}B^l$ denotes the covariant components of the magnetic field (recalling the conversion: $B_i = g_{il}B^l$).

Thus,

$$B_i = g_{il}B^l = g_{ir}B^r + g_{iy}B^y + g_{i\varphi}B^\varphi. \tag{3.15}$$

The Levi-Civita tensor is an antisymmetric tensor used to express cross products and curls in tensor notation. In three dimensions, $\varepsilon^{ijk} = +1$ for even permutations of $(1, 2, 3)$, -1 for odd permutations, and zero if any indices are equal. For our coordinate ordering (r, y, φ), we have $\varepsilon^{ry\varphi} = +1$ (and for its even permutations) and -1 for the odd permutations.

Derivation of each component

By applying the above, we can calculate each component of the curl:

- ◇ **Component j^r:** For $i = r$, the non-zero ε^{rjk} terms are $\varepsilon^{ry\varphi} = +1$, $\varepsilon^{r\varphi y} = -1$. Thus:

$$(\nabla \times \mathbf{B})^r = \frac{1}{\sqrt{\det(g)}} \left[\varepsilon^{ry\varphi}\partial_y(g_{\varphi l}B^l) + \varepsilon^{r\varphi y}\partial_\varphi(g_{yl}B^l)\right] \tag{3.16}$$

Since there is no axial variation, $\partial_y = 0$, the first term vanishes. Also, for this case the covariant component reduces to: $g_{yl}B^l = g_{yy}B^y = B^y$. Therefore, the equation reduces to:

$$j^r = \frac{1}{\mu_0 a^2 \delta r}(-\partial_\varphi B^y). \tag{3.17}$$

- ◇ **Component j^y:** Following a reasoning similar to the previous case, we now set $i = y$, and the non-zero Levi-Civita symbols are $\varepsilon^{y\varphi r} = +1$, $\varepsilon^{yr\varphi} = -1$:

$$(\nabla \times \mathbf{B})^y = \frac{1}{\sqrt{\det(g)}} \left[+\,\partial_\varphi\big(g_{rl}B^l\big) \;-\; \partial_r\big(g_{\varphi l}B^l\big)\right]. \tag{3.18}$$

Where the covariant components are:

$$g_{rl}B^l = g_{rr}\cancelto{0}{B^r} + g_{r\varphi}B^\varphi \tag{3.19}$$

$$g_{\varphi l}B^l = g_{\varphi r}\cancelto{0}{B^r} + g_{\varphi\varphi}B^\varphi \tag{3.20}$$

Thus:

$$(\nabla \times \mathbf{B})^y = \frac{1}{\sqrt{\det(g)}} \left[\partial_\varphi(g_{r\varphi}B^\varphi) - \partial_r(g_{\varphi\varphi}B^\varphi)\right]. \tag{3.21}$$

So:

$$j^y = \frac{1}{\mu_0 a^2 \delta r} \left[\partial_\varphi (g_{r\varphi} B^\varphi) - \partial_r (g_{\varphi\varphi} B^\varphi)\right]. \tag{3.22}$$

◇ **Component j^φ:** Finally, for $i = \varphi$, the non-zero terms are $\varepsilon^{\varphi r y} = +1$, $\varepsilon^{\varphi y r} = -1$:

$$(\nabla \times \mathbf{B})^\varphi = \frac{1}{\sqrt{\det(g)}} \left[+\partial_r (g_{yl} B^l) - \partial_y (g_{rl} B^l)\right] \tag{3.23}$$

Since $\partial_y = 0$, the second term vanishes. And since for the first term we have: $g_{yl} B^l = g_{yy} B^y = B^y$, we obtain:

$$(\nabla \times \mathbf{B})^\varphi = \frac{1}{\sqrt{\det(g)}} \partial_r B^y. \tag{3.24}$$

Therefore:

$$j^\varphi = \frac{1}{\mu_0 a^2 \delta r} \partial_r B^y. \tag{3.25}$$

Combining these, the current density components are:

$$j^r = \frac{1}{a^2 \delta r \mu_0} (-\partial_\varphi B^y) \tag{3.26}$$

$$j^y = \frac{1}{a^2 \delta r \mu_0} \left[\partial_\varphi (g_{r\varphi} B^\varphi) - \partial_r (g_{\varphi\varphi} B^\varphi)\right] \tag{3.27}$$

$$j^\varphi = \frac{1}{a^2 \delta r \mu_0} \partial_r B^y \tag{3.28}$$

Substituting now the forms of the magnetic field found above and arranging a little, we are left with the following expressions:

Current Density General Expressions for the EC Model

$$j^r(r,\varphi) = \frac{-f_2(r)\, g_2'(\varphi)}{a^2\, \delta\, r\, \mu_0}$$

$$j^y(r,\varphi) = \frac{1}{\delta\, \mu_0} \Big[f_3(r)\, (\delta^2 - 1)\, (2\cos^2\varphi - 1) - (\sin^2\varphi + \delta^2 \cos^2\varphi)\, (2 f_3(r) + r\, f_3'(r)) \Big]$$

$$j^\varphi(r,\varphi) = \frac{f_2'(r)\, g_2(\varphi)}{a^2\, \delta\, r\, \mu_0}$$

3.3.2 Requirements to Ensure Physical Validity

To ensure the current density field is physically valid, its components must have a finite limit throughout the domain, particularly at the center ($r = 0$), where singularities could arise. For this limit to exist, considering that trigonometric functions are not constant, each component must satisfy:

$$\lim_{r\to 0} j^i(r,\varphi) = 0, \quad i = r, y, \varphi \tag{3.29}$$

For this to happen, all trigonometric functions must be multiplied by a radial function that vanishes as $r \to 0^+$. Thus, we derive the necessary conditions for this to occur:

Existence of the Limit for j^r:

$$j^r(r,\varphi) = \frac{-f_2(r)\cdot g_2'(\varphi)}{a^2\delta r\mu_0}$$

For the limit to be zero, $\frac{f_2(r)}{r} \to 0$. We can distinguish two possible types of solutions:

- ◇ **Polynomial Form**: If $f_2(r) \propto r^{n_2}$, then $\frac{f_2(r)}{r} \propto r^{n_2-1}$, requiring $n_2 - 1 > 0 \implies n_2 > 1$. Thus, the minimum polynomial order of $f_2(r)$ must be strictly greater than 1.
- ◇ **Exponential Form**: If $f_2(r) \propto e^{-1/r^\alpha}$, $\alpha > 0$, then as $r \to 0^+$, $e^{-1/r^\alpha} \to 0$, and:

$$\frac{f_2(r)}{r} \propto \frac{e^{-1/r^\alpha}}{r} \to 0$$

  since the exponential decay dominates.

Thus, $f_2(r)$ must satisfy $f_2(r) \propto r^{n_2}$, $n_2 > 1$, or $f_2(r) \propto e^{-1/r^\alpha}$, $\alpha > 0$.

Existence of the Limit for j^y:

The axial component is:

$$j^y(r,\varphi) = \frac{1}{\delta\mu_0}\left[f_3(r)(\delta^2-1)(2\cos^2\varphi - 1) - (\sin^2\varphi + \delta^2\cos^2\varphi)(2f_3(r) + rf_3'(r))\right]$$

As there is no r term dividing in the denominator, the condition will be that the terms $f_3(r)$ and $rf_3'(r)$ must vanish as $r \to 0$.

- ◇ **Polynomial Form**: If $f_3(r) \propto r^{n_3}$, then:

$$f_3(r) \propto r^{n_3}, \quad rf_3'(r) \propto r^{n_3}$$

And it is easy to see how the necessary condition will be $n_3 > 0$.

◇ **Exponential Form**: If $f_3(r) \propto e^{-1/r^\alpha}$, then:

$$r f_3'(r) \propto e^{-1/r^\alpha} \cdot \frac{\alpha}{r^{\alpha+1}}$$

And we observe that:

$$\lim_{r \to 0^+} r f_3'(r) \to 0 \tag{3.30}$$

For $\alpha > 0$, this always holds, since the exponential decays faster than the polynomial function.

Thus, $f_3(r) \propto r^{n_3}$, $n_3 > 0$, or $f_3(r) \propto e^{-1/r^\alpha}$, $\alpha > 0$, ensures $j^y \to 0$ for $r \to 0$.

Existence of the Limit for j^φ:

The azimuthal component is:

$$j^\varphi(r, \varphi) = \frac{f_2'(r) \cdot g_2(\varphi)}{a^2 \delta r \mu_0}$$

For the limit to be zero, it must hold that $\frac{f_2'(r)}{r} \to 0$ for $r \to 0$. We also study the polynomial and exponential possibilities:

◇ **Polynomial Form**: If $f_2(r) \propto r^{n_2}$, then:

$$f_2'(r) \propto n_2 r^{n_2 - 1}, \quad \frac{f_2'(r)}{r} \propto r^{n_2 - 2}$$

For $\frac{f_2'(r)}{r} \to 0$, we need $n_2 - 2 > 0 \implies n_2 > 2$. Thus, the minimum order of $f_2(r)$ is strictly greater than 2.

◇ **Exponential Form**: If $f_2(r) \propto e^{-1/r^\alpha}$:

$$f_2'(r) = e^{-1/r^\alpha} \cdot \frac{\alpha}{r^{\alpha+1}} \quad \Rightarrow \quad \frac{f_2'(r)}{r} = \frac{\alpha}{r^{\alpha+2}} e^{-1/r^\alpha}$$

$$\lim_{r \to 0^+} \frac{\alpha}{r^{\alpha+2}} e^{-1/r^\alpha} \to 0$$

Again, the limit is zero, as the exponential decay dominates.

Since $n_2 > 2$ for j^φ is more restrictive than $n_2 > 1$ for j^r, we adopt $n_2 > 2$.

3.3.3 Summary of the Constraints

Finally, the constraints on the radial functions that ensure the fields are physically valid are:

- $f_2(r) \propto r^{n_2}$, $n_2 > 2$, or $f_2(r) \propto e^{-1/r^\alpha}$, $\alpha > 0$.
- $f_3(r) \propto r^{n_3}$, $n_3 > 0$, or $f_3(r) \propto e^{-1/r^\alpha}$, $\alpha > 0$.

For integer polynomial orders, the minimums are $f_2(r) \propto r^3$ and $f_3(r) \propto r^1$, ensuring all current density components are singularity-free at $r = 0$.

Function	Polynomial Form	Exponential Form
$f_2(r)$	r^{n_2}, $n_2 > 2$	e^{-1/r^α}, $\alpha > 0$
$f_3(r)$	r^{n_3}, $n_3 > 0$	e^{-1/r^α}, $\alpha > 0$

Table 3.1: Constraints on radial functions for singularity-free current density.

3.4 Solutions with Only Radial Dependency

We can also study the requirements if we consider only radial dependency for each component of the magnetic field. This is relevant because, until now, only this dependency has been considered, and it can help us compare the models.

Following a reasoning similar to the previous one, we see that the fields would now take the following form:

$$\begin{cases} B^r(r) = f_1(r) \\ B^y(r) = f_2(r) \\ B^\varphi(r) = f_3(r) \end{cases} \tag{3.31}$$

The equation 3.6 directly implies that B^r can either be zero always or proportional to $1/r$. The latter case would imply a singularity at the origin, so we discard it as it lacks physical meaning. Thus, we have $B^r = 0$ always, as in the previous case.

On the other hand, if we now apply equation 3.14, we see that the formulas for the current density components simplify:

$$j^r = 0 \tag{3.32}$$

$$j^y = \frac{1}{a^2 \delta r \mu_0} \left[-\partial_r (g_{\varphi\varphi} B^\varphi) \right] \tag{3.33}$$

$$j^\varphi = \frac{1}{a^2 \delta r \mu_0} \left(\partial_r B^y \right) \tag{3.34}$$

This can be expanded to obtain the following:

$$j^r = 0 \tag{3.35}$$

$$j^y = \frac{1}{\delta\mu_0}(\sin^2\varphi + \delta^2\cos^2\varphi)[2f_3(r) + rf_3'(r)] \tag{3.36}$$

$$j^\varphi = \frac{1}{a^2\delta r\mu_0}f_2'(r) \tag{3.37}$$

Now, as before, we will examine the necessary requirements for the limit of these functions to exist as $r \to 0$. For the case of $j^y(r)$, we see that it is sufficient to impose $f_3(r) \propto r^{n_3}$, with $n_3 > 0$. For the case of j^φ, we observe that the requirement is $f_2'(r) \propto r^{n_2-1}$, with $n_2 - 1 \geq 1 \implies n_2 \geq 2$, so we have $f_2(r) \propto r^{n_2} + C$, which corresponds to a minimum order of ≥ 2. It is worth noting that in this second case, $f_2(r)$ may also include a constant term, since only the derivative of this function affects singularities at the center. Alternatively, as in the previous sections, both $f_2(r)$ and $f_3(r)$ can take the exponential form e^{-1/r^α}, $\alpha > 0$, which also ensures the limits vanish as $r \to 0$.

Function	**Polynomial Form**	**Exponential Form**
$f_2(r)$	$r^{n_2} + C$, $n_2 \geq 2$	e^{-1/r^α}, $\alpha > 0$
$f_3(r)$	r^{n_3}, $n_3 > 0$	e^{-1/r^α}, $\alpha > 0$

Table 3.2: Constraints on radial functions for singularity-free current density with only radial dependency.

3.5 Possible Model Candidates

3.5.1 Generic Model: With Radial and Angular Dependency

Finally, having studied the physical background, we can establish example models that meet the imposed requirements. A basic example would be the following:

Radial-Poloidal Polynomical Model

$$\begin{cases} B^r = 0 \\ B^y(r,\varphi) = A \cdot r^3 \cdot (B + C\cos(\varphi) + D\sin(\varphi)) + E \\ B^\varphi(r) = Fr + Gr^2 + Hr^3 \end{cases} \tag{3.38}$$

As mentioned earlier, the specific constraints for the polynomial parts would allow the order to be reduced to approximately r^{2^+} for the y-component and r^{0^+} for the φ-component. Another possibility would be to treat the exponent of these functions as a parameter to be calculated, but for simplicity, this work will always consider integer exponents.

For this case, the current density components would take the following form:

$$j^r(r,\varphi) = \frac{-r^2 A(B + C\cos\varphi + D\sin\varphi)}{a^2\delta\mu_0} \tag{3.39}$$

$$\begin{aligned} j^y(r,\varphi) = \frac{1}{\delta\mu_0}\Big[&(Fr + Gr^2 + Hr^3)(\delta^2 - 1)(2\cos^2\varphi - 1) \\ &- (\sin^2\varphi + \delta^2\cos^2\varphi)(3rF + 4r^2G + 5r^3H)\Big] \end{aligned} \tag{3.40}$$

$$j^\varphi(r,\varphi) = \frac{3Ar}{a^2\delta\mu_0}(B + C\cos\varphi + D\sin\varphi) \tag{3.41}$$

An exponential form for the radial functions could also be considered:

Radial-Polodal Exponential Model

$$\begin{cases} B^r = 0 \\ B^y(r,\varphi) = A\cdot e^{-1/r^\alpha}\cdot(B + C\cos(\varphi) + D\sin(\varphi)) + E \\ B^\varphi(r) = F\cdot e^{-1/r^\beta} \end{cases} \tag{3.42}$$

For this case, the current density components are derived as follows:

$$j^r(r,\varphi) = \frac{A\cdot e^{-1/r^\alpha}\cdot(C\sin(\varphi) - D\cos(\varphi))}{a^2\delta r\mu_0} \tag{3.43}$$

$$\begin{aligned} j^y(r,\varphi) = \frac{F\cdot e^{-1/r^\beta}}{\delta\mu_0}\Big[&(\delta^2 - 1)(2\cos^2\varphi - 1) \\ &- (\sin^2\varphi + \delta^2\cos^2\varphi)\cdot\left(2 + \frac{\beta}{r^\beta}\right)\Big] \end{aligned} \tag{3.44}$$

$$j^\varphi(r,\varphi) = \frac{A\alpha\cdot e^{-1/r^\alpha}\cdot(B + C\cos(\varphi) + D\sin(\varphi))}{a^2\delta r^{\alpha+2}\mu_0} \tag{3.45}$$

These expressions satisfy the physical requirement that $\lim_{r\to 0} j^i(r,\varphi) = 0$ for $\alpha > 0$, $\beta > 0$, as the exponential terms e^{-1/r^α} and e^{-1/r^β} decay to zero as $r \to 0^+$.

3.5.2 Model with Only Radial Dependency

In this case, one possible polynomial model could take the following form:

$$\begin{cases} B^r = 0, \\ B^y(r) = C + \sum_{n=2}^{N} \alpha_n \, r^n, \\ B^\varphi(r) = \sum_{m=1}^{M} \beta_m \, r^m, \end{cases} \tag{3.46}$$

thus coinciding with the polynomial models proposed in 2.1, 2.3.1 and 2.15.

However, for this study it may be useful to employ the above model solely for comparative purposes. Accordingly, we simplify the nomenclature in our case:

Simplified Radial Model

$$\begin{cases} B^r = 0, \\ B^y(r) = A + C \, r^2, \\ B^\varphi(r) = D \, r, \end{cases} \tag{3.47}$$

In this case, the current density components take the following form:

$$j^r = 0, \tag{3.48}$$

$$j^y(r, \varphi) = -\frac{1}{\delta \, \mu_0} \left(\sin^2 \varphi + \delta^2 \cos^2 \varphi \right) 3D \, r, \tag{3.49}$$

$$j^\varphi(r) = \frac{2C}{a^2 \, \delta \, \mu_0}. \tag{3.50}$$

In X-CME, the user will be able to select which model to use for fitting the magnetic field. In the current version, the **Simplified Radial Model** (from now on, *Model 1*) and the **Radial-Poloidal Polynomical Model** (from now on, *Model 2*) have been implemented. However, the program is designed to allow a wider range of models so that they can be tested and compared against one another.

4 . Flux Rope Reconstruction Methodology

4.1 Introduction to the Reconstruction Methodology

4.1.1 Identifying the current problems

In the study of complex physical systems, it is customary to address the entire problem domain via a single, global minimization procedure. Frequently, this approach is unavoidable: the governing equations admit no closed-form solutions, and increasing model complexity forces one to treat every parameter as a free variable in a comprehensive fit.

For the models presented in Chapter 2, the solution mechanisms solve the entire system at once, attempting to determine simultaneously both the geometric parameters and the physical parameters of the magnetic field components that minimize the error against the experimental data.

What happens in these cases is that the resulting system is high-dimensional, and error-minimization algorithms cannot guarantee finding absolute extrema, but only local ones.

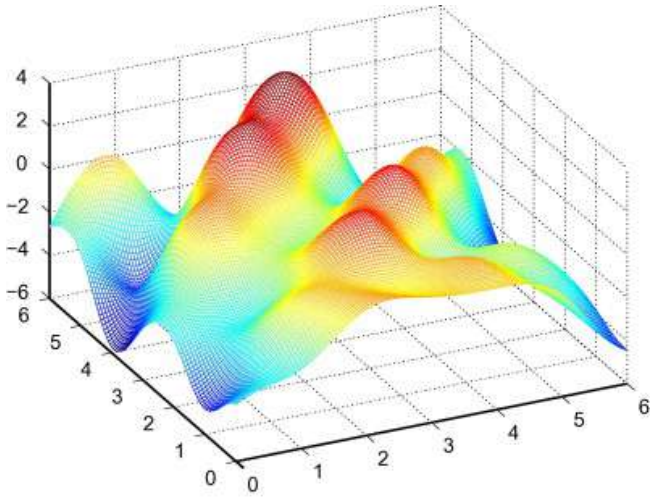

Figure 4.1: 3D surface of a multivariate function showing multiple local minima and maxima. Retrieved from [26].

It is not certain that the solution will converge for such algorithms, and if it does, it is unlikely

to reach the most optimal solution.

For this work, however, it has been observed that the geometry defined by the elliptical-cylindrical model allows us to solve the geometric system analytically, thus limiting the use of minimization algorithms to the purely in-situ fitting of each magnetic field component separately.

This chapter will detail how this problem has been addressed and will subsequently evaluate the results.

4.1.2 Methodology Overview

In the following sections of this chapter, the major blocks required to solve this problem are developed in detail. In general, one can distinguish the following processes:

1. **Data Acquisition and Processing**: Obtained from in-situ satellites and processed for use in X-CME.
2. **Parametrization of the Satellite's Trajectory inside the Flux Rope**: Determined for each combination resulting from the iterative process.
3. **Coordinate Transformation to the Flux Rope Frame**: From the spacecraft's original coordinate system to the local elliptical-cylindrical frame of the flux rope.
4. **Model Fitting to In-Situ Magnetic Field Observations**: Performed separately for each component of the magnetic field.
5. **Assessment of Fit Quality and Iterative Refinement**: Evaluated at each iteration of the process, comparing results to retain the best fit.

The iterative method restricts non-linear minimization to individual magnetic field components which produces better convergence and lower computational expenses. The final output shows both the orientation of the flux rope axis and its cross-sectional dimensions and it also reconstructs the internal field structure and current density distribution. The following sections explain each stage in detail while presenting their corresponding algorithmic code.

4.2 Data Acquisition & Processing

Currently, there are numerous active missions at various positions in the interplanetary medium that are constantly collecting data for subsequent analysis. These data are regularly uploaded to public platforms such as Helio4Cast or LASSOS, from which they can be retrieved for a wide range of studies.

Among all active missions, the X-CME code is currently set up to work with data from the

WIND, STEREO, PSP, and SOLO missions (introduced in Section 1.3). X-CME will extract the event date and then determine the satellite's or planets' locations for subsequent analysis.

4.2.1 Data Retrieval

To ensure user flexibility, X-CME provides two complementary modes for obtaining in-situ measurements:

1. **Local File Import:** Users may upload data files in `.csv`, `.txt`, or `.ascii` formats via an intuitive graphical interface.
2. **HelioSat Download:** Direct retrieval from the Helio4Cast database[1].

The HelioSat module facilitates access to in-situ measurements from a diverse fleet, including Solar Orbiter, Parker Solar Probe, BepiColombo, Wind, STEREO-A, STEREO-B, Juno, VEX, Messenger, MOESTL, MAVEN, and Ulysses. For coronal mass ejection analyses, data from Solar Orbiter, Parker Solar Probe, Wind, and STEREO-A are predominantly utilized and fully integrated within the pipeline.

It is important to note that these satellites do not always provide a continuous data record, because they experience Sun and planetary passes, as well as instrument malfunctions. This must also be taken into account by our code.

The system addresses data gaps through short-term temporal interpolation methods. The fitting procedure automatically detects long outages which results in the exclusion of affected intervals to avoid generating false results.

4.2.2 Preliminary Data Inspection

Each satellite may provide different types of data, and in different coordinate systems. In general, they will provide:

- ◇ Magnetic field intensity $||\mathbf{B}||$ and its components:
  - B_x, B_y, B_z (in the Geocentric Solar Ecliptic coordinate system (GSE)), or
  - B_r, B_t, B_n (in the Radial–Transverse–Normal (RTN) reference frame)
- ◇ Solar wind speed V_{sw}.
- ◇ Decimal day of the year ($ddoy$).
- ◇ Proton density (N_p), in [protons/cm^3].

[1] Maintained by the LASSOS research group and subject to occasional downtime; when available, it supports data requests for all missions and dates.

◇ The ratio between the plasma thermal pressure and the magnetic field pressure (plasma beta, β_p).

◇ Components and/or magnitude of the thermal speed of the particles: V_{th}.

Not all satellites offer every data type. However, those we analyze provide at least the magnetic field components, solar wind speed, and proton density, which are essential for our simulation.

Once the data file has been imported, the first output is a concise report that summarizes the event's metadata and computes key descriptive statistics of the experimental measurements.

File Details:

- **Mission:** Parker Solar Probe
- **Date:** 2022-08-18
- **Day-of-Year (ddoy):** 35.0
- **Sampling Interval:** 11m
- **Coordinate System:** RTN
- **Radial Distance (AU):** 0.5
- **Ecliptic Longitude (degrees):** 107.74

(a) Event and mission definition.

	ddoy	B	Br	Bt	Bn	Np	Vth	Vsw
count	960	960	960	960	960	638	639	638
mean	230.9993	24.7687	-10.7907	-4.1901	-2.2836	10.3669	18.459	560.983
std	0.5777	15.8449	8.0023	20.8122	15.121	15.086	10.9515	97.2666
min	230.0003	5.4564	-25.1754	-67.6813	-35.4085	0.9647	4.2192	323.2318
25%	230.4998	15.2462	-15.5838	-5.3028	-9.6122	3.2728	11.2503	474.2568
50%	230.9993	18.3923	-12.6897	1.2295	-3.1859	5.4141	16.2911	519.7802
75%	231.4988	20.8796	-9.0703	7.0004	3.4998	9.6355	22.6642	665.472
max	231.9983	73.0244	32.9782	42.9097	60.4289	118.8092	94.2116	779.0643

(b) Summary table of the data's basic statistics

Figure 4.2: Event and mission definition and basic statistics from the data: number of points, mean, standard deviation, minimum, maximum, and percentiles.

Next, the plot of the magnetic field components will be displayed on screen, with the dates shown along the horizontal axis. The user will then manually select the interval they wish to study, and will be ready to execute the fitting process.

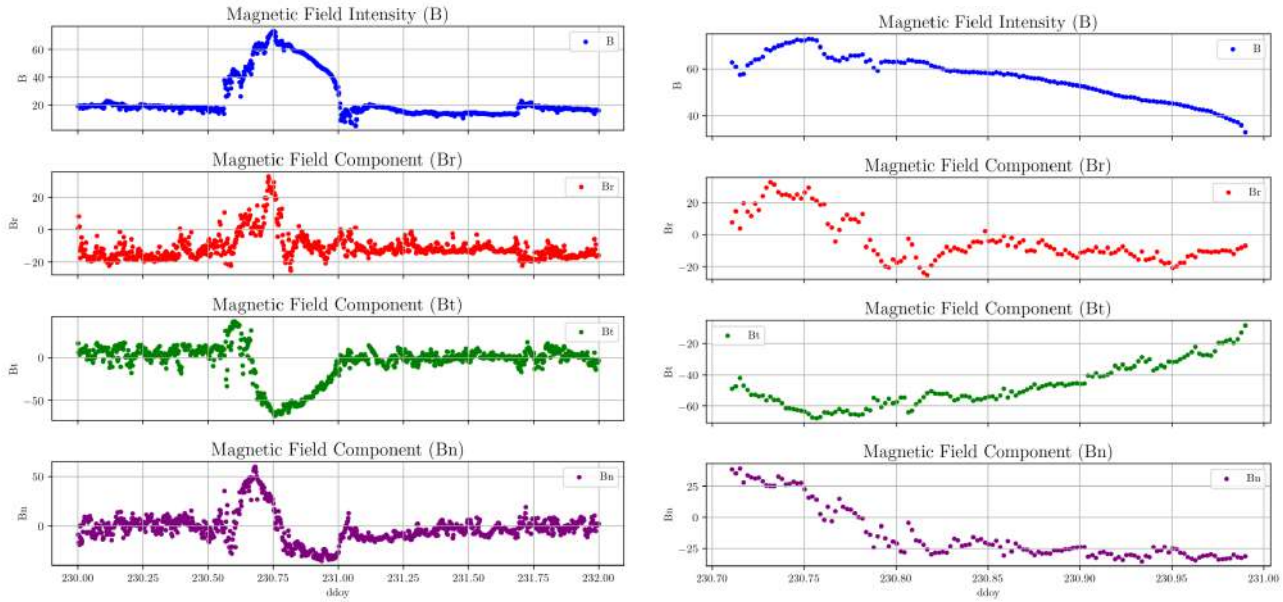

(a) Initial data of the event. **(b)** Selected data.

Figure 4.3: Data selection for the specific event.

Where the criteria for selecting the boundaries within which the event occurs are outlined in the sections 1.3 and 7.

4.3 Solving the geometry for each iteration

4.3.1 Iteration Through All Possible Geometric Configurations

In order to be able to express the in-situ data into the local cylindrical coordinate system, it will be necessary to determine the orientation of the local cylindrical coordinate system and the trajectory of the spacecraft within it. For this, we determine that 5 parameters will be needed:

$$\theta_x,\ \theta_y,\ \theta_z,\ \delta,\ \bar{z}_0 \tag{4.1}$$

Here, the angles θ_x, θ_y, θ_z are those generating Euler rotations with respect to the GSE coordinate system, δ is the deformation of the ellipse, and $\bar{z}_0$ is the entry index in the section (a fraction relative to the maximum point of the section, ranging from -1 to +1).

The following illustrates how the geometry can change with these variables, and what is the domain for each of them.

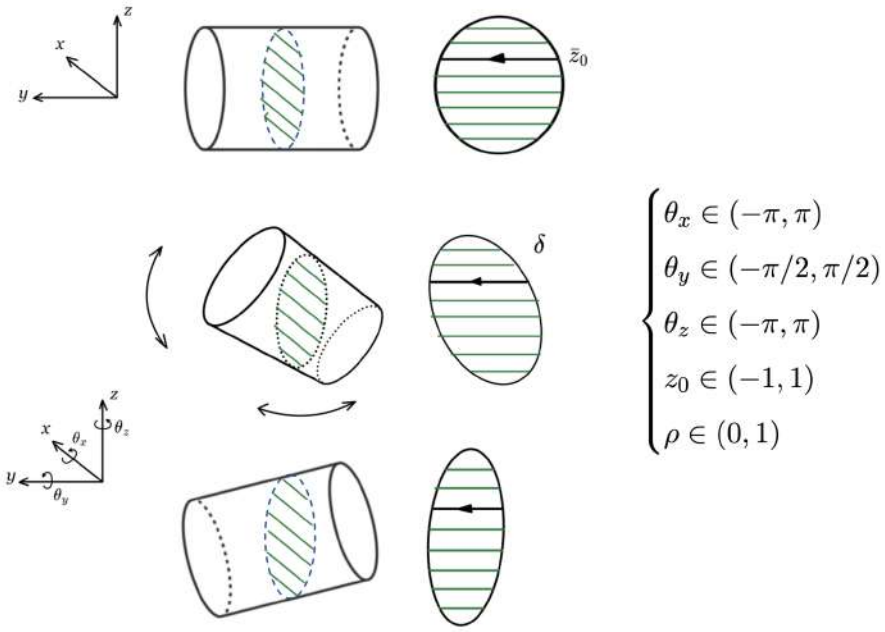

Figure 4.4: Iterations through the geometry configurations

In practical applications, certain extreme values of the fitting parameters lack physical credibility and must be excluded from the optimization domain. For instance, if the axial position parameter $\bar{z}_0$ approaches the bounds of $[-1, 1]$, it implies that the spacecraft trajectory intersects the outermost boundary of the flux rope. However, these peripheral regions exhibit strongly turbulent plasma behavior that deviates from the idealized, laminar model, rendering any fit in these intervals unreliable. Consequently, one adopts the restricted domain:

$$\bar{z}_0 \in (-0.75,\, 0.75)$$

as a physically meaningful range for the axial crossing position.

An analogous argument applies to the distortion factor ρ, which quantifies the ellipticity of the flux rope cross section. Values of ρ approaching zero correspond to an excessively elongated, needle-like ellipse that is not observed in situ. To prevent this unphysical regime, the permissible interval is defined as:

$$\rho \in (0.5,\, 1)$$

ensuring that the fitted cross section remains sufficiently oblate, in order to reflect realistic flux rope geometries.

Finally, the orientation of the flux rope axis itself must also be constrained. Should the inferred axis direction become nearly colinear with the spacecraft's trajectory (i.e., the x–axis in the flux rope frame), the assumption of negligible axial variation (central to our model) would break down. The axial-invariance approximation remains valid only when the spacecraft crosses a narrow local slice of the coronal mass ejection in a transverse direction. To enforce its validity,

one imposes a lower bound on the angle θ_{axis} between the fitted axis and the sampling direction,

$$\theta_{\text{axis}} > \theta_{\text{min}}$$

where θ_{min} is chosen to exclude near-longitudinal intersections that violate the model assumptions.

By imposing these parameter bounds, we ensure that the optimization remains confined to physically plausible regions of the solution space, thereby enhancing both the robustness and the interpretability of the fitted results.

4.3.2 Parametrization of the Trajectory

We start by defining a cylinder in space with arbitrary dimensions (e.g., major axis $a = 1$) and then apply the rotations defined by $\theta_x, \theta_y, \theta_z$:

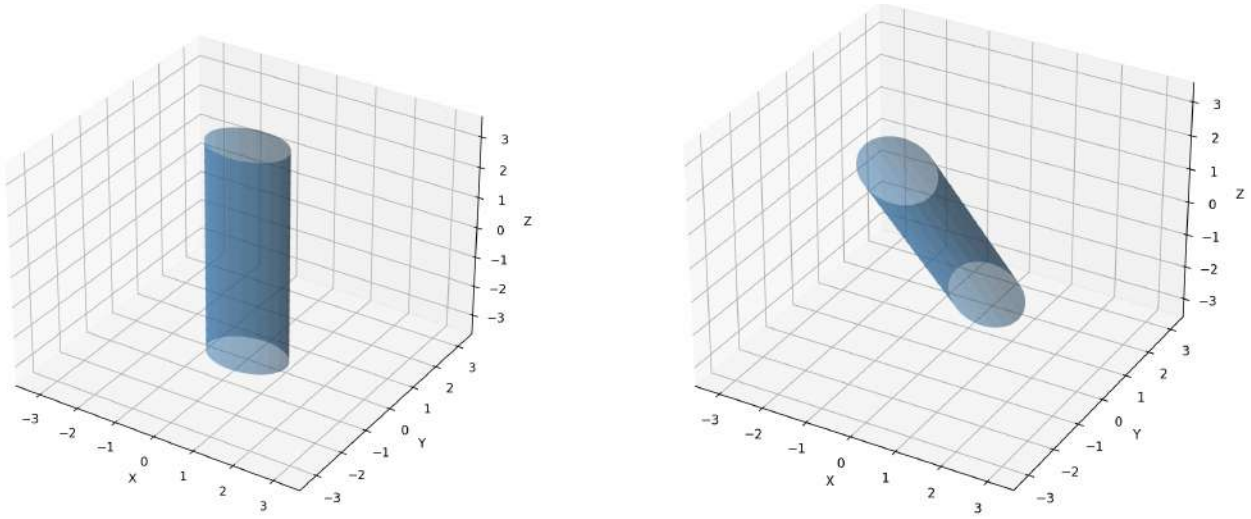

(a) Initial Cylinder **(b)** Rotated Cylinder

The second step involves drawing the satellite's intersection plane inside the magnetic object. Any plane that includes the x-axis would work for this purpose. For example, we will use $y = 0$ to represent the cross-section that the satellite observes inside. The critical point occurs at this stage because the satellite's distance measurement reveals only the length of the flux rope crossing but provides no additional information. For this reason, we will determine the intersection cut distance first before applying a scaling factor to match the satellite's observed distance:

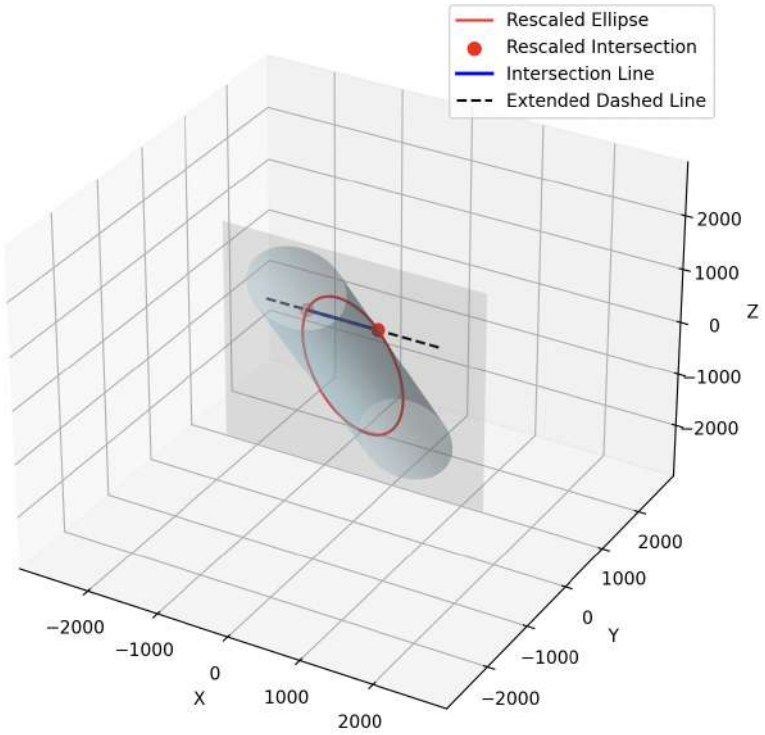

Figure 4.6: Elliptical Section Seen by the Satellite

For this example, we have assumed that the distance traversed by the satellite is 1000 km (much smaller than real scales). This means we will need to adjust the dimensions of the whole object so that the horizontal cut has this length, and by doing this we will have obtained the flux rope geometry and its true dimensions.

On the other hand, the section we are interested in is not the one crossing the plane $y = 0$, but the cross-section of the FR itself! According to the second hypothesis mentioned in the introduction, we assume no variation in the y-coordinate for any component of the magnetic field. For this reason, every slice of the FR exhibits the same magnetic field distribution, and thus we can project the previous cut onto the transversal plane crossing the FR, as shown in Figure 4.7.

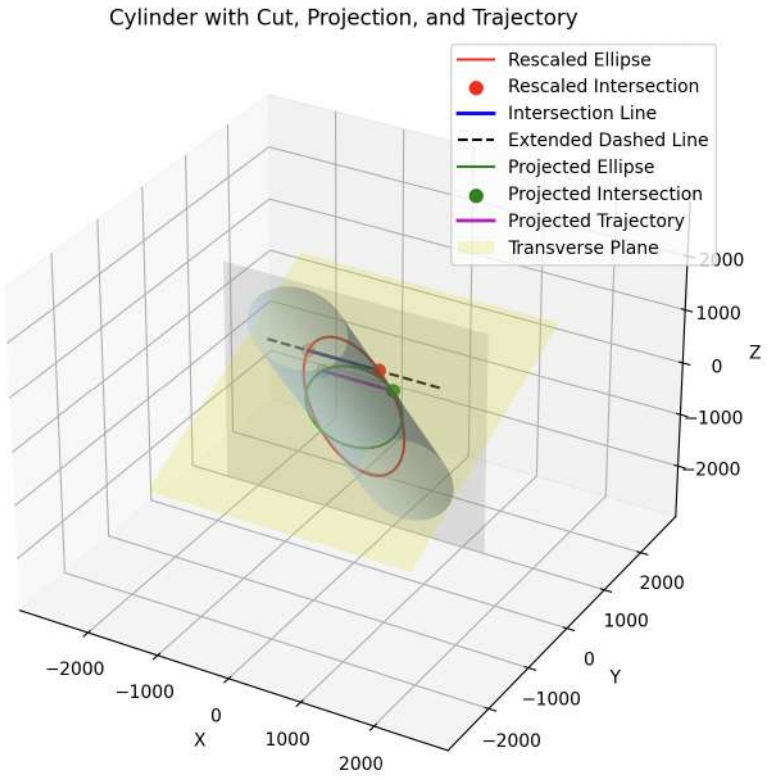

Figure 4.7: Projection of the Ellipse to the Transversal Plane

This will be the section we are interested in, as it will be expressed in the local cylindrical coordinate system. When we plot this new ellipse, we will likely see the satellite's trajectory as non-horizontal. To create a more proper representation, we will apply a rotation to the entire section, as shown below:

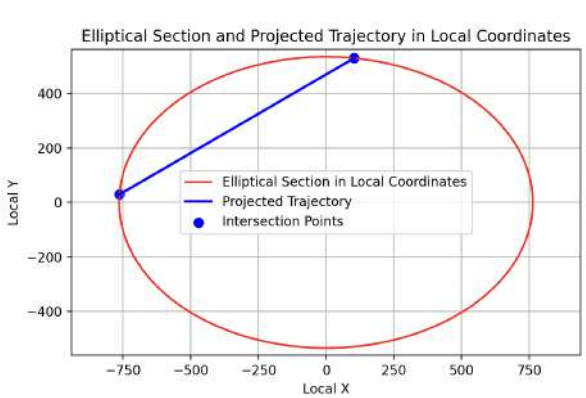

(a) Cross Section

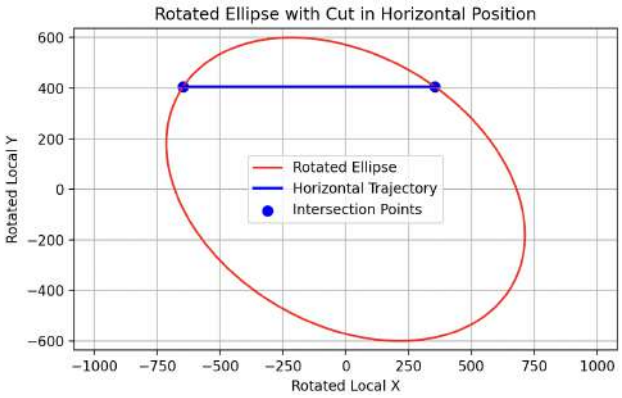

(b) Rotated Cross Section

This entire procedure can be executed analytically by determining the intersection of the $y = 0$ plane with the rotated cylinder, followed by the application of the satellite's trajectory at a specified proportion $\bar{z}_0$. At the end of the process, the user will see an interactive 3D representation of the final structure.

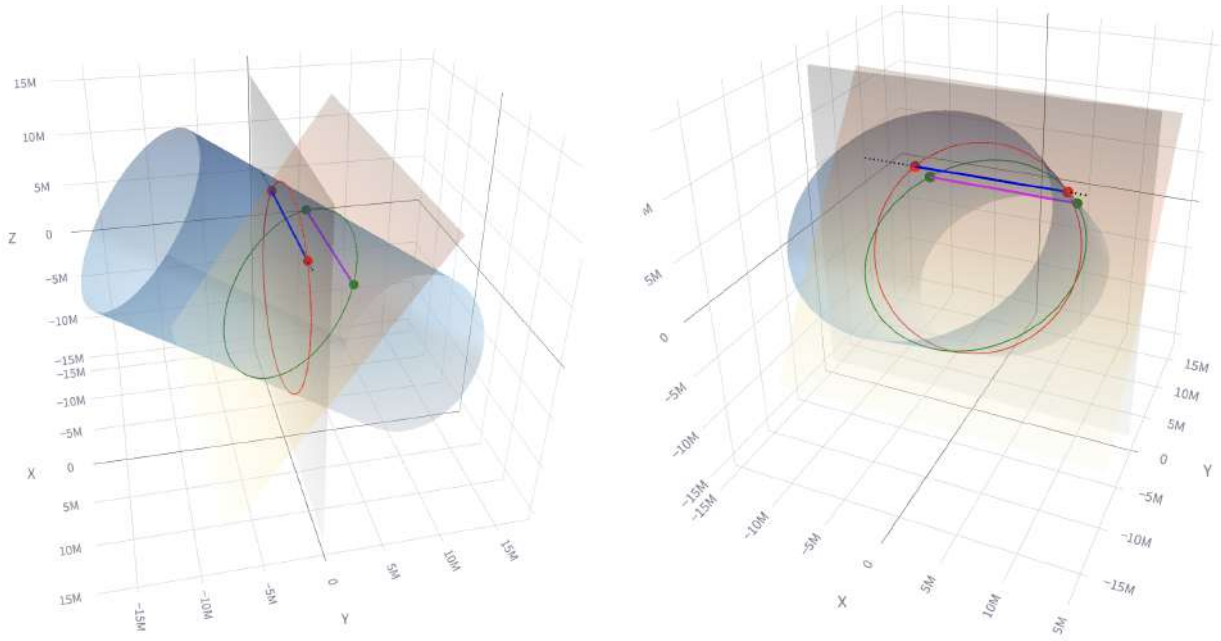

Figure 4.9: Interactive 3D representation of the Flux Rope

In the next section, the mathematical process required for the analytical resolution of the problem will be developed in more detail.

4.3.3 Analytical Solution to the Trajectory for a Given Configuration

For each iteration, we will have a specific combination of the geometric parameters θ_x, θ_y, θ_z, δ, $\bar{z}_0$.

1) The first step is to rotate the cylinder by applying a global rotation matrix. We define the rotation matrices with respect to each of the axes in GSE coordinates as:

$$R_x = \begin{bmatrix} 1 & 0 & 0 \\ 0 & \cos(\theta_x) & -\sin(\theta_x) \\ 0 & \sin(\theta_x) & \cos(\theta_x) \end{bmatrix} \quad R_y = \begin{bmatrix} \cos(\theta_y) & 0 & \sin(\theta_y) \\ 0 & 1 & 0 \\ -\sin(\theta_y) & 0 & \cos(\theta_y) \end{bmatrix} \quad R_z = \begin{bmatrix} \cos(\theta_z) & -\sin(\theta_z) & 0 \\ \sin(\theta_z) & \cos(\theta_z) & 0 \\ 0 & 0 & 1 \end{bmatrix}$$

The total rotation matrix R is computed as the product $R = R_y R_x R_z$. Using this rotation matrix, we orient the Flux Rope according to the configuration for the current iteration. The rotated elliptical cylinder is then defined by the following coordinates:

$$\begin{pmatrix} x \\ y \\ z \end{pmatrix} = R \begin{pmatrix} a\ \cos(\varphi) \\ y_c \\ a\delta \sin(\varphi) \end{pmatrix} = \tag{4.2}$$

$$\begin{pmatrix} a(\cos\theta_z \cos\theta_x + \sin\theta_z \sin\theta_x \sin\theta_x)\cos\varphi + \sin\theta_z \cos\theta_x y_c + a\delta(\cos\theta_z \sin\theta_x - \sin\theta_z \sin\theta_x \cos\theta_x)\sin\varphi \\ a(-\sin\theta_z \cos\theta_x + \cos\theta_z \sin\theta_x \sin\theta_x)\cos\varphi + \cos\theta_z \cos\theta_x y_c - a\delta(\sin\theta_z \sin\theta_x + \cos\theta_z \sin\theta_x \cos\theta_x)\sin\varphi \\ -a\cos\theta_x \sin\theta_x \cos\varphi + y_c \sin\theta_x + a\delta \cos\theta_x \cos\theta_x \sin\varphi \end{pmatrix}$$

From now on, considering that the three rotation angles are known, we will use the following notation:

$$\begin{pmatrix} x \\ y \\ z \end{pmatrix} = \begin{pmatrix} aA\cos\varphi + B\,y_c + aC\sin\varphi \\ aD\cos\varphi + E\,y_c + aF\sin\varphi \\ aG\cos\varphi + H\,y_c + aI\sin\varphi \end{pmatrix} \tag{4.3}$$

2) The next step is to define the cutting section with the plane $y = 0$. It is important to note here that the variable y_c refers to the local y coordinate of the original cylinder, but now we are working with absolute coordinates, so in the cutting plane, y_c does not necessarily have to be zero. The cutting section will then be given by:

$$\begin{pmatrix} x \\ 0 \\ z \end{pmatrix} = \begin{pmatrix} aA\cos\varphi + B\,y_c + aC\sin\varphi \\ aD\cos\varphi + E\,y_c + aF\sin\varphi \\ aG\cos\varphi + H\,y_c + aI\sin\varphi \end{pmatrix} \tag{4.4}$$

This defines an ellipse in the plane $y = 0$. This results in three equations that we need to solve.

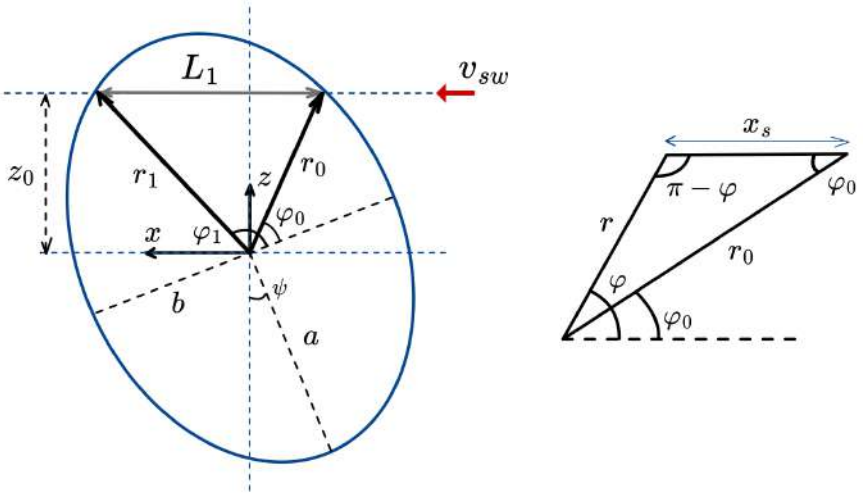

Figure 4.10: Trajectory parameters representation

3) We can start with the first equation:

$$x = aA\cos\varphi + B\,y_c + aC\sin\varphi \tag{4.5}$$

the information we have here is the following: we know that the spacecraft crosses the magnetic structure going along the x axis in the GSE coordinates, and the length traversed by the spacecraft inside it, given by $L_1 = t_{sw}v_{sw}$. We will use this to impose the following condition:

$$x_1 - x_0 = L_1 = a(A\cos\varphi_1 + C\sin\varphi_1) + By_{c,1} - By_{c,0} - a(A\cos\varphi_0 + C\sin\varphi_0) \tag{4.6}$$

Where the x_0 and x_1 points correspond to the x coordinate at the entrance and at the output of the Flux Rope. Therefore, from here we obtain the first relation:

$$\boxed{a = \frac{L_1 - By_{c,1} + By_{c,0}}{(A\cos\varphi_1 + C\sin\varphi_1) - (A\cos\varphi_0 + C\sin\varphi_0)}} \tag{4.7}$$

Apart from that, we can also introduce two more equations to provide the formulas for x_0 and x_1, in this case introducing two additional variables: r_0 and r_1. These will not be used right now to solve the system, but they will be important later for the parametrization of the trajectory.

$$x_0 = r_0\cos(\varphi_0) \qquad\qquad x_1 = r_1\cos(\varphi_1) \tag{4.8}$$

4) The next thing we will do is analyze the y equation.

$$0 = aD\cos\varphi + Ey_c + aF\sin\varphi \tag{4.9}$$

This must hold at every point along the ellipse. Therefore, we can obtain the value of y_c at the entrance and exit of the FR as follows:

$$y_c = -\frac{a(D\cos\varphi + F\sin\varphi)}{E} \tag{4.10}$$

$$\boxed{y_{c,0} = -\frac{a(D\cos\varphi_0 + F\sin\varphi_0)}{E}} \qquad \boxed{y_{c,1} = -\frac{a(D\cos\varphi_1 + F\sin\varphi_1)}{E}} \tag{4.11}$$

We now observe that we have 3 equations and 5 variables: a, $y_{c,0}$, $y_{c,1}$, φ_0, φ_1. We still need two more equations to obtain a fully determined system. Let us now proceed to the last component: z.

5) From the z equation, we know that the trajectory will be horizontal, with a constant z_0.

$$z_0 = aG\cos\varphi + Hy_c + aI\sin\varphi \quad \Rightarrow \quad \frac{z_0 - Hy_c}{a} = G\cos\varphi + I\sin\varphi \equiv K \tag{4.12}$$

We have rewritten the equation to better isolate the trigonometric components.

We know there will be two angles at which the spacecraft trajectory intersects the elliptical section. We can solve this system by rewriting $\sin\varphi = \sqrt{1-\cos^2\varphi}$, isolating the cosine, and squaring both sides. This leads to a quadratic equation, and solving it we obtain:

$$\cos\varphi = \frac{KG \pm I\sqrt{G^2 + I^2 - K^2}}{G^2 + I^2} \tag{4.13}$$

From this, we obtain the final two equations needed to solve the system:

$$\boxed{\cos\varphi_0 = \frac{\frac{z_0 - Hy_{c,0}}{a}\cdot G - I\sqrt{G^2 + I^2 - \left(\frac{z_0 - Hy_{c,0}}{a}\right)^2}}{G^2 + I^2}} \tag{4.14}$$

$$\boxed{\cos\varphi_1 = \frac{\frac{z_0 - Hy_{c,1}}{a}\cdot G + I\sqrt{G^2 + I^2 - \left(\frac{z_0 - Hy_{c,1}}{a}\right)^2}}{G^2 + I^2}} \tag{4.15}$$

However, we now observe that a new variable has been introduced: z_0.

6) Determination of z_0:

We begin, for example, by finding the maximum height of the ellipse. We can find this by deriving the z variable with respect to the angle and identifying the angle that maximizes or minimizes the height:

$$\frac{\partial z}{\partial \varphi} = 0 = -G\sin\varphi + I\cos\varphi \quad \Rightarrow \quad \boxed{\tan\varphi_{z_{max}} = \frac{I}{G}} \quad \Rightarrow \quad \varphi_{z_{max}} \tag{4.16}$$

Before substituting this value into the z equation, we need the corresponding y_c value. Solving again, we obtain:

$$\boxed{y_{c,z_{max}} = -\frac{a(D\cos\varphi_{z_{max}} + F\sin\varphi_{z_{max}})}{E}} \tag{4.17}$$

$$\boxed{z_{max} = aG\cos\varphi_{z_{max}} + Hy_{c,z_{max}} + aI\sin\varphi_{z_{max}}} \tag{4.18}$$

And finally, we can use the relation:

$$\boxed{z_0 = \bar{z}_0 \cdot z_{max}} \tag{4.19}$$

7) Trajectory Parametrization:

Now, the system is completely solved, and we just need to find how to parametrize the trajectory. That means, finding the array of r values along the path, as well as the array for the φ values.

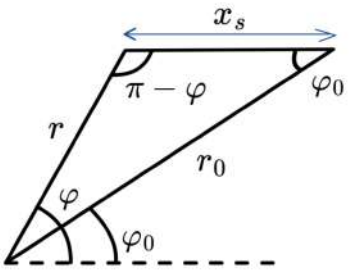

Figure 4.11: Relation of variables along the trajectory

- ◇ **Cosine Theorem:** $r^2 = a^2 + r_0^2 - 2x_s r_0 \cos(\varphi_0)$
- ◇ **Sine Theorem:** $\frac{x_s}{\sin(\varphi - \varphi_0)} = \frac{r}{\sin(\varphi_0)}$

By substituting and simplifying, we obtain the following expression:

$$r^2 \left[\left(\frac{\sin(\varphi - \varphi_0)}{\sin \varphi_0} \right)^2 - 1 \right] + 2r_0 \cos(\varphi - \varphi_0) \cdot r = r_0^2 \quad \Rightarrow \quad r = r(\varphi) \tag{4.20}$$

8) Projection to the Transversal Plane:

With the previous process, we obtain the parametrization of the section and the trajectory within the plane $y = 0$. However, we are interested in knowing this parametrization in a generic cross-section of the cylinder. As mentioned earlier, we will use the assumption that there is no variation in the physical properties along the axial component of the cylinder, and therefore we can project the points found onto a single plane transversal to the cylinder's axis.

Thus, we begin by taking the axis of the cylinder after the rotation, which will be the normal vector to the plane of interest. This vector is given by:

$$\mathbf{n}_{axis} = R \begin{pmatrix} 0 \\ 1 \\ 0 \end{pmatrix} = \begin{bmatrix} -\cos(\theta_y)\sin(\theta_z) + \sin(\theta_y)\sin(\theta_x)\cos(\theta_z) \\ \cos(\theta_x)\cos(\theta_z) \\ \sin(\theta_y)\sin(\theta_z) + \cos(\theta_y)\sin(\theta_x)\cos(\theta_z) \end{bmatrix} \tag{4.21}$$

Let this axis be denoted as $\mathbf{n}_{axis} = (n_x, n_y, n_z)$. The transversal plane is perpendicular to $\mathbf{n}$, and its equation can be written as:

$$n_x x + n_y y + n_z z = d \tag{4.22}$$

where d is the distance from the origin to the plane, determined by a point on the plane (e.g., the center of the ellipse in the $y = 0$ plane). We will assume $d = 0$, as the origin coordinate system was not displaced. Thus, the transversal plane is defined by:

$$n_x x + n_y y + n_z z = 0 \tag{4.23}$$

What we will need to do now is to project the found section into this other plane. To do that, we will need to use the formula for the projection of a point $\mathbf{p} = (x, 0, z)$ onto a plane with normal $\mathbf{n}$:

$$\mathbf{p}_{\text{proj}} = \mathbf{p} - \frac{\mathbf{n} \cdot (\mathbf{p} - \mathbf{p}_0)}{\|\mathbf{n}\|^2}\mathbf{n} \tag{4.24}$$

And considering that the plane contains the origin, we simplify $\mathbf{p}_0 = 0$:

$$\boxed{\mathbf{p}_{\text{proj}} = \mathbf{p} - \frac{\mathbf{n} \cdot \mathbf{p}}{\|\mathbf{n}\|^2}\mathbf{n}} \tag{4.25}$$

Substituting $\mathbf{p} = (x(\varphi), 0, z(\varphi))$, we compute:

$$\mathbf{p}_{\text{proj}}(\varphi) = \begin{pmatrix} x(\varphi) \\ 0 \\ z(\varphi) \end{pmatrix} - \frac{n_x x(\varphi) + n_z z(\varphi)}{n_x^2 + n_y^2 + n_z^2} \begin{pmatrix} n_x \\ n_y \\ n_z \end{pmatrix} \tag{4.26}$$

This gives the coordinates $(x_{\text{proj}}, y_{\text{proj}}, z_{\text{proj}})$ of the projected trajectory in the transversal plane. The radial distance r_{proj} and angular position φ_{proj} in this plane can then be computed relative to the cylinder's axis projected onto the plane.

Once we reach this point, we have defined the internal trajectory of the satellite inside the FR, and we can extract the values of the radial distance to the FR axis or its angular position, which will later be used to express the in-situ data in this new coordinate system. For this case, for example, the parametrized radial distance and angular position of the spacecraft along the cut take this form:

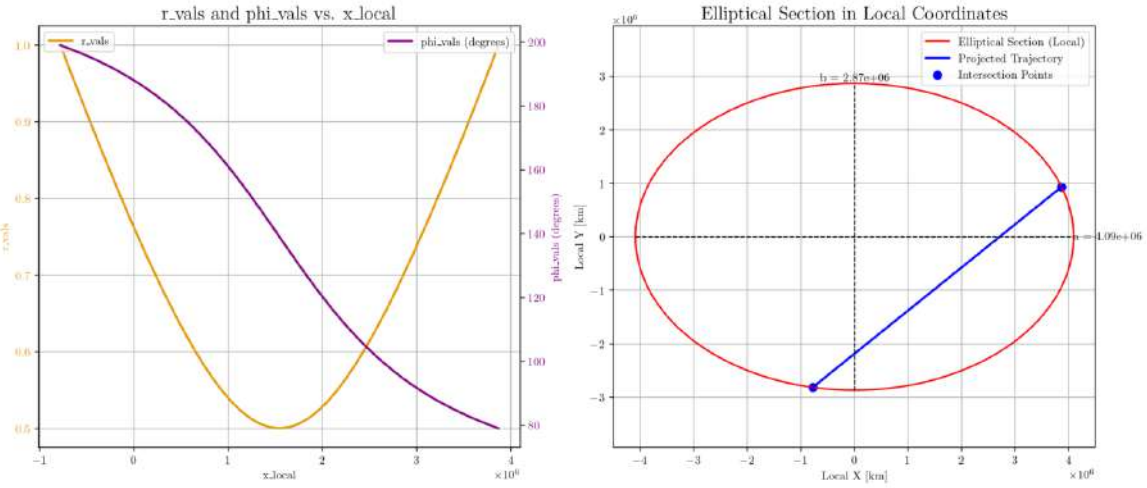

Figure 4.12: Angular and Radial Coordinates Along the Trajectory

The most important thing we obtain here are the trajectory angles in the local coordinates, which we will later use for the change of coordinates (φ_{sat}).We also determine the radial distance (r_{sat}, which will be used to evaluate the magnetic field models along the spacecraft's path.

4.4 Change of Coordinates of the In-Situ Data

Once we have the configuration well defined and parametrized, we will proceed to change the basis of the in-situ measurements and express them in the local cylindrical coordinate system of the magnetic flux rope. This is necessary because the models used for each component of the magnetic field are defined in that frame. Therefore, we must map the in-situ data into that system in order to determine which field configuration best matches the experimental observations.

To perform this transformation, we begin by expressing the magnetic field $\mathbf{B}$, which was originally in GSE (*Geocentric Solar Ecliptic*) coordinates, in a local Cartesian frame; and then we apply a second change of basis to express it in the local cylindrical frame adapted to the flux rope's geometry.

4.4.1 Transformation from GSE to Local Cartesian

The relationship between the components in the GSE coordinate system and the local Cartesian frame is given by the global rotation matrix of the system, defined previously as $R = R_y R_x R_z$:

$$\mathbf{B}_{\text{local}} = R \cdot \mathbf{B}_{\text{GSE}} \tag{4.27}$$

where $\mathbf{B}_{\text{local}} = \left(B_x^{\text{local}}, B_y^{\text{local}}, B_z^{\text{local}}\right)$ and $\mathbf{B}_{\text{GSE}} = \left(B_x^{\text{GSE}}, B_y^{\text{GSE}}, B_z^{\text{GSE}}\right)$. The matrix R is

designed to align the GSE axes with the local axes, which are defined by the orientation of the flux-rope axis or the spacecraft trajectory. Since we are still in an orthonormal frame, the total magnetic field magnitude is simply

$$B_{\text{local,total}} = \sqrt{\left(B_x^{\text{local}}\right)^2 \; + \; \left(B_y^{\text{local}}\right)^2 \; + \; \left(B_z^{\text{local}}\right)^2}.$$

This will serve as a consistency check as the coordinate system is transformed. Upon switching to the non-orthogonal basis inside the cylinder, the magnitude of $\mathbf{B}$ must be conserved. To ensure this, the procedure developed in the next section must be followed.

4.4.2 Transformation from Local Cartesian to Elliptical-Cylindrical

As explained in Section 3.1, the elliptical-cylindrical coordinate system is not orthogonal. Its basis vectors are neither unitary nor mutually orthogonal, yet the resulting vector must remain invariant under any change of basis.

In the local Cartesian frame we write:

$$\mathbf{B}_{\text{local}} = B^x \, \hat{x} \; + \; B^y \, \hat{y} \; + \; B^z \, \hat{z}. \tag{4.28}$$

This must equal the representation in elliptical-cylindrical components:

$$\mathbf{B}_{\text{cyl}} = B^r \, \varepsilon_r \; + \; B^y \, \varepsilon_y \; + \; B^\varphi \, \varepsilon_\varphi. \tag{4.29}$$

Where the vectors ε_i are those we previously defined in 3.3. A direct relationship between components is obtained by projecting the total vector onto each basis vector. The quickest approach is to project $\mathbf{B}_{\text{cyl}}$ onto the Cartesian unit vectors:

$$B_L^x = \hat{x} \cdot \mathbf{B}_{\text{cyl}} \qquad B_L^y = \hat{y} \cdot \mathbf{B}_{\text{cyl}} \qquad B_L^z = \hat{z} \cdot \mathbf{B}_{\text{cyl}}, \tag{4.30}$$

which yields the transformation matrix:

$$\begin{pmatrix} B_x \\ B_y \\ B_z \end{pmatrix}_L = \begin{pmatrix} a\cos\varphi & 0 & -a\,r\sin\varphi \\ 0 & 1 & 0 \\ a\,\delta\sin\varphi & 0 & \delta\,a\,r\cos\varphi \end{pmatrix} \begin{pmatrix} B^r \\ B^y \\ B^\varphi \end{pmatrix}_{\text{Cyl}} \tag{4.31}$$

Note that the y-component remains unchanged, since it is identical in both the local Cartesian and elliptical–cylindrical frames. Moreover, because the local system is orthonormal, it makes no difference whether one uses contravariant or covariant components, and we can simply place

the index as a subscript to avoid confusing it with an exponent.

Finally, to recover the elliptical-cylindrical components from the Cartesian ones, we apply the inverse transformation:

$$\mathbf{B}_{\text{local}} = A\,\mathbf{B}_{\text{cyl}} \quad \Longrightarrow \quad \mathbf{B}_{\text{cyl}} = A^{-1}\,\mathbf{B}_{\text{local}}. \tag{4.32}$$

With this, we obtain each component of the in-situ measured magnetic field in the local elliptical-cylindrical system and can proceed to fit our magnetic field models.

Finally, we can compute the magnitude in cylindrical coordinates to confirm agreement with the Cartesian result, using equation 3.4:

$$B^{\text{cyl}}_{\text{total}} = \sqrt{g_{rr}\,(B^r)^2 \;+\; g_{yy}\,(B^y)^2 \;+\; g_{\varphi\varphi}\,(B^\varphi)^2 \;+\; 2\,g_{r\varphi}\,B^r\,B^\varphi}.$$

4.4.3 Representation in the Cross Section

Subsequently, if we wish to represent the magnetic field components in the elliptical–cylindrical coordinate system, there are two approaches. On the one hand, we can plot the raw contravariant components (the coefficients multiplying each director vector ε_i); but also, we can examine those components rescaled so that they multiply a unit vector, as is common in studies such as [21]. In practical terms, this makes no difference for the fitting process, as long as we remain consistent and ensure that the magnetic field magnitude is preserved throughout the analysis. However, the rescaled view can be illustrative if we want to show what the spacecraft actually "sees" along each specific direction.

If we choose to plot the scaled components in the cross-section, we must multiply each magnetic field component by the norm of its corresponding director vector. Following the notation of [20], we denote the rescaled components with a subscript c, and the scale factors for each component are:

$$\begin{cases} h_r = \|\varepsilon_r\| = a\sqrt{\cos^2\varphi + \delta^2\sin^2\varphi}, \\ h_y = \|\varepsilon_y\| = 1, \\ h_\varphi = \|\varepsilon_\varphi\| = ra\sqrt{\sin^2\varphi + \delta^2\cos^2\varphi}, \end{cases} \quad \Rightarrow \quad \begin{cases} B^r_c = h_r\,B^r, \\ B^y_c = h_y\,B^y, \\ B^\varphi_c = h_\varphi\,B^\varphi. \end{cases} \tag{4.33}$$

Since B^r remains zero and B^y is unchanged, only B^φ is affected in the representation. Below is an example for the case where B^φ takes the form:

$$B_\varphi(r) \;=\; 1.3065\cdot 10^{-28}\,r^3 \;-\; 5.2897\cdot 10^{-18}\,r^2 \;+\; 5.2655\cdot 10^{-8}\,r. \tag{4.34}$$

Its representation in the cross section can be shown in these two ways:

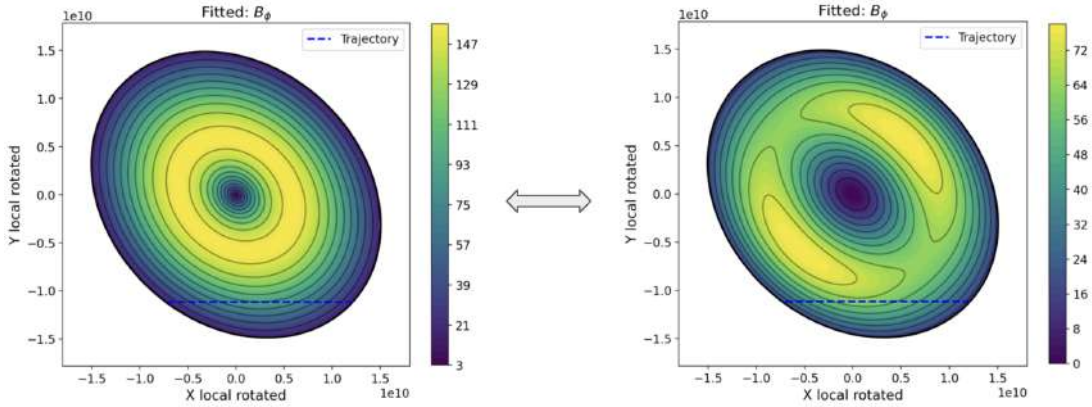

Figure 4.13: Original contravariant component (B^φ) and its rescaled version (B_c^φ) within the elliptical cross section.

However, as noted, both the axial component and the total field magnitude are identical in each case. Assuming we have the following expression for B^y, their representations would be the ones shown in Figure 4.14.

$$B_y(r,\varphi) = 3.02 \cdot 10^{-30}\, r^3\big(0.1\,\sin(\varphi + 4.45 \cdot 10^{-32}) + 0.1\,\cos(\varphi + 4.45 \cdot 10^{-32}) + 0.5\big) + 17.74.$$

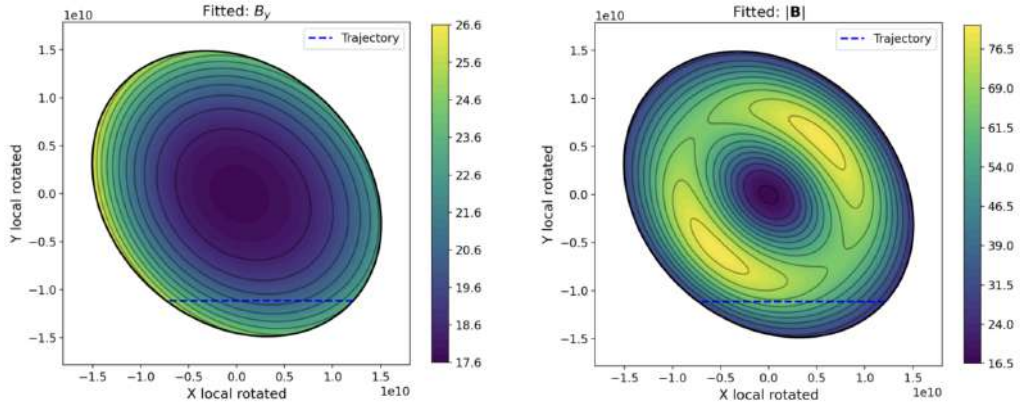

Figure 4.14: B^y and **B** representations in the cross section. The scaled and non-scaled views coincide.

We conclude that this distinction may be relevant for graphical representations, but it does not affect the internal solution process. In subsequent steps, we will always work directly with the contravariant components without any rescaling.

4.5 Fitting the Model to Experimental Data

4.5.1 Fitting in the Local Cylindrical Coordinate System

Once in the cylindrical-elliptical system, we will determine the parameters of our magnetic field model that best fit the experimental data. To achieve this, we will use the least-squares fitting method, which involves minimizing the difference between the experimental data $\left(B^r_{\text{exp}},\ B^y_{\text{exp}},\ B^\varphi_{\text{exp}}\right)$ and the values predicted by the models for each magnetic field component.

Considering N experimental points, $\{(x_i, y_i)\}_{i=1}^N$, where in our case $x_i = (r_i, \alpha_i)$, and y_i is the experimentally measured value of each component at those points, we can express:

$$y_i = f(x_i; \theta) + \varepsilon_i \tag{4.35}$$

Here, $f(x_i; \theta)$ is the function corresponding to each model B_i, θ represents the fitting parameters for each model, and ε_i are the independent errors for each point.

The main objective of nonlinear least-squares regression involves minimizing the total squared differences between observed and predicted values.

$$S(\theta) = \sum_{i=1}^{N} [y_i - f(x_i; \theta)]^2 \tag{4.36}$$

The method operates under the condition that $\varepsilon_i \sim N(0, \sigma^2)$. The Python library `scipy.optimize` contains the `curve_fit` function which computes the maximum likelihood estimator $\hat{\theta}$. The function implements two optimization algorithms which are Gauss-Newton and Levenberg-Marquardt.

The algorithm will be used in our code to find the optimal parameters that match the experimental data points for each magnetic field component.

For the case of the simplified radial model 3.47, in one of the program's iterations we may encounter something like the following:

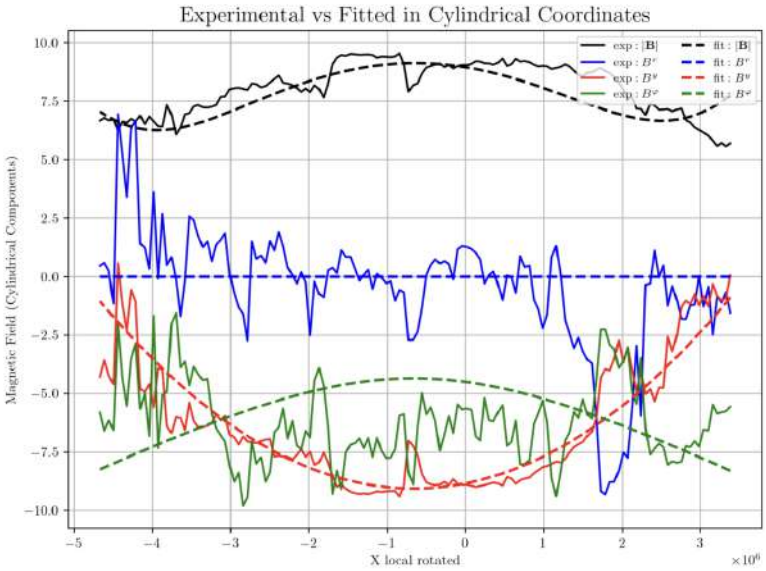

Figure 4.15: Fitted in-situ data in the cylindrical reference frame.

However, this is by no means the end of our fitting code. Even if the data fit in cylindrical coordinates is very accurate, the fit may be very poor when transformed back to the GSE coordinate system.

4.5.2 Transformation of Coordinates to the GSE System

The final step to compare the experimental values with the proposed model will be to transform the fitted data back to the GSE coordinate system. To do this, we simply apply the inverse transformations of those performed so far. To go to the local Cartesian coordinate system, we use expression 4.31, and then, to go from local to GSE, we use the inverse of 4.27, i.e.:

$$\mathbf{B}_{\text{local}} = A\,\mathbf{B}_{\text{cyl}} \qquad\qquad \mathbf{B}_{\text{GSE}} = R^{-1} \cdot \mathbf{B}_{\text{Local}} \tag{4.37}$$

With this, we will have succeeded in expressing the modeled values of each field in the original reference system, and we can now evaluate the results.

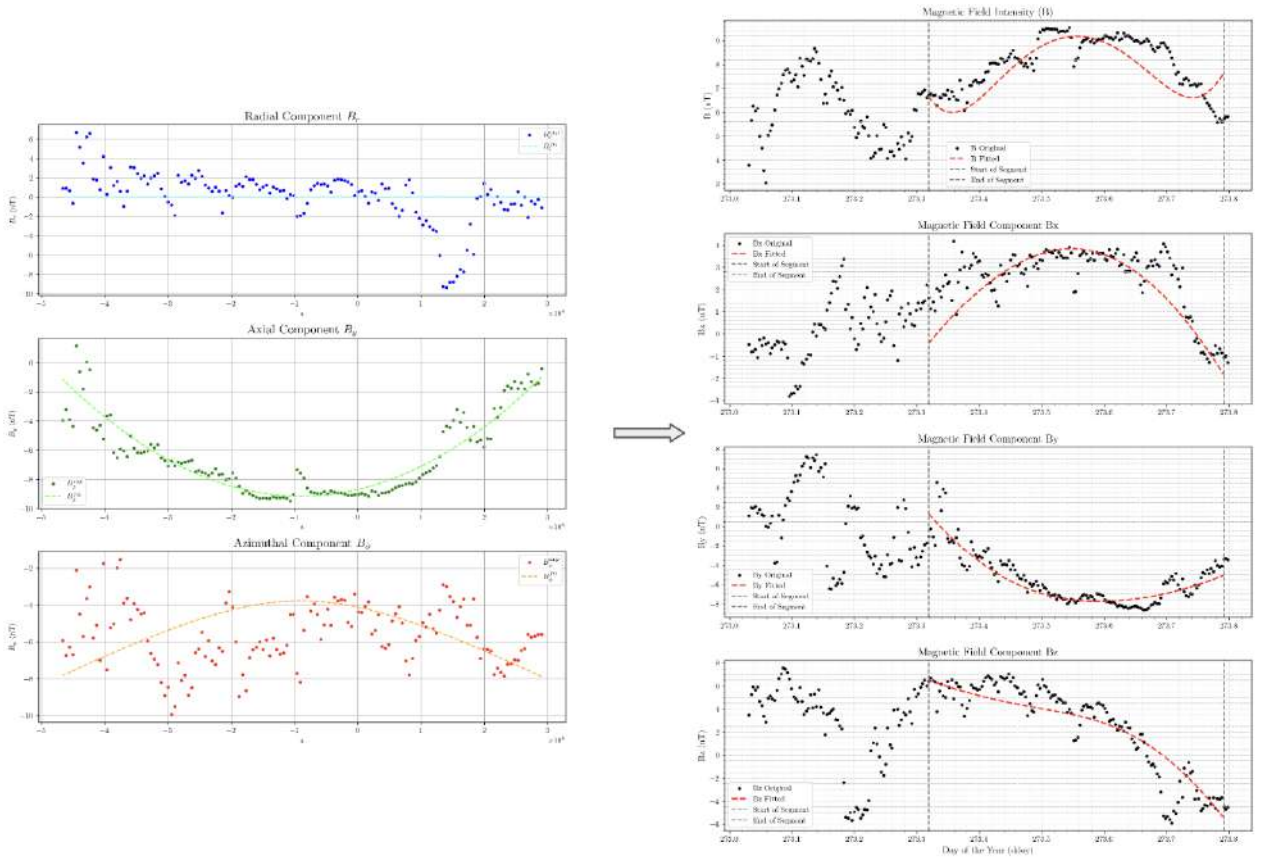

Figure 4.16: Fit of the values in the local cylindrical coordinate system and their subsequent representation in the GSE system.

A good fit in the local cylindrical coordinate system only tells us how well the proposed model adapts to the experimental data seen by the satellite for a given flux rope orientation. However, the final way to check its validity is by checking the results once we are again in the GSE coordinate system. Therefore, we will focus on maximizing quality based on this final result.

4.6 Fit Quality Criteria

Finally, the last step within the main loop will involve numerically evaluating the quality of the fit, based on its results in the GSE frame. If a given iteration is determined to be better than previous ones, the corresponding parameter values will be saved, and the loop will continue. When choosing the statistical criterion to determine quality, we can particularly hesitate between two options:

- ◇ **Coefficient of determination R^2:** In case our main objective is to minimize the squared discrepancy between fitted and observed values, then R^2 is the natural choice. It directly measures the fraction of variance explained by the model.
- ◇ **Pearson correlation coefficient ρ:** The experimental series can be evaluated for point-to-point linear agreement with normalized fitted values.

In fully multivariate systems where multiple unknowns are optimized simultaneously and one wants a single global metric, Pearson's ρ can be particularly effective, as shown by Nieves-Chinchilla et al. [17]. However, since in our case we estimate only the physical model parameters while iterating over the geometric variables, minimizing the fitting error via R^2 is the most coherent approach.

4.6.1 Coefficient of Determination R^2

The coefficient of determination R^2 measures the fraction of the total variability that the model manages to explain. For measured data $\{y_i\}$ and their predictions $\{\hat{y}_i\}$ it is defined:

$$R^2 \;=\; 1 \;-\; \frac{\displaystyle\sum_{i=1}^{n}(y_i - \hat{y}_i)^2}{\displaystyle\sum_{i=1}^{n}(y_i - \bar{y})^2}$$

Where the domain is $-\infty < R^2 \leq 1$. If we obtain a value close to 1, it means that the fit is good, since almost all of the variance in the data is explained. If the value is less than 0, it means that the fit is worse than if we had simply taken the mean of all the values.

Since we will perform 3 separate fits for (B_x, B_y, B_z) (in addition to later computing the magnitude from the fitted values), we will define a global coefficient of determination by averaging the individual ones:

$$R^2_{\text{avg}} = \frac{1}{4}\big(R^2_B + R^2_{B_x} + R^2_{B_y} + R^2_{B_z}\big).$$

The maximization of this parameter will be the chosen criterion to determine how good the obtained fit is.

4.7 Computation of the Current Density

Finally, once the entire fitting procedure has been completed and the internal magnetic field characteristics are known, the resulting equations for the current density inside the Flux Rope can be derived, as well as other derived physical properties of the flux.

The formulas that define the internal current field can be obtained analytically, as done in Chapter 3. A possible example of the results is shown in Figure 4.17, corresponding to the PSP event of August 18, 2022, also studied later in Section 7.1.

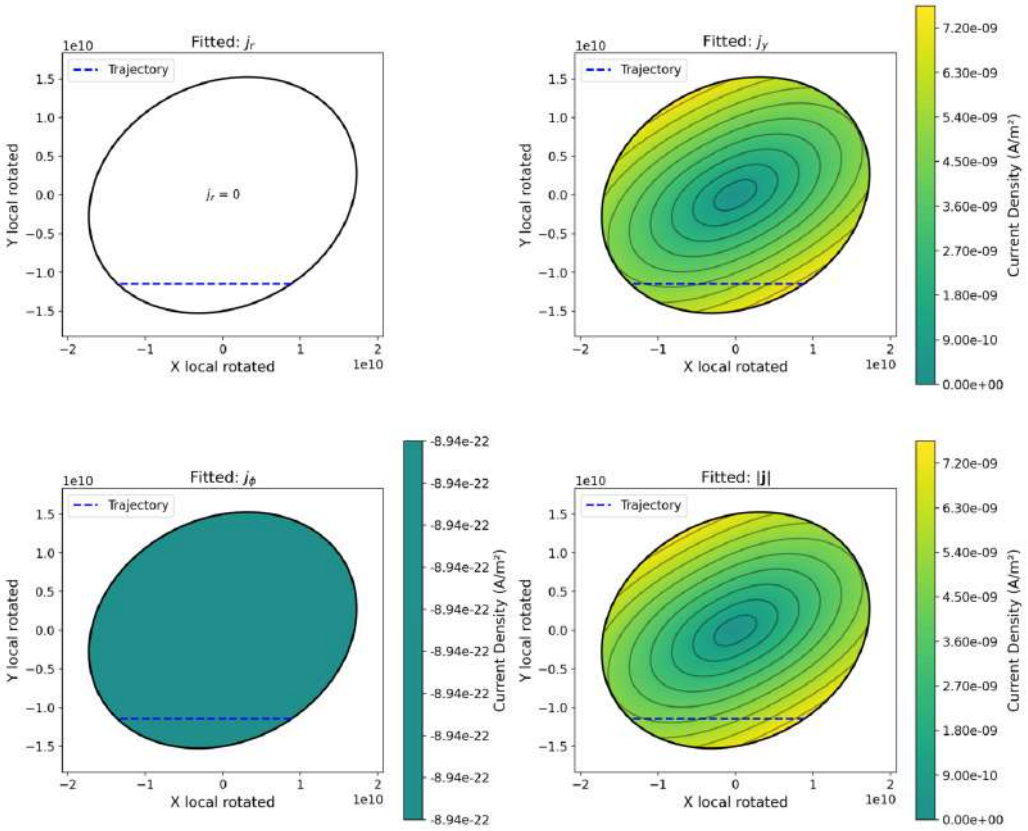

Figure 4.17: Current density field for the Simplified Radial Model

This final calculation is not relevant to the fitting process itself, but it is a necessary part of the modeling process, in order to verify visually that any proposed model has physical validity.

5 . Validation of the Model

To validate this fitting algorithm, two complementary methodologies were implemented. First, the fit was applied to a synthetic flux rope, followed by a convergence study of the adjusted parameters. Then, it was applied to previously studied real events detected in situ.

5.1 Synthetic Flux Rope Generation

The first fundamental step for any model-fitting algorithm is to perform a verification test using synthetic data. In this case, a flux rope with a known orientation and internal magnetic field was generated synthetically, and it was assumed that the satellite crosses it along a prescribed trajectory. What we aim to verify is whether, from the data recorded by the satellite, the algorithm can deduce the flux rope's orientation and the conditions under which the satellite intersected this magnetic structure. The procedure is outlined below.

5.1.1 Generation of the Geometry

To determine the size, shape, and orientation of the magnetic flux rope, one must define at least the following parameters: L_1 (length of the path traversed by the satellite), δ (section distortion), $\bar{z}_0$ (relative entry height of the satellite), and the rotation angles θ_x, θ_y, and θ_z.

To assign a value to the length L_1, we assumed a typical solar wind speed encountered in flux ropes of $V_{sw} = 430$ km/s. We also assumed the event duration to be one day (24h), so the total detected length would be approximately 0.248AU. The other geometric parameters were set to the following values:

$$\delta = 0.7, \qquad z_0 = 0.3, \qquad \theta_x = 45°, \qquad \theta_y = 30°, \qquad \theta_z = -30° \tag{5.1}$$

Using these values and following the calculations presented in Section 4.3, we can determine the final orientation of the flux rope, its dimensions, the spacecraft's internal trajectory, and its parametrization in elliptical–cylindrical coordinates. The result for this case is shown in Figure 5.1.

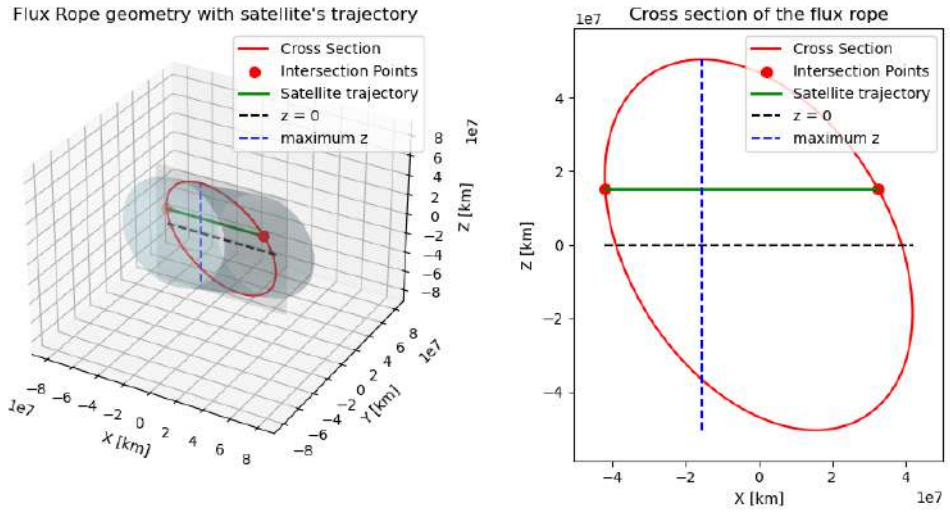

Figure 5.1: Synthetic flux rope geometry creation.

5.1.2 Generation of the Magnetic Field Data

Next, we define the internal magnetic field for this flux rope. Based on the conditions outlined in Section 3.3.2, we propose the following basic model for this simulation:

$$B^r = 0, \qquad B^y = 1 - r^2, \qquad B^\varphi = r \tag{5.2}$$

The representation of their scaled versions, using the relations from 4.33 are shown in the Figure 5.2.

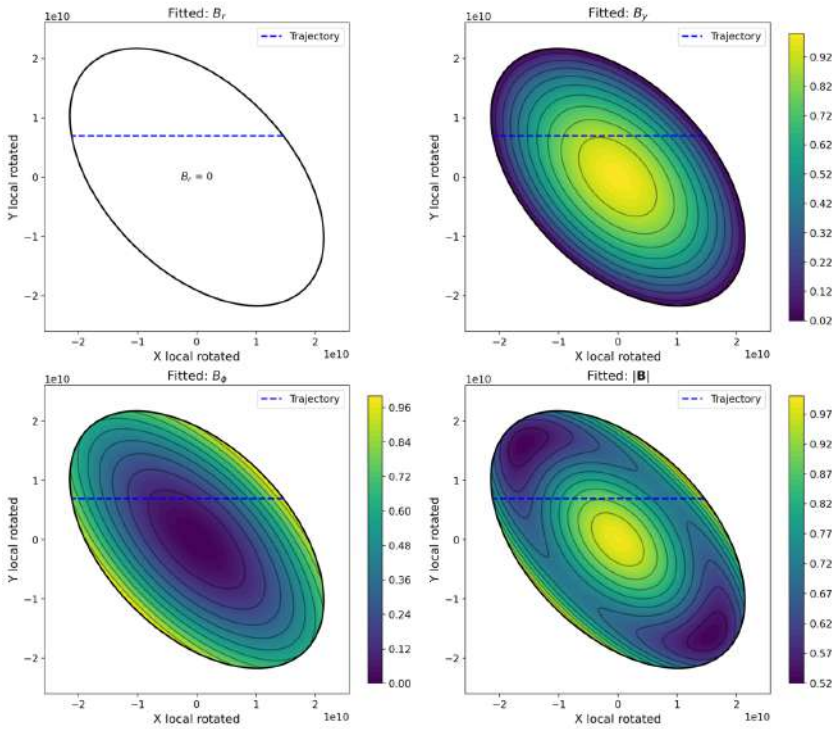

Figure 5.2: Magnetic field inside the cross section of the synthetic flux rope.

The satellite's trajectory through the flux rope was then simulated, and from this we extracted the magnetic field values that the satellite would detect, as shown in Figure 5.3.

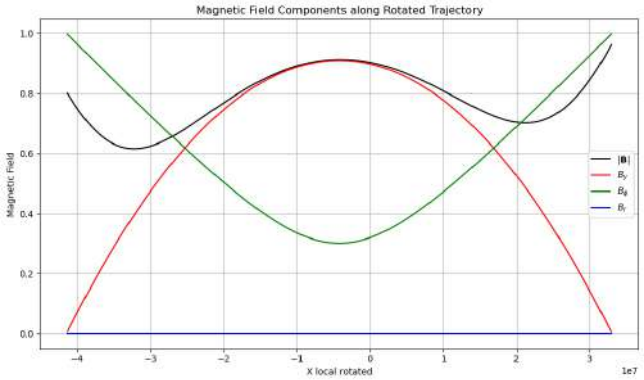

Figure 5.3: Magnetic field values evaluated at the trajectory points.

Note that the magnetic field components are expressed as contravariant components, and that the field magnitude was calculated using formula 3.4. Hence, the magnitude does not necessarily exceed all individual components, as one might expect in an orthonormal metric.

5.1.3 Transformation of Coordinates and Exporting the Data

With these data, we now have the satellite's observations in the cylindrical coordinate system. However, real experimental data are recorded in GSE coordinates. Therefore, we must apply the corresponding coordinate transformation to these generated values to obtain what the satellite would actually record. As explained in Section 4.4.2, we will apply relations 4.31 to convert the cylindrical magnetic field components into local Cartesian components, and then apply the inverse of relation 4.27 to obtain the components in the GSE frame.

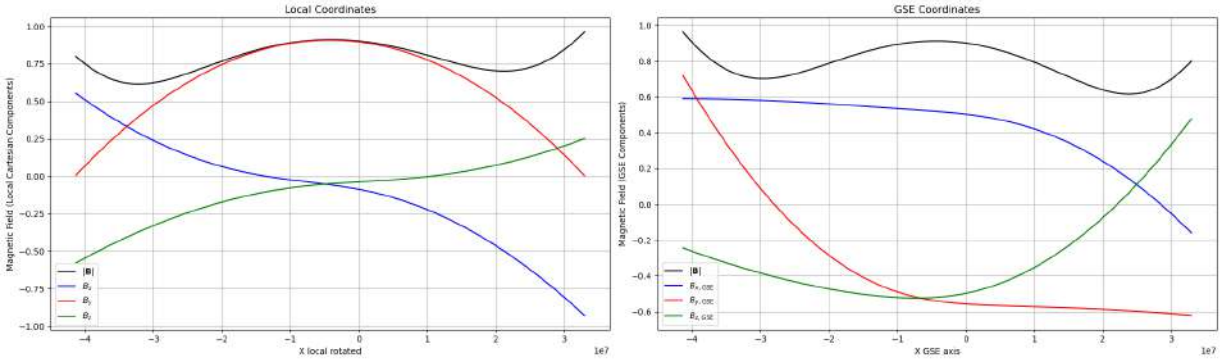

Figure 5.4: Magnetic field components in Local and GSE coordinate systems.

With this we would have generated the values the spacecraft would observe if it crossed the flux rope along the defined trajectory. However, for the study we will add irregularities to better simulate what would be detected in reality. We impose a certain Gaussian noise for each component, resulting in the following:

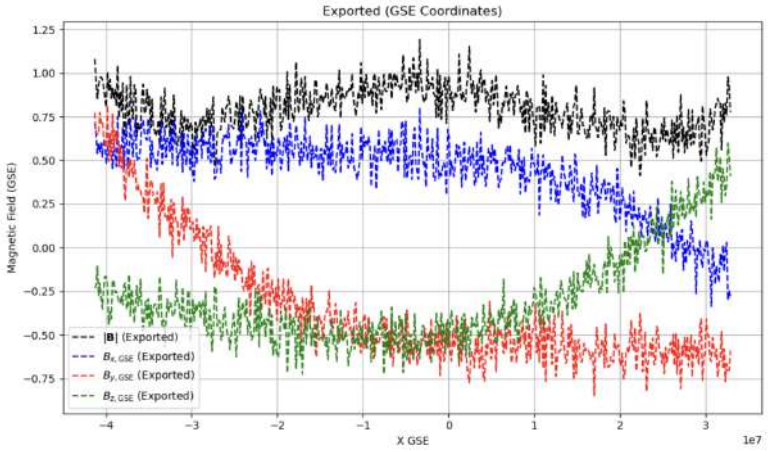

Figure 5.5: Synthetic GSE values with gaussian noise.

This is what we will export, and later analyze with X-CME. In the next section we show how the results converge when we apply our algorithm to these synthetic data.

5.1.4 Convergence Analisis

It will be crucial for our algorithm to check from what number of iterations the obtained result is sufficiently good. In X-CME, the user is allowed to choose the number of iterations to be taken for the fitting. For this first version, it has been assumed that each of the geometric variables has its domain discretized into n values. Thus, considering that we have 5 variables to iterate over, the total number of iterations will be calculated as 5th-order powers with base n. Therefore, for our convergence study, we consider for example the values:

n	3	4	5	6	7	8	9	11	13	15	20	22
N_{iter}	243	1 024	3 125	7 776	16 807	32 768	59 049	161 051	371 293	759 375	3 200 000	5 153 632

Table 5.1: Number of iterations N_{iter} for each n.

We will run the code for each of these values and see how good the resulting fit is. Below are some plots that will compare the evolution of the obtained values:

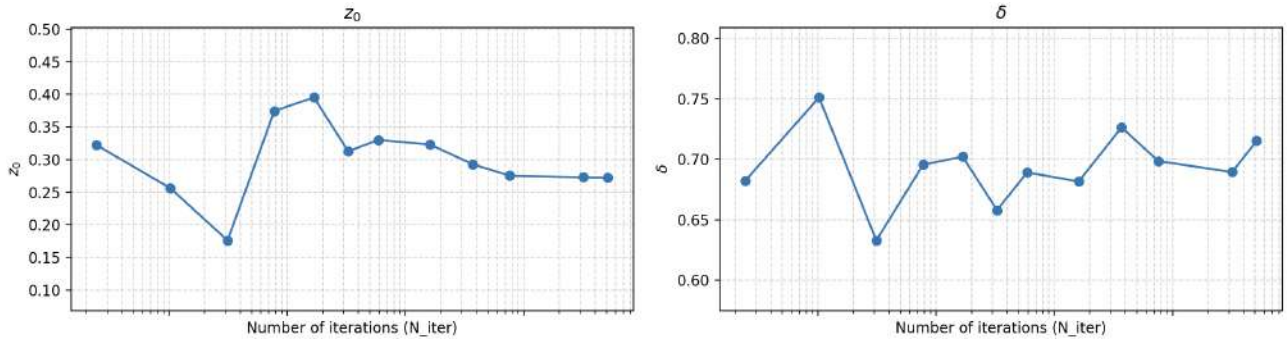

Figure 5.6: Convergence of the z_0 and δ parameters.

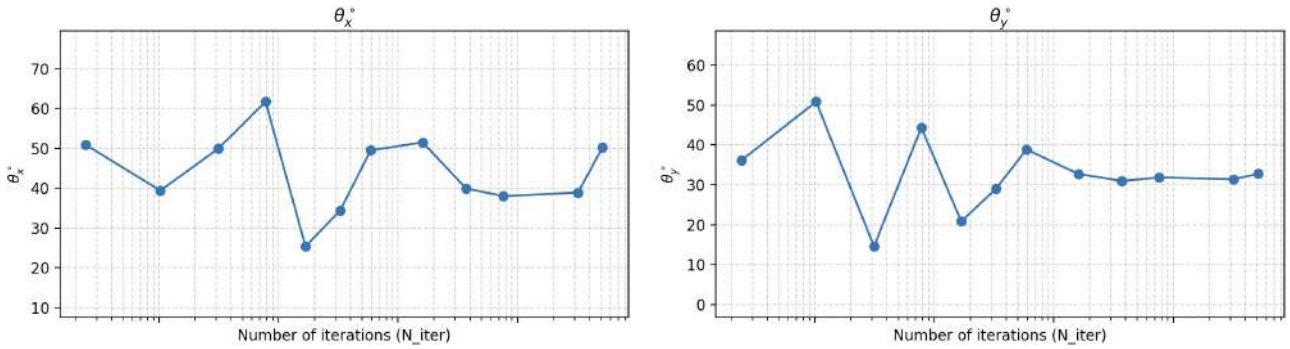

Figure 5.7: Convergence of the θ_x and θ_y parameters.

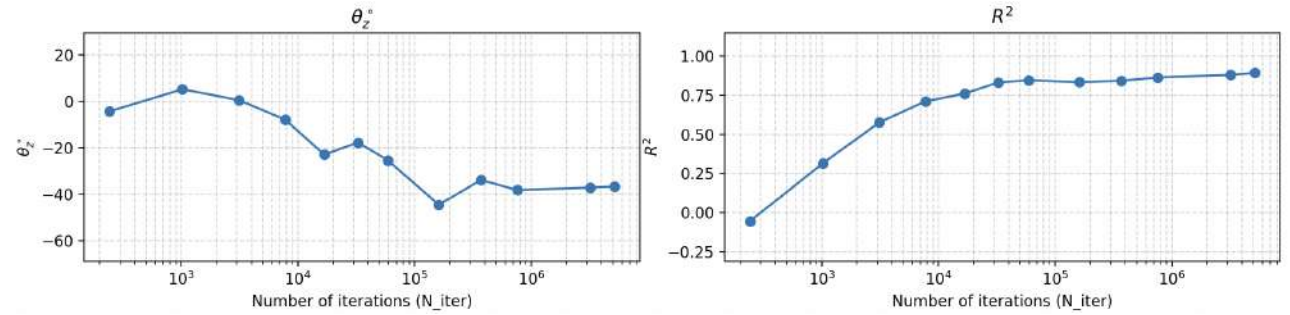

Figure 5.8: Convergence of θ_z and R^2.

From these plots, one can observe that the trend follows towards the original combination chosen for the synthetic Flux Rope. It is true that in the displayed values the original value is not reached perfectly, but this is also because the candidate parameters in each iteration are discretized values. Nonetheless, the results are good, and the trend of the coefficient of determination R^2 indicates that an increase in the number of iterations generally produces results better fitted to the original data.

In particular, if we run X-CME for the case of $n = 22$ ($N_{iter} = 5\,153\,632$), we obtain the following parameters:

Parameter	Obtained value	Original value
z_0	0.27246	0.30
δ	0.71516	0.70
θ_x	50.25262°	45.00°
θ_y	32.76500°	30.00°
θ_z	−36.59289°	−30.00°
R^2	0.89290	1

Table 5.2: Comparison of obtained values vs. original values

And the final result of the fit is seen as in Figure 5.9:

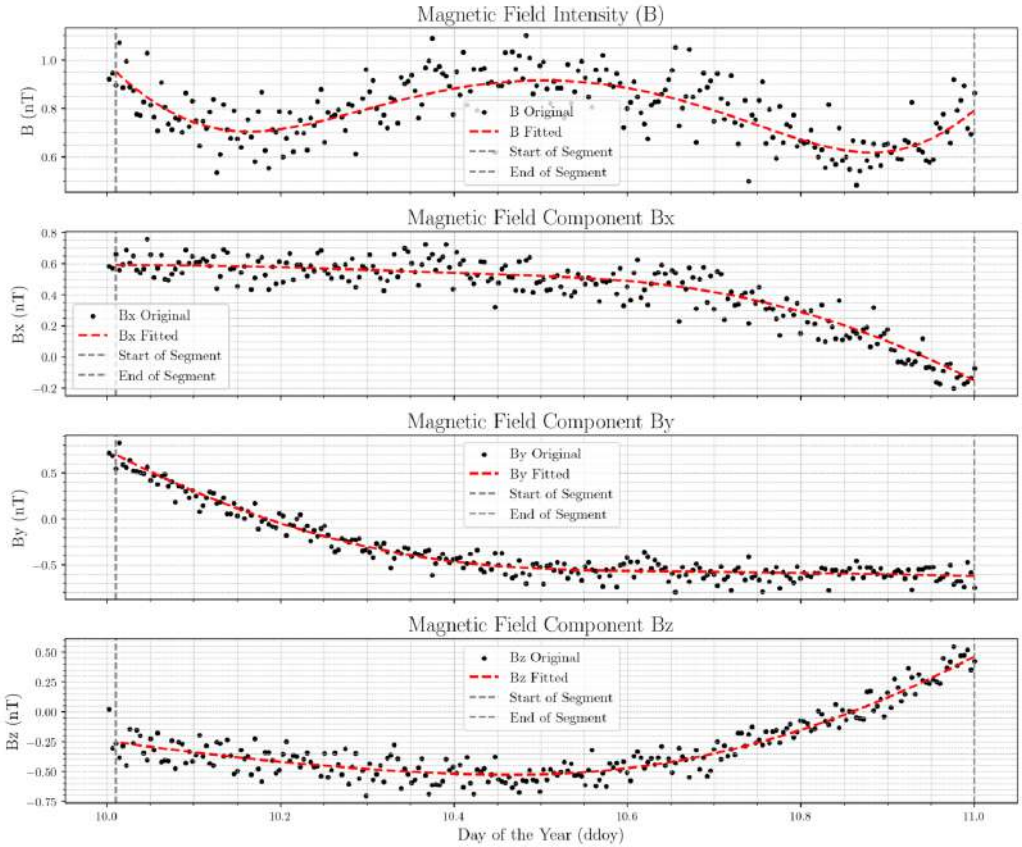

Figure 5.9: Fitted model to the generated in-situ data.

It can be seen that the fitted values are very similar to the originals. Considering the full domains of 4.4, to achieve a precision of $\pm 1°$ in the angles, it would be necessary to discretize their domain into steps of 2°. Therefore, one would have to make 180 partitions for the angles θ_x and θ_z, and 90 partitions for θ_y (since its domain spans 180°). To have a resolution of ± 0.1 in z_0, one would have to make 10 partitions, since its full domain is from -1 to $+1$ (although in practice the extremes are not included, and it is taken up to 0.8). Finally, for a resolution of ± 0.1 in the parameter δ, only 5 iterations would be needed, since it can take values from 0.1 to 1 (although in practice, the lower limit does not reach such distortion, but rather is usually taken from 0.4 to 1).

In conclusion, one can state that the relative tolerance for each variable may be expressed based on its domain and calculated as:

$$\boxed{\text{tolerance} = \pm \frac{\text{Domain}}{2n}} \tag{5.3}$$

where n is the number of partitions made within the variable's domain. Thus, the way to further minimize the tolerance for a given variable is to increase the number of iterations for those with a larger domain, and reduce it for those requiring less precision or possessing a smaller domain (as is the case for θ_x and θ_z in contrast to θ_y, as noted above).

5.2 Fitting of Real Events

The final step in validating our new flux-rope fitting algorithm is to compare X-CME results with published fits of well-studied events. We selected two events observed by the WIND spacecraft and analyzed by Nieves-Chinchilla et al. [17]. These occurred on:

- ◇ **WIND 2009 – September 30**: DOY 273.32–273.82
- ◇ **WIND 2010 – January 2**: DOY 2.00–3.37

In [17], the magnetic field components are expressed using auxiliary parameters τ, C_1, φ, θ, and Y_0/R (see 2.2.1). For consistency, we extract the full $B^r(r)$, $B^y(r)$, and $B^\varphi(r)$ profiles from those parameters and compare them to the profiles generated by X-CME.

5.2.1 Published Reconstruction Parameters

Date (DOY)	τ	α [10^{-22} A/m^3]	C_1	φ (°)	θ (°)	Y_0/R (%)	R (AU)
2009 Sep 30 (273)	1	3.72	1.46	302	22	16	0.042
	2	2.00	0.64	313	21	26	0.038
2010 Jan 01 (001)	1	0.40	0.82	72	22	8	0.105
	2	0.16	0.36	82	25	4	0.109

Table 5.3: Reconstruction parameters from Nieves-Chinchilla et al. [17]

Note that τ was held fixed to values 1 and 2 in the published fits to simplify convergence.

5.2.2 Analytical Forms of $B(r)$

From the reconstruction relations,

$$B^r(r) = 0, \qquad B^y(r) = B_y^0 - \mu_0 \alpha_1 \frac{r^2}{2}, \qquad B^\varphi(r) = -\mu_0 \beta_0 \frac{r}{2},$$

with

$$B_y^0 = \frac{\mu_0 \alpha_1 R^2 \tau}{2} \qquad C_{10} = \frac{\alpha_1}{\beta_0} R \qquad \beta_0 = \frac{\alpha_1 C_{10}}{R} \tag{5.4}$$

we obtain the magnetic field profiles shown in Table 5.4 (expressed in T):

Event Date	τ	$B^r(r)$	$B^y(r)$	$B^\varphi(r)$
2009 Sep 30	1	0	$9.227 \cdot 10^{-9} - 2.337 \cdot 10^{-28}\, r^2$	$-1.006 \cdot 10^{-18}\, r$
	2	0	$8.122 \cdot 10^{-9} - 1.257 \cdot 10^{-28}\, r^2$	$-1.116 \cdot 10^{-18}\, r$
2010 Jan 01	1	0	$6.201 \cdot 10^{-9} - 2.513 \cdot 10^{-29}\, r^2$	$-4.814 \cdot 10^{-19}\, r$
	2	0	$5.346 \cdot 10^{-9} - 1.005 \cdot 10^{-29}\, r^2$	$-4.554 \cdot 10^{-19}\, r$

Table 5.4: Magnetic-field components as functions of r for each event and τ.

We now proceed to evaluate and compare fits for each event.

5.2.3 Event 1: WIND 2009 – September 30

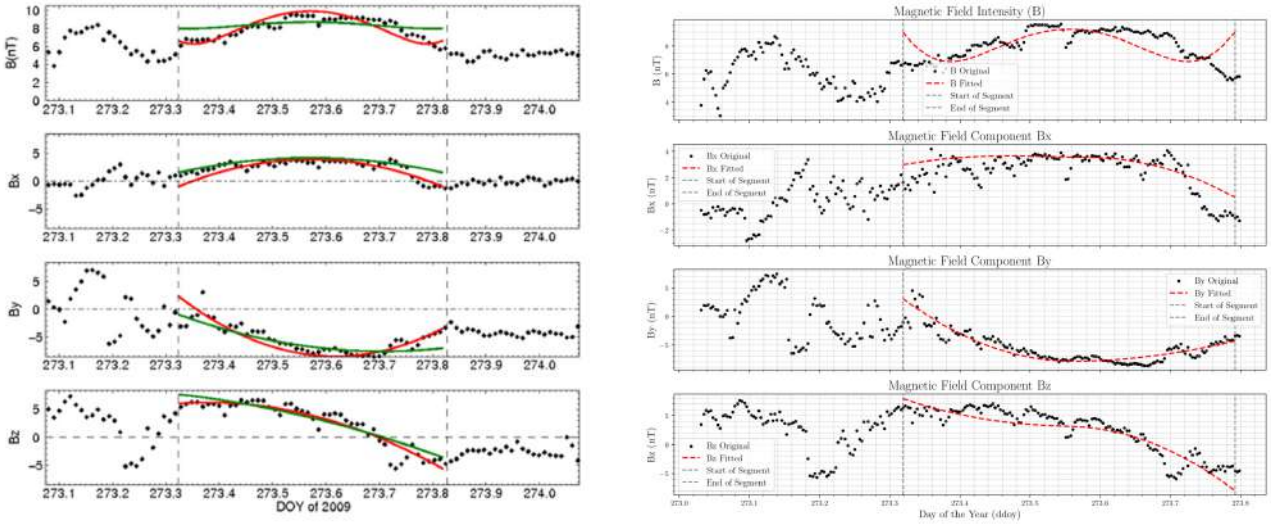

(a) Published fit [17] **(b)** X-CME fit

Figure 5.10: Comparison of published and X-CME flux-rope fits for 2009 Sep 30.

At first glance, the two fits are visually similar. Converting the published profiles to nT yields:

$\tau = 1$	$\tau = 2$
$B^r(r) = 0,$	$B^r(r) = 0,$
$B^y(r) = 9.227 - (2.337 \cdot 10^{-19})\, r^2,$	$B^y(r) = 8.122 - (1.257 \cdot 10^{-19})\, r^2,$
$B^\varphi(r) = -(1.006 \cdot 10^{-9})\, r$	$B^\varphi(r) = -(1.116 \cdot 10^{-9})\, r$

Table 5.5: Published magnetic-field components (nT) for 2009 Sep 30 WIND event.

On the other hand, X-CME yields the following magnetic field components:

$$B^r = 0, \qquad B^y(r) = 9.3646 - 1.6616 \cdot 10^{-19}\, r^2, \qquad B^\varphi(r) = -1.2343 \cdot 10^{-9}\, r.$$

One can observe how both methods produce very similar profiles in sign and shape. On the other hand, regarding the Flux Rope orientation and dimensions, we observe the following:

	$\tau = 1$	$\tau = 2$	X-CME
θ (XY)	22°	21°	–5.61°
φ (XZ)	302°	313°	348.54°
Y_0/R (%)	16	26	14
R (AU)	0.042	0.038	0.0471

Table 5.6: Geometric parameters: published vs. X-CME (2009 Sep 30 WIND event).

Discrepancies in orientation reach up to 43°, while the FR radius and the entrance height agree within a few percent. Such differences, nonetheless, were expected, given that:

1. The published fitting used the fixed values for τ
2. Both methods used different minimization schemes (global Levenberg–Marquardt vs. iterative)

Nonetheless, there is a close agreement across nearly all parameters, which is encouraging.

5.2.4 Event 2: WIND 2010 – January 1

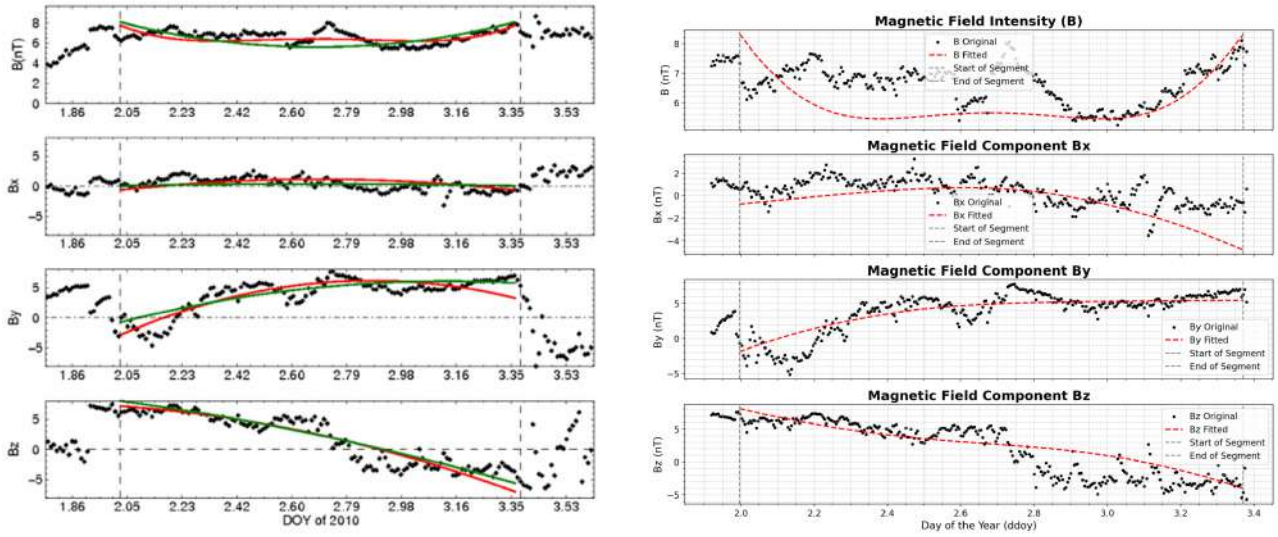

(a) Published fit [17] **(b)** X-CME fit

Figure 5.11: Comparison of published and X-CME flux-rope fits for 2010 Jan 1.

Converting the published profiles to nT yields:

$\tau = 1$	$\tau = 2$
$B^r(r) = 0,$	$B^r(r) = 0,$
$B^y(r) = 6.201 - (2.513 \cdot 10^{-20})\, r^2,$	$B^y(r) = 5.346 - (1.005 \cdot 10^{-20})\, r^2,$
$B^\varphi(r) = -(4.814 \cdot 10^{-10})\, r$	$B^\varphi(r) = -(4.554 \cdot 10^{-10})\, r$

Table 5.7: Published magnetic-field components (nT) for 2010 Jan 1 WIND event.

On the other hand, X-CME yields:

$$B^r = 0 \qquad B^y(r) = 6.470 - 1.467 \cdot 10^{-20}\, r^2 \qquad B^\varphi(r) = -4.3322 \cdot 10^{-10}\, r$$

And we observe how both methods produce very similar component shapes and signs. Additionally, the geometric parameters for this case compare as follows:

	$\tau = 1$	$\tau = 2$	X-CME
θ (XY)	22°	25°	22.04°
φ (XZ)	72°	82°	67.60°
Y_0/R (%)	8	4	45
R (AU)	0.105	0.109	0.127

Table 5.8: Geometric parameters: published vs. X-CME (2010 Jan 1 WIND event).

Here, the flux-rope orientation (θ, φ) agrees closely between methods. However, the relative entry height Y_0/R differs markedly (4–8% vs. 45%), driving a larger discrepancy in the fitted radius R of the flux rope (around a 10% difference).

5.2.5 Conclusions of the Real-Event Comparison

Across both events, X-CME successfully reproduces the published magnetic-field profiles and orientation parameters, with discrepancies primarily arising from:

- ◇ The fixed choice of τ in the published reconstructions.
- ◇ Different fit-quality metrics (Pearson's ρ vs. coefficient of determination R^2).
- ◇ Distinct minimization methods (global Levenberg–Marquardt vs. iterative grid search).

Despite these factors, a remarkable agreement is observed in the resulting flux-rope orientation (θ, φ) as well as its dimensions, indicating that both fitting algorithms can yield very similar results. The way to determine which of the two fits reality better would likely be to use them

as forecasts for the propagation of the magnetic structure. Without subsequent validation, it is impossible to know whether one model represents reality more accurately than the other.

In the following chapters, this type of analysis will be carried out, proposing an integrated flux-rope model within the CME structure. Since, to date, flux-rope fittings have not been applied to CME forecasting, the predictions will be validated directly against data provided by successive spacecraft observing the same event. By comparing the forecast made from the first detection with the measurements from the next spacecraft, we can assess whether both the flux-rope fitting algorithms and the global CME model are accurate.

6 . CME Propagation Dynamics

Once the structure and orientation of the Flux Rope have been defined, the next step will be to model the global structure of the CME based on it, and predict how the propagation will proceed after detection, as well as to deduce how the propagation occurred from when it left the Sun until it was detected by the satellite.

In order to solve this problem, it will be necessary to address the dynamics of the CME propagation, and to do so it will be necessary to consider some hypotheses.

6.0.1 Hypotheses for the CME Model

- ◇ The in-situ measured velocity component of the flux rope can be considered almost entirely radial (i.e., the CME propagates radially away from the Sun).
- ◇ The total mass of the CME is constant during the propagation.
- ◇ The CME is assumed to be globally electrically neutral.
- ◇ Geometry: the global structure of the CME is modeled as a tapered torus, with poloidal angle parameter ϕ spanning from $-\frac{\pi}{2}$ to $\frac{\pi}{2}$, as shown in the figure 6.3.
- ◇ The CME section is constant throughout its structure, and has the same shape as the Flux Rope section encountered.

6.1 Dynamics of the Propagation for the CME

As shown in [28], the primary contribution to the dynamics of a CME during its propagation is the drag due to the solar wind. However, this is true beyond 20 solar radii. Before that, the gravitational interaction with the Sun is also highly relevant. One might ask whether magnetic interaction influences this process. When the CME is still confined within the low corona, in fact, the main forces governing its motion are magnetic interactions. However, once it is ejected into interplanetary space, the global structure is considered electrically neutral, and in most models this force is not taken into account. Therefore, in our case we will solve the system considering only the gravitational interaction and the drag from the solar wind.

We are interested in solving the system for the entire propagation, from the moment the CME is ejected from the Sun until it is subsequently detected. Therefore, in our system, we will consider both the gravitational interaction and the drag from the solar wind:

$$m_{\text{CME}} \cdot a_{\text{CME}} = F_{\text{grav}} + F_{\text{drag}} \tag{6.1}$$

This can be rewritten as:

$$m\frac{d^2r}{dt^2} = -G\frac{Mm}{r^2} - \frac{1}{2}C_d\rho(r)A(r)(v - v_{\text{sw}}(r))|v - v_{\text{sw}}(r)| \tag{6.2}$$

To facilitate solving this differential equation, we express the acceleration in terms of the velocity and the radial distance. [11] By applying the chain rule, we can transform the second time derivative into a form that depends on the radial velocity, yielding a first-order differential equation suitable for numerical or analytical integration:

$$\frac{d^2r}{dt^2} = \frac{dv}{dt} = \frac{dv}{dr}\frac{dr}{dt} = v\frac{dv}{dr} \tag{6.3}$$

$$\boxed{v\frac{dv}{dr} = -\frac{GM_s}{r^2} - \frac{C_d\rho(r)A(r)}{2m}(v - v_{\text{sw}}(r))|v - v_{\text{sw}}(r)|} \tag{6.4}$$

This is the system required to determine the propagation velocity along the entire trajectory of the CME, from its ejection from the Sun until it is detected. Once we obtain this velocity profile, and knowing the position and date of the satellite at which the event was detected, we can determine the date when the CME originated at the Sun. However, before solving this, we need to define some components of the equation, which will be done in the following sections.

6.1.1 Solar Wind Velocity

The basic differential equation of Parker's isothermal model is derived from the conservation of mass and momentum [25], with its implicit solution given by:

$$\frac{v_{\text{sw}}^2}{c_s^2} - \ln\left(\frac{v_{\text{sw}}^2}{c_s^2}\right) = 4\ln\left(\frac{r}{r_c}\right) + 4\frac{r_c}{r} - 3 \tag{6.5}$$

where:

- $v_{\text{sw}} = v_{\text{sw}}(r)$: Solar wind speed as a function of distance r,
- $c_s = \sqrt{\frac{kT}{m}}$: Isothermal sound speed, where k is Boltzmann's constant, T is the coronal temperature, and m is the average particle mass (typically the proton mass m_p),
- $r_c = \frac{GM_s}{2c_s^2}$: Critical radius, the point where $v_{\text{sw}} = c_s$ (transition from subsonic to supersonic

flow), with G as the gravitational constant and M_s as the Sun's mass.

This equation is typically approximated by two distinct behaviors: one for distances closer to the Sun than the critical radius r_c, and another for distances beyond it [25]:

Asymptotic Behavior

- **Near the Sun ($r \ll r_c$):** The speed is subsonic and increases slowly. We can approximate:

$$v_{\text{sw}} \approx c_s \exp\left(2\ln\left(\frac{r}{r_c}\right) + 2\frac{r_c}{r} - \frac{3}{2}\right) \tag{6.6}$$

  This is an approximation valid for $v_{\text{sw}} \ll c_s$.

- **Far from the Sun ($r \gg r_c$):** The speed becomes supersonic and approaches a constant value:

$$v_{\text{sw}} \approx c_s\sqrt{4\ln\left(\frac{r}{r_c}\right) + 4\frac{r_c}{r} - 3} \tag{6.7}$$

  At large distances ($r \to \infty$), the logarithmic term dominates, but in practice, v_{sw} stabilizes at a terminal value (e.g., 400–500 km/s under typical conditions).

The resulting velocity profile can be observed by plotting these functions on a logarithmic scale:

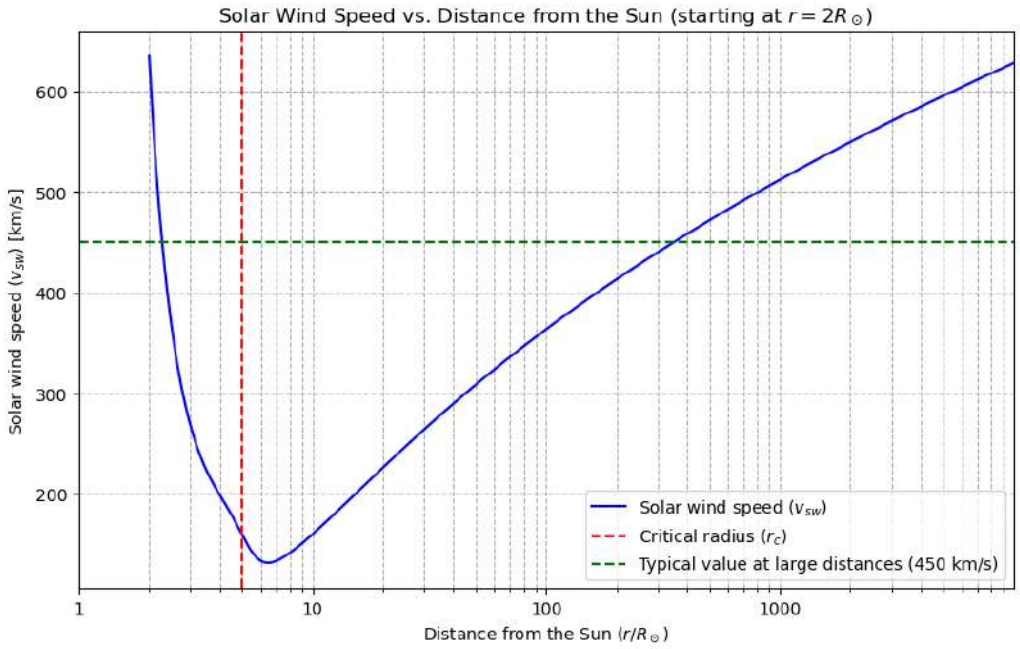

Figure 6.1: Solar wind speed (v_{sw}) profile from $2R_s$ to $10,000R_s$.

This will be the velocity that affects the drag component in equation 6.4.

6.1.2 Density Profile in the Interplanetary Medium

The next property necessary to perform this calculation is to determine the function that provides the mass density of the interplanetary medium as a function of the distance from the Sun.

The solar wind density $\rho(r)$ is calculated by considering the mass continuity equation for a radial spherical flow, as shown in [25]. It is assumed that the solar wind flow is steady, so the mass loss rate is constant across any spherical surface of radius r:

$$\rho(r) = \frac{\dot{M}}{4\pi r^2 v_{\mathrm{sw}}(r)} \tag{6.8}$$

Using the solar wind velocity profile found earlier, we can plot the density profile as a function of distance, as shown in the figure:

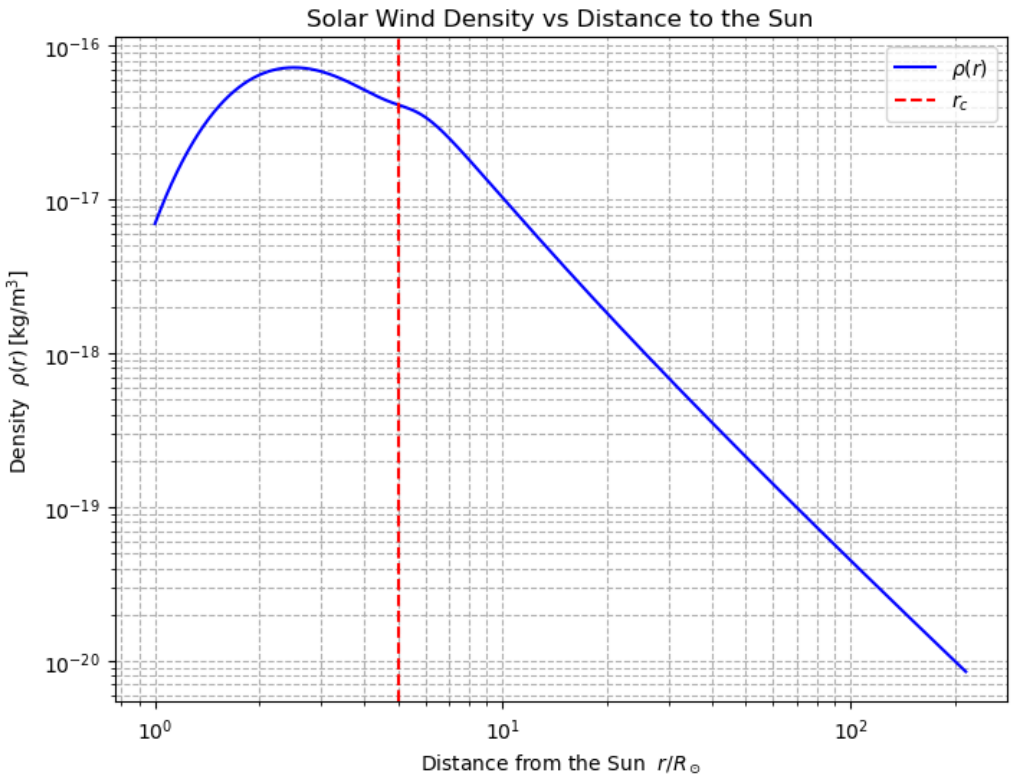

Figure 6.2: Solar wind density profile.

It should be noted that, although this is the current model used to estimate the solar wind density at distances greater than several solar radii, it still exhibits significant errors at distances close to the solar surface. Specifically, we observe that at 1 $R_\odot$, this model yields an approximate value of $7 \cdot 10^{-18}\,\mathrm{kg/m^3}$, whereas the value reported by [3] is on the order of $10^{-12}\,\mathrm{kg/m^3}$, indicating a discrepancy of several orders of magnitude. This difference arises because the simplified model does not fully capture the complexities of the lower corona, where the density is higher due to the magnetic structure and coronal heating processes.

Nonetheless, this inaccuracy in the density near the Sun has a negligible effect on the calculation of the CME propagation velocity at those distances. At distances close to the solar surface ($r < 10\,R_\odot$), not only the gravitational force gains importance, but also there are additional interactions due to the intense magnetic field produced in that area. The contribution of drag, which depends on $\rho(r)$, begins to become more significant at larger distances, specifically beyond $\sim 20-30\,R_\odot$, as observed in studies of CME propagation [28]. At distances greater than $50\,R_\odot$, the drag force becomes the primary factor determining the CME velocity, as the gravitational force diminishes significantly ($F_{\text{grav}} \propto 1/r^2$), while the drag depends on the density and the relative velocity between the CME and the solar wind.

6.1.3 Geometry of the CME

In the previous fits, we have determined the orientation of the Flux Rope and its internal field structure, assuming that there was no variation of the physical properties in the axial direction. If we want to use this result for the new tapered torus geometry under consideration, we must bear in mind that if we locate ourselves in regions where the cross-section varies very substantially, the assumption of no variation along the axial direction would cease to be valid, since the geometry would also change significantly.

To avoid this, we will impose that this approximation can only be made if the flux rope makes an angle not too large with the y-axis. For this study, an angular limit of 45° has been considered, but a more extensive validation would be required to determine which threshold would be most appropriate. Undoubtedly, this would be an interesting task for the future.

Thus, to fit the Flux Rope to this new geometry, we will use the fifth hypothesis considered at the beginning of this chapter, and we must determine what inclination the global structure must have and at which cross-section we must locate ourselves such that the central axis of the detected CME coincides with the normal vector of a cutting plane within the CME.

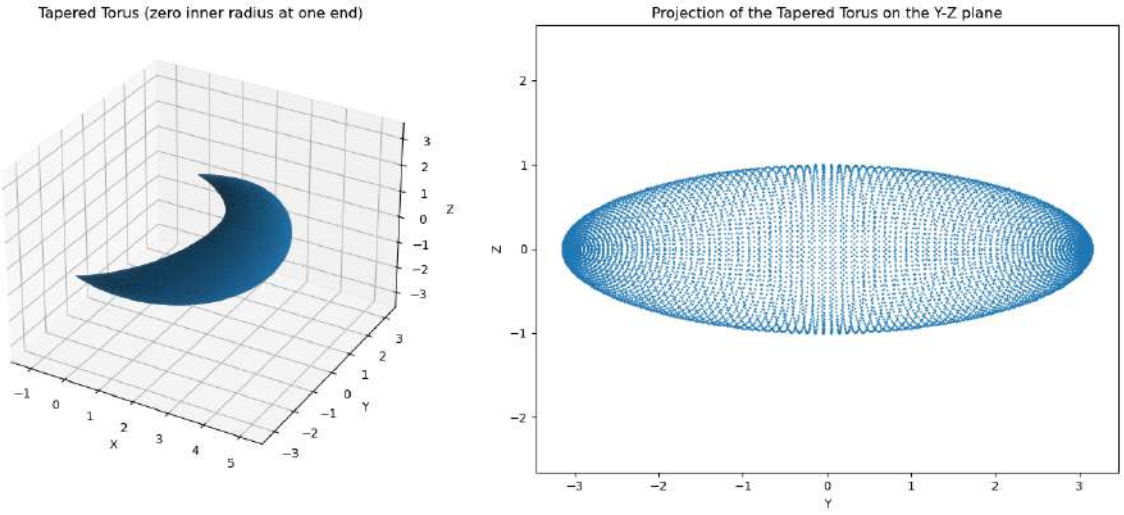

Figure 6.3: Tapered torus geometry and projection onto the Y-Z plane.

To begin, the mathematical definition of a torus with an elliptical cross-section is as follows:

$$\begin{cases} x = (R + a\cos\theta)\cos\phi, \\ y = (R + a\cos\theta)\sin\phi, \\ z = b\sin\theta, \end{cases}$$

where a and b are the semi-major and semi-minor axes of the ellipse, and they satisfy $b = \delta\, a$.

The tapering is achieved by making the cross-section shrink as a function of the major angle ϕ. We do this by applying a factor $\cos\phi$ that multiplies a. The effect of this factor can be seen in the following illustration:

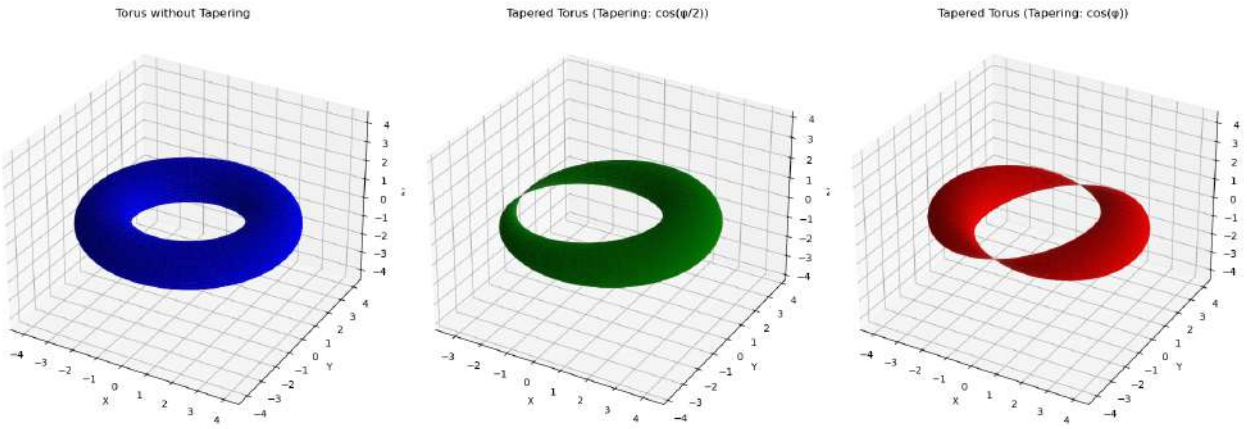

Figure 6.4: Applying different tapering factors to the torus.

For this model, we will choose a factor of $\cos\phi$ and take only the domain $\phi \in (-\pi/2, \pi/2)$, thus recovering the shape shown in Figure 6.3. The resulting equations are:

$$\begin{cases} x = (R + a_{\max}\cos\phi\cos\theta)\cos\phi, & \phi \in [0, 2\pi], \\ y = (R + a_{\max}\cos\phi\cos\theta)\sin\phi, & \theta \in [-\pi/2, \pi/2], \\ z = \delta\, a_{\max}\cos\phi\sin\theta & \delta \in (0, 1]. \end{cases} \tag{6.9}$$

6.1.4 Rotation, Cut Section, and Projected Area of the Torus

Rotation of the Torus

The next step is to allow the torus to rotate about the x-axis, thereby changing its orientation. The purpose of this rotation is as follows: if we take an arbitrary cross-section of the torus, we observe that its normal vector is always contained in the x-y plane. However, when we determine the orientation of the flux rope, we impose no restrictions on the direction in which its internal axis points. Therefore, to align it with the internal cross-section of the torus, we

must allow that cross-section to be oriented arbitrarily.

The components rotated about the x-axis take the form:

$$\begin{cases} x_{\text{rot}} = x = (R + a_{\max}\cos\phi\cos\theta)\cos\phi \\ y_{\text{rot}} = y\cos\theta_x - z\sin\theta_x = (R + a_{\max}\cos\phi\cos\theta)\sin\phi\cos\theta_x - \delta\, a_{\max}\cos\phi\sin\theta\sin\theta_x \\ z_{\text{rot}} = y\sin\theta_x + z\cos\theta_x = (R + a_{\max}\cos\phi\cos\theta)\sin\phi\sin\theta_x + \delta\, a_{\max}\cos\phi\sin\theta\cos\theta_x \end{cases}$$

Projection onto the Y–Z Plane

The following step involves projecting the torus surface onto the YZ plane, taking the coordinates $(y_{\text{rot}}, z_{\text{rot}})$ of all points obtained on the torus after rotation. This projection creates a cloud of points on that plane. We then extract only the outermost point in each direction to define the projected contour.

1. **Find Extremal Points**: We establish our reference point at the center of the projected surface while defining a vector in polar coordinates. For each angle $\alpha \in (0, 2\pi)$, the direction vector defined as:
$$\mathbf{d}(\alpha) = (\cos\alpha, \sin\alpha)$$
will point to one direction and we will maximize the dot product $\big(y_{\text{rot}}, z_{\text{rot}}\big)\cdot\mathbf{d}(\alpha)$, finding the extremal points to trace the contour.
2. **Ellipse Fitting**: It is observed that this contour follows the shape of an ellipse. One could extract its expression using 5 points from it to define its semi-axes a, b, the coordinates of its center, y_c, z_c, and its rotation angle θ_{el}. However, there is an alternative way even more practical, which is using the `EllipseModel` function from `skimage`, which takes all the contour points and automatically fits an ellipse, providing its corresponding characteristic parameters.
3. **Compute the Projected Area**: Finally, once the semi-axis of the ellipse are computed, one can find the resulting projected area simply applying:
$$A \;=\; \pi\, a_{\text{contour}}\, b_{\text{contour}} \;=\; \pi\,\delta\, a_{\text{contour}}\,.$$

The process followed is shown graphically below. In the left figure, we have the tapered torus rotated by a certain angle, showing an internal cross-section at an angle of $\varphi = -35.3°$. The normal vector to this surface is also shown, which we always consider to have a positive x-component. Then, the figure on the right shows the projected points of the CME on the YZ plane and the fitted ellipse in its contour.

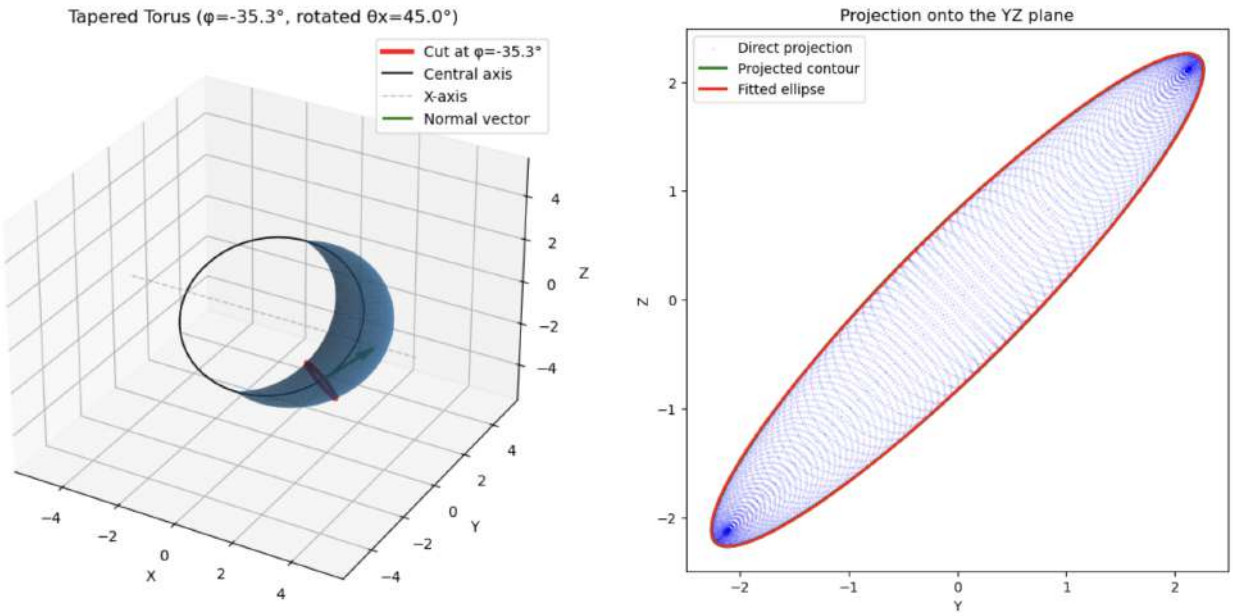

Figure 6.5: Cut section at a certain angle of the CME and projected area.

6.2 Expansion of the Geometry While Propagating

With the previous reasoning, we can determine the projected area of the CME at the moment it is observed. However, for the equation of motion, we need to know how this area changes throughout its entire trajectory, i.e., as a function of r. To do this, we will assume that the projected surface always maintains the same proportions and that its growth follows the form of an attenuated exponential:

$$a(r) = a_0 \left(\frac{r}{r_0}\right)^{\alpha} \qquad A(r) = \pi\delta a(r)^2 = \pi\delta a_0^2 \left(\frac{r}{r_0}\right)^{2\alpha} \tag{6.10}$$

Since there is no way to determine the initial size of the CME, we will consider a standard initial value of $a_0 \approx 3000\,\text{km}$ at a distance of 2 solar radii, and we will seek the growth factor α, using the experimental values of b_1 known at r_1 and b_0 known at r_0:

$$\alpha = \frac{\ln(b_1/b_0)}{\ln(r_1/r_0)} \tag{6.11}$$

6.3 Total Volume and Mass Inside the CME

In order to find the total volume, we will sweep an elliptical cross-section along $\phi \in (-\pi/2, \pi/2)$. The area of a cross-section is

$$A(\phi) = \pi\, a\, b\, \cos^2\phi,$$

and we will integrate it along the central path, with differential length $R\,d\phi$, obtaining:

$$V = \frac{\pi^2 Rab}{2} = \frac{\pi^2 R\delta a^2}{2}. \tag{6.12}$$

Which corresponds to the volume of the CME at the moment we observe it. Then, we will compute the average density of the CME found in-situ, and we will be able to compute the total mass as follows:

$$m_{\text{CME}} = \langle \rho \rangle \, V_{\text{CME}}$$

We will consider that this mass remains constant along the propagation, allowing us to consider it constant in the equation 6.4.

6.4 Time of propagation of the CME

With all the above, we can now solve equation 6.4, thus obtaining the velocity of the CME throughout its propagation through the interplanetary medium. By numerically solving the ODE, the following result is obtained:

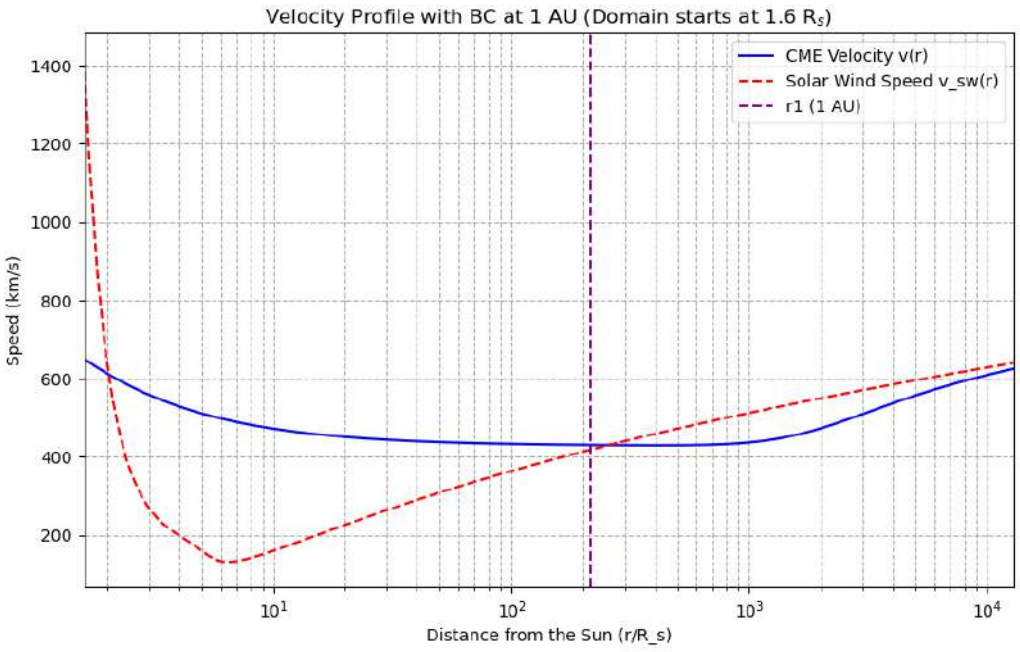

Figure 6.6: Propagation velocity of the CME and solar wind velocity.

This result agrees with experimental values of CME velocities at the moment they are ejected from the Sun, with values ranging between 500 km/s and 1000 km/s.[22, 27].

Thus, once the velocity profile along the trajectory of the CME is known, we can integrate it to find the time it took for the CME to travel from its ejection at the Sun to the observed

point, allowing us to determine the date on which the CME originated and verify whether the predictions of the emission are accurate.

The travel time t from the initial position r_0 to the observed position r_1 is calculated by integrating the inverse of the velocity profile $v(r)$:

$$t = \int_{r_0}^{r_1} \frac{dr}{v(r)}. \tag{6.13}$$

This integral is typically computed numerically using the velocity profile $v(r)$ obtained from solving equation 6.4. The result gives the time in seconds, which can then be converted to days for practical interpretation:

$$t_{\text{days}} = \frac{t_{\text{seconds}}}{86400},$$

where 86400 is the number of seconds in a day. This allows us to determine the exact date of the CME's ejection based on the detection date and the calculated travel time.

It is important to note that, once the ODE for the CME propagation velocity has been solved, we can integrate over any interval, past or future, to determine the time it takes for the CME to travel between any two locations.

6.5 Swept Area in the Ecliptic Plane

The next step in the study of CME propagation may be the most important for practical purposes. Determining the portion of a CME that lies within the ecliptic plane is crucial for assessing potential impacts on planetary bodies or other satellites. In this section, we first identify the intersection of the CME with the $z = 0$ plane, and then compute the evolving area that the CME sweeps out as it propagates.

6.5.1 Intersection with the Ecliptic Plane

To find the portion of the CME contained in the XY plane, the easiest way will be to make a horizontal cut through the projected area from at $z = 0$, as shown in Figure 6.7b.

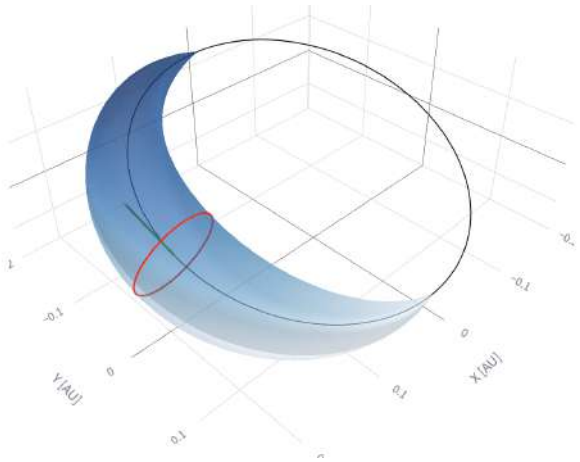

(a) Three-dimensional CME model

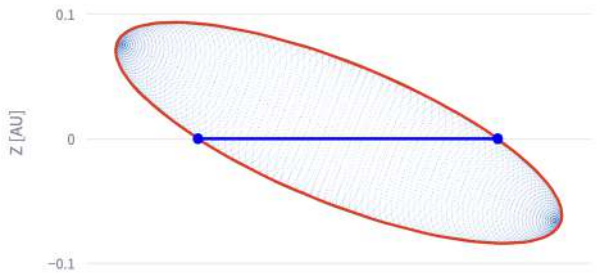

(b) Horizontal intersection at the ecliptic plane ($z = 0$)

Figure 6.7: CME geometry for the 2009-09-30 WIND event.

This will give us the instantaneous width of the CME within the ecliptic plane at the moment where the spacecraft is crossing it. Then, as we also know the CME's radial velocity and expansion rate, we can trace back how the area swept in the ecliptic plane grows over time:

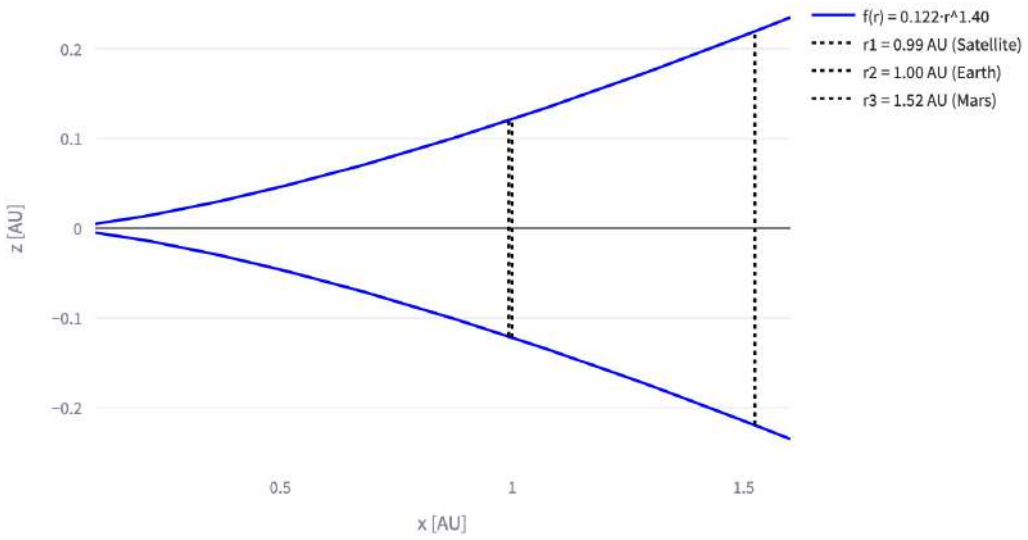

Figure 6.8: Temporal evolution of the area swept by the CME in the ecliptic plane.

However, we also need to know the propagation orientation, since the satellite may not have detected it at its center.

To determine the portion of the CME cut located to the right or left of the satellite, one simply checks which part of the cut lies on the positive or negative y-semi-axis in figure 6.7b. Once these portions are identified, and knowing the distance of that detection from the Sun, we can calculate the correction angle required to locate the corresponding ecliptic longitude at the center of the cut.

Let L_{cut} be the total length of the cut. The correction angle to be applied will be:

$$\varphi_{\text{correction}} = \arcsin\left(\frac{\Delta L_{\text{cut}}}{2\,r_1}\right) \tag{6.14}$$

where ΔL_{cut} is the difference in cut length between the right and left sides. With this, we can determine the true propagation direction of the central part of the cut in the ecliptic plane.

On the other hand, to see what angular width the CME will have once it reaches certain positions, we evaluate the expansion function at those points of interest and compute the angular amplitudes as follows:

$$\gamma_2 = \pm \arctan\left(\frac{f(r_2)}{r_2}\right) \quad \text{and} \quad \gamma_3 = \pm \arctan\left(\frac{f(r_3)}{r_3}\right) \tag{6.15}$$

Finally, the schematic of the CME's propagation path will be displayed on-screen, taking into account the positions of the satellite and the planets for the date on which the CME passes each location.

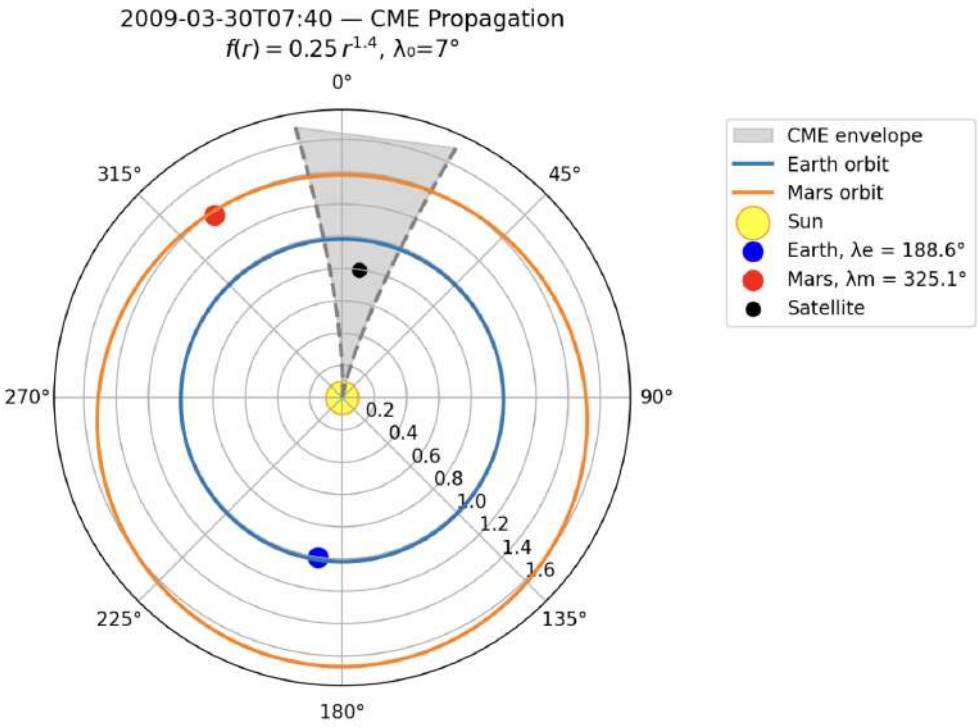

Figure 6.9: CME plot in the Solar System

Additionally, an animation of the CME propagation will be shown. An example can be found here: CME Propagation Video[1].

[1] `https://www.youtube.com/watch?v=FYmorZpCAoA`

7 . Validation of the CME Propagation Model

Finally, we will proceed to validate whether the predictions regarding the propagation of the CME are accurate or not. To do this, two events involving satellites that detected a CME at intermediate distances between the Earth and the Sun will be studied and, subsequently, it will be verified when those CMEs were later detected at Earth by WIND. The results will be analyzed using both the **radial model** (Model 1, 3.47) and the **radial–poloidal polynomical model** (Model 2, 3.38) already presented in this work.

7.1 Event 1: Parker Solar Probe - August 18, 2022

The first study event will be the one detected by Parker Solar Probe on August 18, 2022, with the internal magnetic structure spanning ddoy $\in$ (230.64, 231.01).

We proceed with an analysis analogous to that described in Section 6.1.4.

7.1.1 Fitting Results for the Flux Rope

The results of the internal magnetic structure fitting are the ones shown in Figures 7.1 and 7.2.

At first glance, it is observed that the versatility of the Radial–Poloidal model better adapts the fitting to the experimental data found, and this is reflected in the value of the coefficient of determination obtained. Table 7.1 summarizes the fitted parameters of the Flux Rope found in each case.

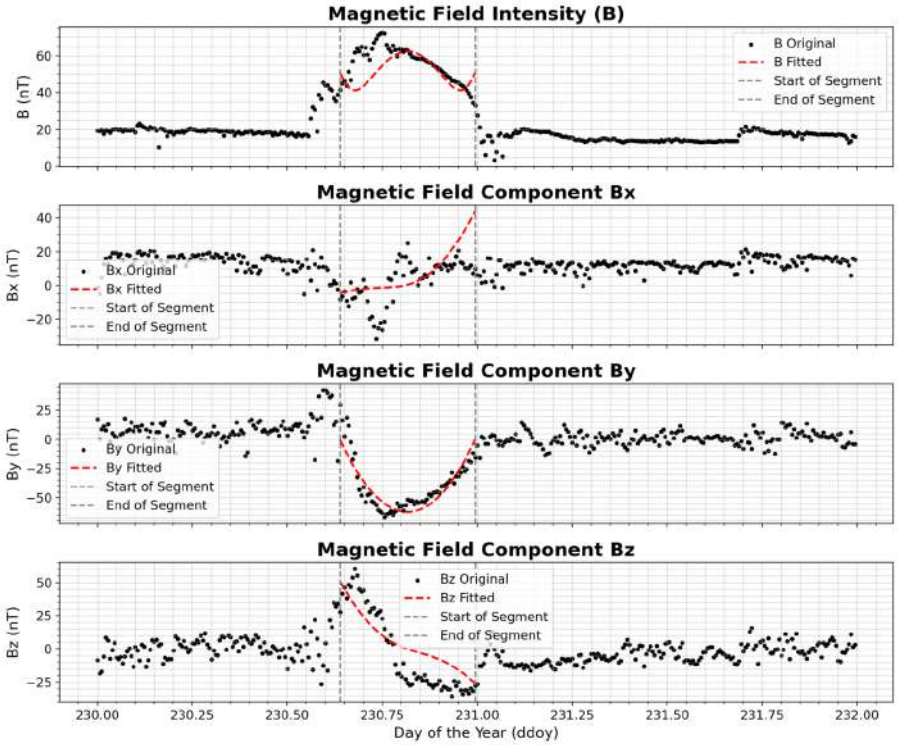

Figure 7.1: Fitting using the radial model, PSP – August 18, 2022

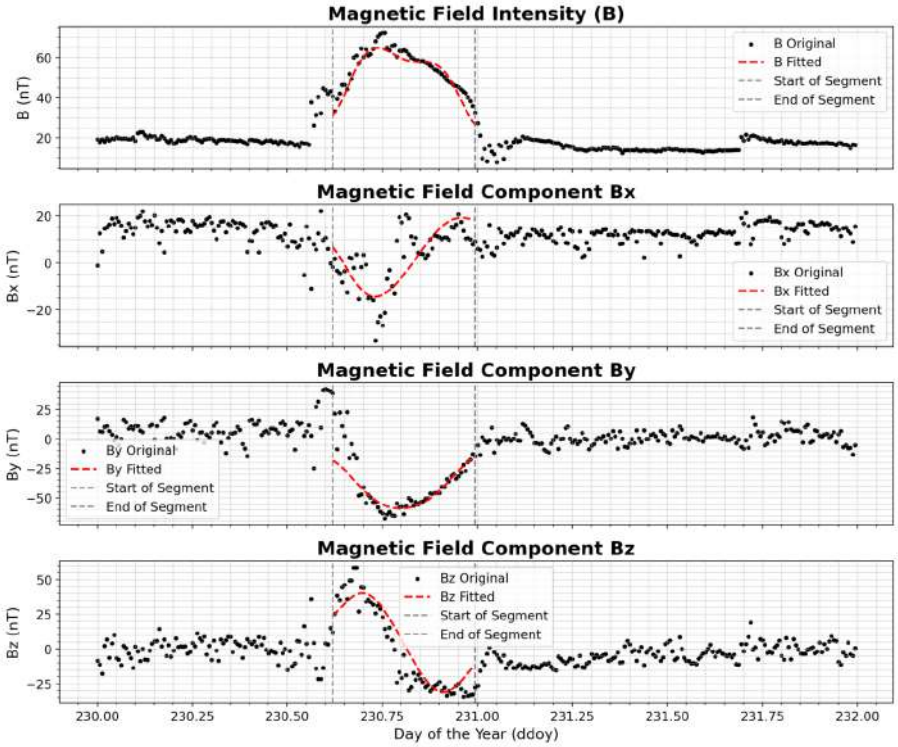

Figure 7.2: Fitting using the radial-poloidal model, PSP – August 18, 2022

From table 7.1, we can see that the coefficient of determination for the radial–poloidal model is considerably higher than for the purely radial model, which would indicate a higher fitting quality.

Parameter	Radial Model	Radial–Poloidal Model
z_0	-0.45	-0.50
θ_x	$-95.26°$	$133.67°$
θ_y	$7.66°$	$60.19°$
θ_z	$-22.73°$	$174.27°$
δ	1.00	0.87
θ (XY)	$-5.22°$	$-20.07°$
ϕ (XZ)	$67.39°$	$41.29°$
a (major axis) [AU]	0.0756	0.0716
b (minor axis) [AU]	0.0756	0.0624
R^2	0.3042	0.6634

Table 7.1: Comparison of the fitted parameters for the radial and radial–poloidal models.

On the other hand, although the iterative parameters may be very different, the resulting physical parameters used to describe the orientation and dimensions of the Flux Rope (θ_{XY}, ϕ_{XZ}, a, and b), are considerably similar in both cases, even when using different models, demonstrating that the final geometric description of the structure is essentially the same.

7.1.2 CME Propagation Results

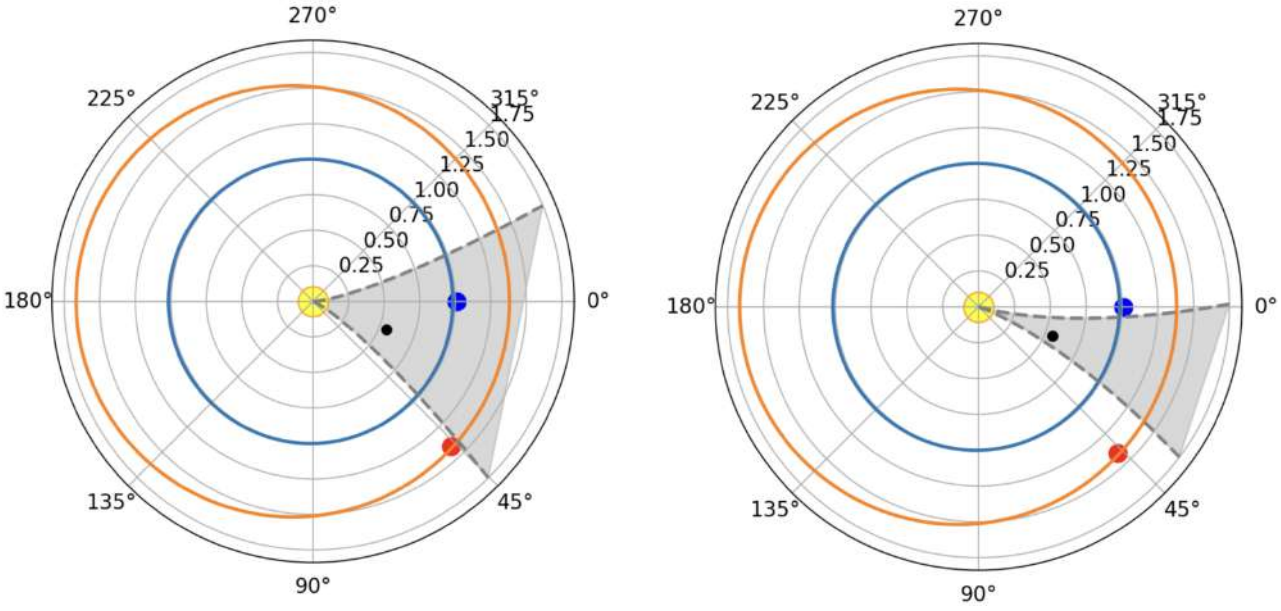

(a) CME Forecast Using Model 1. **(b)** CME Forecast Using Model 2.

Figure 7.3: Comparison of the CME forecast for each of the models studied.

Observing the CME propagation forecast, we see that the small differences resulting from the fits now have significant consequences. For Model 1, the CME is predicted to graze Earth on one flank and pass very close to Mars, whereas Model 2 predicts that its width will be insufficient for such an interaction and that it will, in principle, pass between the two bodies.[1]

Table 7.2 provides further details on the predicted propagation according to both models.

Key Timestamps	**Model 1**	**Model 2**
Departure From the Sun	2022-08-17 T09:34	2022-08-17 T09:04
Detected by Satellite	2022-08-18 T15:21	2022-08-18 T15:21
Crosses Earth's Orbit	2022-08-19 T18:05	2022-08-19 T17:50
Crosses Mars' Orbit	2022-08-21 T03:20	2022-08-21 T02:20
Satellite and Planetary Positions at their respective Timestamps		
Satellite	$r_1 = 0.554\,\text{AU}$, $\gamma_1 = 21.25°$	$r_1 = 0.554\,\text{AU}$, $\gamma_1 = 21.25°$
Earth	$r_2 = 1.012\,\text{AU}$, $\gamma_2 = 0.00°$	$r_2 = 1.012\,\text{AU}$, $\gamma_2 = 0.00°$
Mars	$r_3 = 1.407\,\text{AU}$, $\gamma_3 = 46.46°$	$r_3 = 1.407\,\text{AU}$, $\gamma_3 = 46.44°$
CME Propagation Details		
Ecliptic Longitude at the Center	11.30°	18.10°
CME Inclination	−5.62°	−27.48°
Angular Width at Earth Distance	(340.70°, 41.91°)	(4.13°, 32.07°)
Angular Width at Mars Distance	(338.22°, 44.39°)	(0.69°, 35.52°)
Encounter with Earth	Yes	No
Encounter with Mars	No	No

Table 7.2: Comparison of the CME forecast for the Parker Solar Probe event from August 18th, 2022.

We observe that in each case, the timestamp predictions are considerably similar, indicating that the CME is expected to reach each location at practically the same time for both models considered. However, it is observed that the predicted angular widths in each case are considerably different. This is because, although the global dimensions of the modeled CME are similar in both cases, in the first model a significantly larger portion is contained within the ecliptic plane, due to its lower inclination, as shown in Figure 7.4:

[1] It is relevant to mention here that, by convention, ecliptic longitudes are expressed in the HEE (Heliocentric Earth Ecliptic) coordinate system, which is why Earth always appears centered at angle 0°.

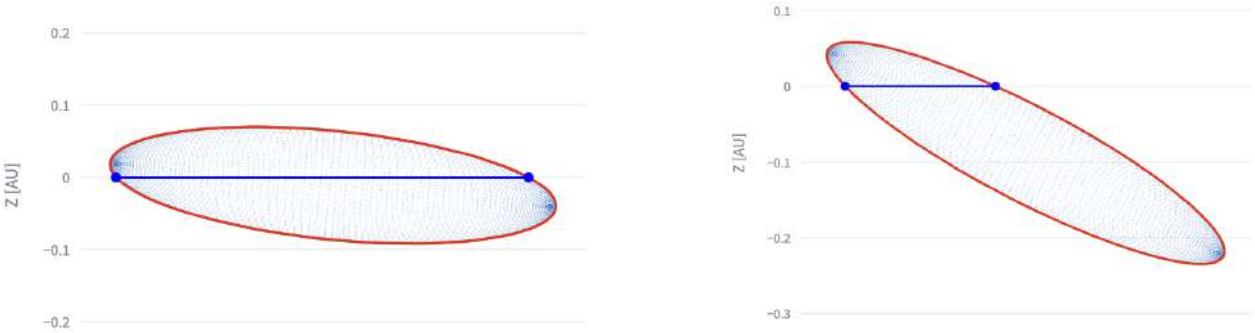

(a) CME Projected Area for Model 1.

(b) CME Projected Area for Model 2.

Figure 7.4: Projected area of the CME for the two models under study for the PSP event on August 18, 2022.

Next, we will use data to verify how accurate this prediction is. The typical way to corroborate whether a CME has reached Earth is by using in-situ data from the WIND satellite, which is located at the $L1$ point, and all events passing through it are considered to subsequently reach Earth.

7.1.3 Validation of CME Forecast with *WIND* In-Situ Observations

Figure 7.5 displays *WIND* data around the predicted CME arrival time. A clear disturbance in the magnetic field occurs near 18:00UT on August 19, 2022, corresponding to a forward shock, followed by a more regular region with features indicative of a more defined internal structure.

Regarding the collision timestamps, the time of the shock coincided with the predicted moment when the magnetic structure would reach Earth's orbit. However, each model forecast this encounter differently:

Collision Prediction for Each Model

- ◇ **Model 1**: Forecasts a flank encounter with an initial shock (sheath region) followed by traversal of the flux rope proper.
- ◇ **Model 2**: Predicts only a sheath passage without direct flux-rope traversal.

To determine which prediction is closer to reality, we analyze the in-situ data obtained.

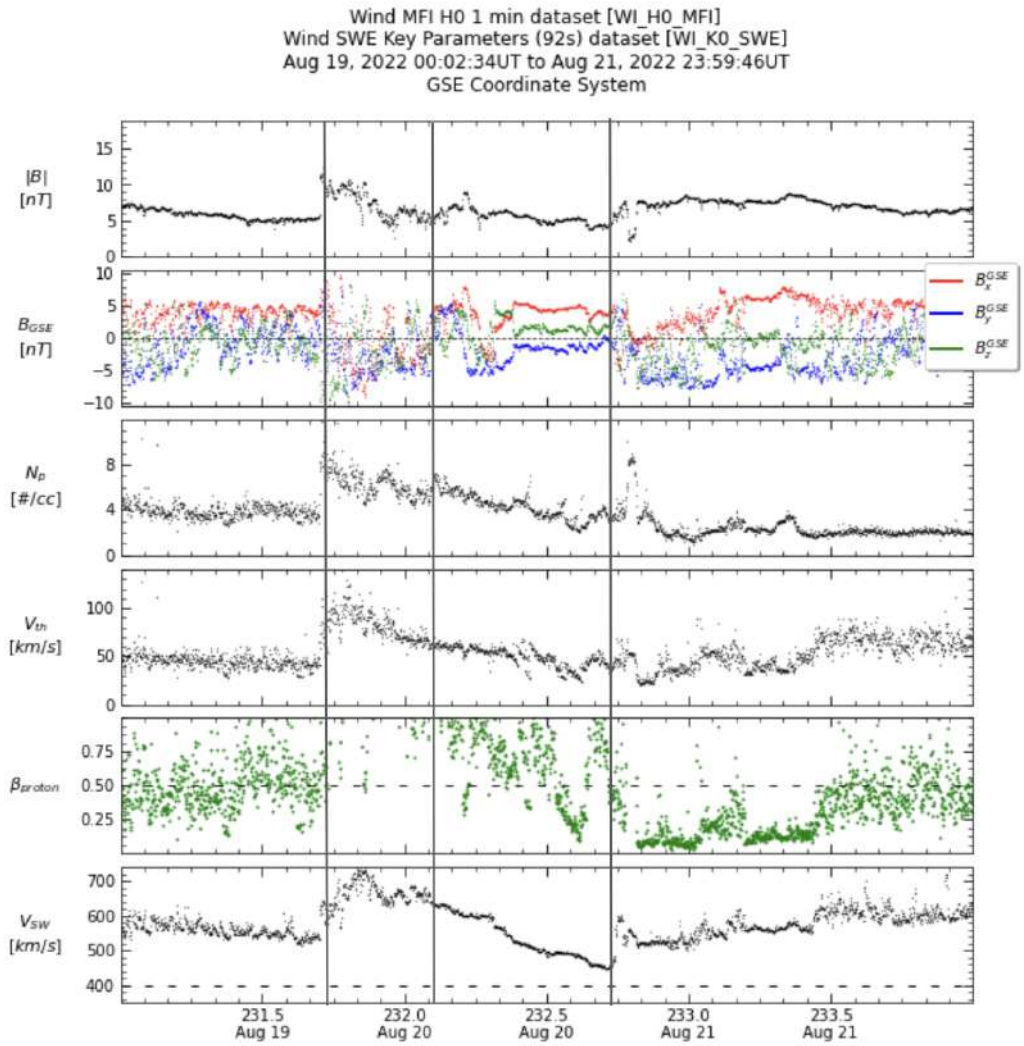

Figure 7.5: Magnetic and plasma parameters recorded by *WIND* on August 19, 2022, retrieved from the LASSOS catalog [13].

When passing through a CME flank, one typically observes a decrease in solar wind speed, a slight expansion of the magnetic field, and in some cases a shock. The CME's expansion is very weak and mainly manifests as a drop in V_{sw}. Compared to frontal shocks, the thermal temperature does not decrease as sharply during flank passages, nor do the proton density and the β_p parameter.

Since these conditions are visible in the in-situ plots, we conclude that the event indeed corresponds to a passage through one of the flanks, also referred to as a *Glancing Blow*.

It is worth noting that this type of event could also correspond to an encounter with the CME's envelope (the outer structure shown in Figure 1.4), and the resulting signatures would be very similar to those from a flank collision.

Forecast Accuracy.

Because our model does not yet include a dedicated sheath-forecast module, it remains difficult to estimate the sheath's expected thickness or to assess whether, in the second scenario, that

structure alone might collide with Earth.

Despite these uncertainties, both models predicted the CME's arrival at Earth with remarkable precision, within approximately one hour of the observed shock time (roughly 26 hours after the upstream detection). This outcome is a strong positive indication of the X-CME propagation framework's potential for operational forecasting.

7.2 Event 2: Solar Orbiter - March 8th, 2022

The second event we will study was detected on March 8, 2022, by the Solar Orbiter probe. The internal magnetic structure was determined to be within the interval $ddoy \in (67.92, 68.27)$. We proceed with an analysis analogous to the previous case:

For this case, the magnetic field fitting results are the ones shown in figures 7.6 and 7.7:

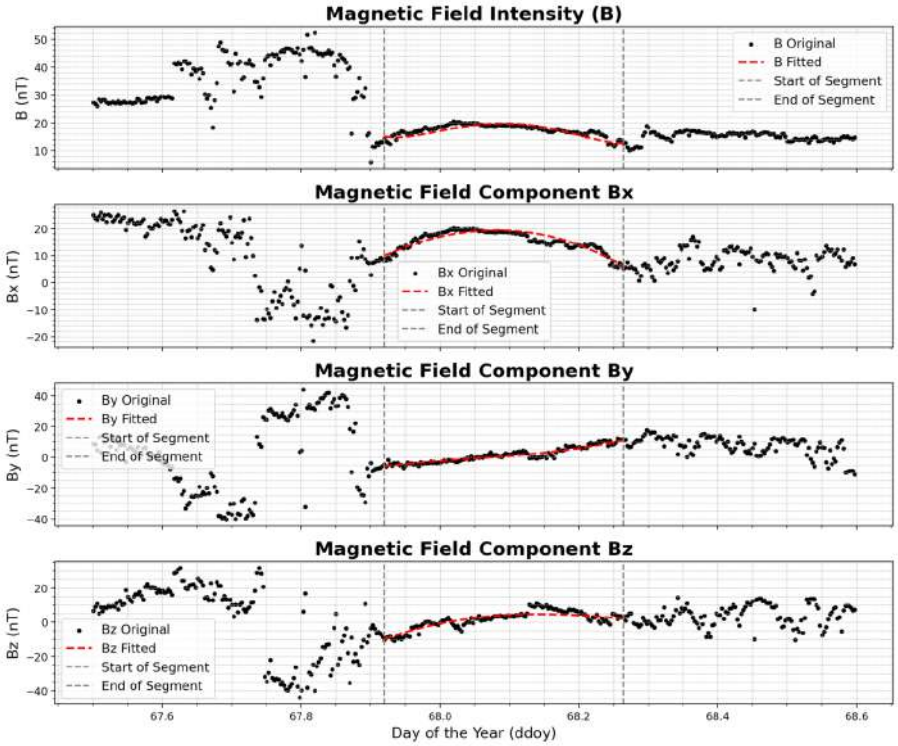

Figure 7.6: Fitting using the radial model, PSP – March 8, 2022

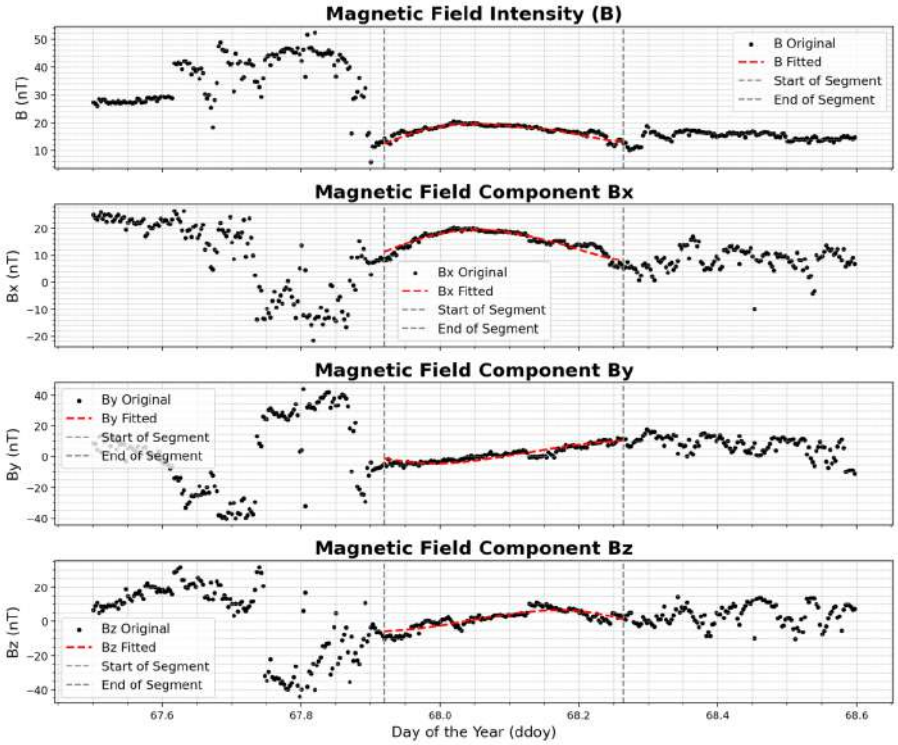

Figure 7.7: Fitting using the radial-poloidal model, PSP – March 8, 2022

In this case, we observe that the fitting quality is quite similar for both models. Specifically, the coefficients of determination for each case are: $R_1^2 = 0.7826$ and $R_2^2 = 0.8228$. The summary of the parameters obtained for the Flux Rope fitting is presented on Table 7.3:

Parameter	Radial Model	Radial–Poloidal Model
z_0	0.75	0.75
θ_x	$-7.33°$	$-51.3°$
θ_y	$-53.63°$	$22.98°$
θ_z	$53.04°$	$-159.12°$
δ	0.68	0.84
θ (XY)	$36.03°$	$35.15°$
ϕ (XZ)	$-34.15°$	$-54.70°$
a (major axis) [AU]	0.0753	0.0716
b (minor axis) [AU]	0.0514	0.0624
R^2	0.7826	0.8228

Table 7.3: Comparison of the fitted parameters for the Model 1 and Model 2, for Event 2.

In this case, we again observe that, despite significant differences in the iterative fitting parameters, the flux rope's final configuration is very similar.

7.2.1 CME Propagation Results

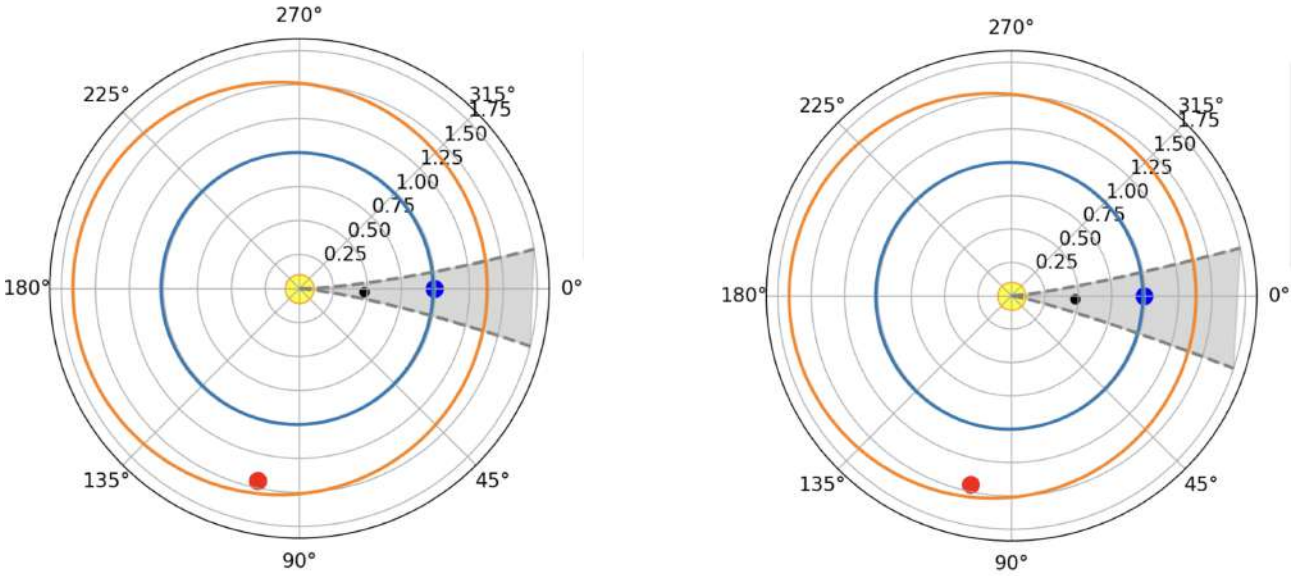

(a) CME Forecast Using Model 1. **(b)** CME Forecast Using Model 2.

Figure 7.8: CME forecast for SO Event, using Model 1 (left) and Model 2 (right).

Key Timestamps	**Model 1**	**Model 2**
Departure From the Sun	2022-03-07 T03:51	2022-03-07 T03:59
Detected by Satellite	2022-03-08 T22:04	2022-03-08 T22:04
Crosses Earth's Orbit	2022-03-10 T23:23	2022-03-10 T23:26
Crosses Mars' Orbit	2022-03-13 T00:09	2022-03-13 T00:16
Satellite and Planetary Positions at their respective Timestamps		
Satellite	$r_1 = 0.477\,\text{AU}$, $\gamma_1 = 3.00°$	$r_1 = 0.477\,\text{AU}$, $\gamma_1 = 3.00°$
Earth	$r_2 = 0.993\,\text{AU}$, $\gamma_2 = 0.00°$	$r_2 = 0.993\,\text{AU}$, $\gamma_2 = 0.00°$
Mars	$r_3 = 1.447\,\text{AU}$, $\gamma_3 = 102.29°$	$r_3 = 1.447\,\text{AU}$, $\gamma_3 = 102.29°$
CME Propagation Details		
Ecliptic Longitude at the Center	2.27°	3.16°
CME Inclination	−46.33°	−35.20°
Angular Width at Earth Distance	(352.90°, 11.64°)	(349.74°, 16.59°)
Angular Width at Mars Distance	(351.14°, 13.39°)	(348.61°, 17.72°)
Encounter with Earth	Yes	Yes
Encounter with Mars	No	No

Table 7.4: Comparison of the CME forecast for the PSP event from August 18th, 2022.

For this second event, we also observe a strong similarity in the calculated key timestamps. In general, when the CME's computed dimensions, internal density, and propagation velocity are very similar, the corresponding timestamp predictions should likewise be very close.

Moreover, in this second event, the angular widths predicted by each model are also quite similar. Both indicate that the collision will occur in a fairly frontal manner, with all indicators pointing to it happening around the end of March 10th.

Next, we will conduct an analysis analogous to that of the previous event to verify whether the prediction is indeed fulfilled.

7.2.2 Validation of Predicted CME Parameters with *WIND* In-Situ Observations

In the figure 7.9 we present the in-situ data detected by WIND between March 9 and 12, 2022.

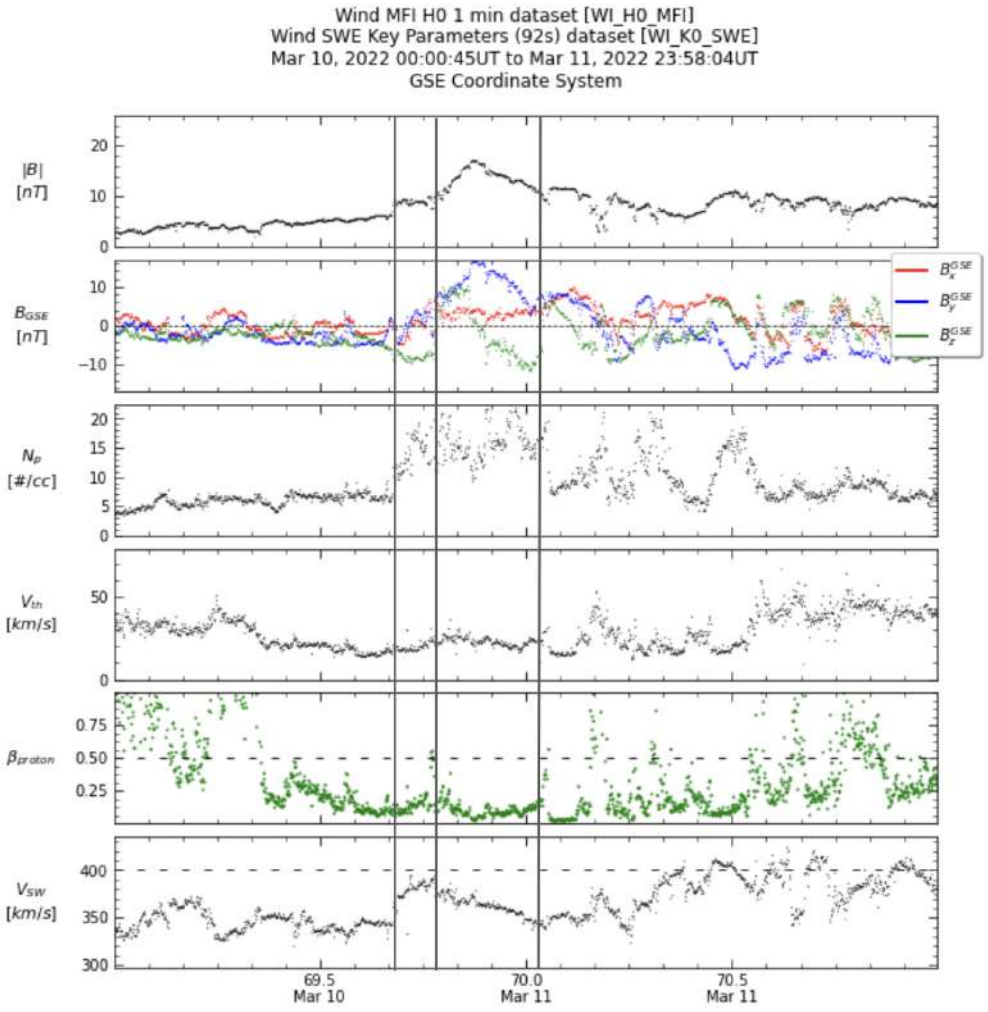

Figure 7.9: WIND data retrieved from the LASSOS catalog [13].

The WIND data analysis reveals that magnetic field disturbances started to appear at 4 PM on

March 10. The shock intensity during this event remains lower than the previous one while the magnetic field reaches its peak value. The β_p parameter shows substantial reduction throughout the studied region during this event. The indicators point to the CME crossing through the central section of the Flux Rope.

The fitting results indicate that the CME would enter Earth's orbit during the night of March 10 at 11 PM. The Flux Rope arrived at WIND at 7 PM during this event which resulted in a prediction error of four hours.

Multiple factors could explain this observed error. The calculations depend on the internal CME structure detection point by satellites which will reach Earth's orbit after a specific time period of 2 days and 1 hour. The CME exists as a non-planar structure because different parts move at different times according to 6.7a. The object's astronomical unit scale size produces time differences of several hours when different parts of the structure reach detection points.

The current model lacks this resolution but implementing it for improved detection timing predictions would be beneficial.

The physical solar wind models demonstrate good accuracy for velocity and density measurements at these distances but advanced models exist which could enhance interplanetary environment modeling.

In conclusion, the CME propagation prediction can be considered fairly accurate. There will always be some margin of tolerance for the results, and it would be a matter of analyzing many events to determine whether systematic errors exist or if, in general, the results align as expected.

Still, even if the error tolerance were around 4 hours, this is significantly better than the current average prediction error obtained from coronagraph-based forecasts. According to a 2024 report, predictions typically have a bias of -2.5 h (on average 2.5 h early), a mean absolute error of 13.2 h, and a standard deviation of 17.4 h [8].

This is because all of their predictions are based on coronagraph data (just after the CME leaves the Sun), but this study shows that if we instead use satellite detections at intermediate positions as the reference point, the predictions can be significantly more accurate.

7.2.3 Validation Conclusions

For the first event, the detection time precision at Earth was very good, with an error of around 1 hour. However, the two models studied provided different conclusions—one predicted a collision with Earth, the other did not. From the in-situ data, it was determined that both scenarios could be possible. The CME impact does not appear to be frontal, but rather lateral (Glancing Blow). However, this could mean either that we are passing through one of the CME's flanks, or that what is being perceived is its sheath. In both cases, the result provides

valuable information, but it would be necessary to apply this study to many more events to determine which better fits reality.

For the second event, it is clearly seen in both the predictions and the subsequent detection that the CME impact is frontal and intersects the contained Flux Rope. However, for this second event, the accuracy of the collision timing prediction was lower, with an error of around 4 hours. Still, this error is relatively small when compared to the errors of predictions based on coronagraphs. Therefore, we conclude that this CME propagation prediction methodology is quite effective and promising.

8. Methodology and Planning

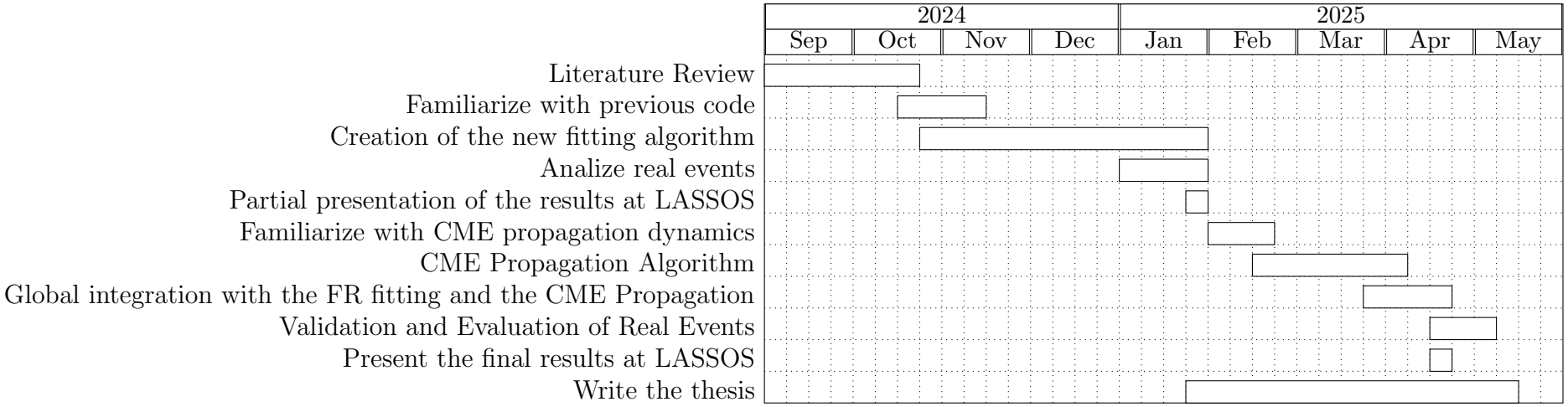

Figure 8.1: Gantt chart showing the planning of the development of this thesis.

9 . Sustainability Report

9.1 Sustainability Matrix

The objective of this chapter is to evaluate the environmental, economic, and social impacts of the development and execution of X-CME, and to identify the main risks and limitations. These aspects are summarized in Table 9.1.

Table 9.1: Thesis Sustainability Matrix

	Thesis Development	**Project Execution**	**Risks and Limitations**
Environmental Perspective	Air travel (two round-trips Spain–USA) and daily commute to NASA Goddard. Laptop use (8 h/day, 6 days/week, Oct 2024–May 2025).	Hosted on existing NASA servers; negligible incremental footprint. Future HPC runs could increase energy use.	Potential spikes in compute demand if higher-resolution physics are added. Monitor energy use and adopt renewable-energy credits.
Economic Perspective	Housing (8 months in DC), car expenses, living costs, and airfare (∼$16 200 total).	Running on institutionally funded NASA infrastructure; no extra operating cost.	Costs could rise if commercial data feeds or premium APIs are required. Seek mixed funding (agency + industry) and periodic budget reviews.

continued on next page

Table 9.1 (continued)

	Thesis Development	Project Execution	Risks and Limitations
Social Perspective	Inclusive, gender-neutral writing; open-source code on GitHub; student training. International collaboration with NASA and UPC.	Democratises access to accurate CME forecasts via web interface; supports research and education.	Misinterpretation of forecasts could erode trust or cause needless operational actions. Ensure clear documentation and user training.

9.1.1 Environmental impact

Development. The single largest source of emissions is air travel: two round-trips from Madrid to Washington DC (economy) produce roughly 3.5 tCO_2, about 78 % of the development footprint. Daily commutes by car (2013 Nissan Altima, 125 g CO_2/km) add approximately 1.0 tCO_2 (22 %). Continuous laptop operation (8 h/day, 6 days/week from Oct 2024 to May 2025) consumes about 107 kWh, yielding $\sim$ 43 kg CO_2 ($<$ 1 %). Total development emissions are therefore $\sim$4.5 tCO_2. Mitigations: consolidate site visits; replace one flight with teleconferencing; use low-emission or public transit for commuting.

Execution. X-CME currently runs on existing NASA heliophysics infrastructure, imposing negligible additional environmental load. If integrated into a real-time forecasting service, the dominant impact will be high-performance-computing cycles, which should be profiled and optimized.

Risks and limitations. Future versions may include finer spatial or temporal resolution, driving up energy use. Continuous monitoring of computational carbon intensity and purchasing renewable-energy credits are recommended to cap the operational footprint.

9.1.2 Economic impact

Development. Total direct expenditure for the thesis is approximately \$16 182: housing \$6 750 (42 %), car costs \$5 082 (31 %), living expenses \$3 150 (20 %), and airfare \$1 200

(7 %). Cost-containment measures included minimizing non-essential travel and leveraging institutionally provided workspace and equipment.

Execution. Current execution on NASA's funded servers incurs no incremental operating cost. Transitioning X-CME to a commercial or service-level environment would introduce annual hosting and maintenance fees.

Risks and limitations. Budget allocations may shift with NASA's priorities, and chartering external data feeds could drive unforeseen expenses. Recommendations: conduct semi-annual cost reviews and pursue blended funding (government grants plus industry partnerships).

9.1.3 Social impact

Development. All thesis materials employ inclusive, gender-neutral language, accessible figures, and publicly available source code to foster transparency and reproducibility. Collaboration with international research centers broadened participation and skill development among students.

Execution. When deployed, X-CME will enable earlier and more accurate space-weather alerts for power operators, airlines, insurers, and satellite mission planners, enhancing societal resilience to CME-driven geomagnetic storms.

Risks and limitations. Overreliance on model outputs without proper user training may lead to misplaced confidence or unwarranted shutdowns. Clear documentation, user tutorials, and continued stakeholder engagement are essential to maintain trust and ensure responsible use.

9.2 Ethical Implications

The X-CME tool presented in this thesis directly addresses the critical need for robust, user-friendly algorithms to fit and forecast CME magnetic structures, a requirement underscored by both heliophysics researchers and satellite operators. By making the fitting routines open-source and deploying them via a Streamlit application, this work promotes transparency and reproducibility in space-weather modeling.

From an ethical standpoint, X-CME adheres to the scientific community's highest standards of rigor and openness: all source code, data-processing steps, and model equations are fully documented and freely available, eliminating barriers posed by proprietary software. Because

the project involves only computational analysis of public in-situ datasets, there are no direct human-subject or environmental interventions, ensuring full compliance with institutional review and data-management policies. Moreover, by enabling more accurate CME arrival-time estimates, X-CME contributes to risk mitigation strategies for satellite operators, power-grid managers, and manned spaceflight planners, ultimately enhancing the safety and reliability of critical technologies without introducing new ethical concerns.

9.3 Relationship with the Sustainable Development Goals

The capabilities developed in this thesis align closely with **SDG 9**: Industry, Innovation and Infrastructure (United Nations). By delivering accessible, high-precision fitting algorithms for CME structures, X-CME supports the resilience of communication and navigation satellites, as well as terrestrial power networks, against extreme solar events. Improved forecasting models reduce the likelihood of service disruptions and expensive hardware replacements, thereby fostering more sustainable technological infrastructures.

In addition, this work touches on **SDG 3**: Good Health and Well-Being by contributing to the protection of human health in high-radiation environments. Accurate CME predictions inform decision-making for astronauts on deep-space missions and for crewed aircraft operating at polar routes, where exposure to solar particle events can exceed safe limits. By enhancing pre-event warnings, X-CME helps operators implement timely safety protocols, mitigating radiation risks and safeguarding human life.

10 . Conclusions

10.1 Flux Rope Structure Reconstruction

To study the reconstruction of magnetic structures in the interplanetary medium, we began by **generalizing the possible physical models** assuming a classical Cylindrical–Ecliptic geometry. In this development, the possibility of a **poloidal dependence was included**, and the constraints that both the magnetic field shapes and the current density field should satisfy for this model to have physical meaning were determined.

The quality of the fits obtained with the classical radial model was compared to those of the radial–poloidal model, and it is observed that the latter provides significantly **better fitting results** due to its added versatility. However, it would be necessary to verify via a milti-point analysis if those predictions are really better or not.

Moreover, a complete **redesign of the classic reconstruction algorithms** was undertaken. It was possible to substantially simplify the number of influential parameters in the minimization processes by separating the resolution of the Flux Rope geometry from that of the internal field. The newly developed iterative method also allowed control over the error tolerance for each parameter and verification that the algorithm always converges.

This algorithm has been implemented in a practical and easy-to-use **Streamlit application**, which produces detailed reports for any selected event in an automated fashion, drawing data from satellites such as WIND, PSP, STEREO, and SOLO.

Additionally, the **fitting algorithm was validated** through its application to **synthetic data**, followed by a **convergence analysis** of the results. It was also used to evaluate **real events**, obtaining values similar to those predicted by other methodologies. To determine which result is better in such cases, a study with more than one observation point would be necessary to verify which model yields the best predictions.

10.2 Study of ICME Propagation

Based on the results obtained from Flux Rope reconstruction, **a new model has been developed to define the structure of an ICME**. This model is based on a tapered torus geometry, and the satellite crossing region is determined using the Flux Rope reconstruction results.

The **interplanetary propagation dynamics of the CME have been solved**, allowing us to define its evolution and velocity throughout the entire interplanetary trajectory, and to predict travel times between various reference points, such as from the Sun's departure until detection by the satellite, or from the satellite to Earth's orbit or Mars' orbit.

The **swept area of the CME within the ecliptic plane** has also been calculated by first computing the intersection with that plane at the satellite detection position, and then using the dynamic propagation models to predict how the swept area will evolve.

Using all obtained results, the positions of Earth and Mars have been calculated for the dates **when the CME is expected to collide** with them, and a collision forecast has been derived.

Finally, this **forecasting process was applied to several real events** from Sun-proximal satellites, showing that the predicted subsequent CME detection occurred with **temporal errors of only 1 to 4 hours** (less than half the current mean error of 13.2 hours obtained just from coronograph predictions).

This entire prediction algorithm has been published as a Streamlit Cloud application under the name **X-CME**, offering a user-friendly and practical interface that allows users to easily obtain results, including the ability to download data from the cloud via the HelioSat module.

11 . Future Work

11.1 Flux Rope Reconstruction

Although the new magnetic field function used yields better fitting results, additional checks are needed to assess whether the physical implications it represents are feasible. For example, one could employ new internal relationships within the Flux Rope by solving its **internal thermodynamics**, or by providing a **more arbitrary geometry** or one better adapted to interplanetary propagation.

One could introduce a more general internal magnetic field by **removing the assumption of no axial dependence of the geometric properties**, allowing for a more dynamic structure with a well-defined expansion process, as well as a potential dynamic model with temporal dependence.

Moreover, one could also apply new **validation methods with multiple point detections** to verify not only the predicted structure of the flux ropes but also the internal magnetic field configuration.

Additionally, **new experimental models of the internal magnetic field** could be implemented to see how they fit the actual values.

11.2 CME Propagation

In the ICME propagation modeling algorithm, certain **size proportions of the CME have been assumed fixed**, and these could later be refined through continuous in-situ evaluation.

The **models used to define the interplanetary medium** are classical models retrieved from [25], but significant advances have recently been made in this field, and it would be very interesting to implement more sophisticated models into this program, particularly for regions closer to the Sun, where the regime changes markedly.

Also, for the moment the X-CME algorithm is designed for forecasts at Earth and Mars, but the process can be extended and could be used to predict whether there will be collisions with

other satellites or other bodies in the solar system.

Finally, the current CME model does not **include its outer envelope**, which is responsible for the initial shocks and adds considerable thickness to the magnetic structure. For collision forecasting, including this envelope could be very useful, not only for adjusting arrival dates but also for defining lateral margins in CME propagation.

In conclusion, without a doubt, the development of this tool still has a long way to go, with many avenues for improvement. It is currently being evaluated by Space Weather experts at NASA GSFC to validate its accuracy, and experts in interplanetary medium modeling are being consulted to implement new, more sophisticated models. It is hoped that this research has been useful and will serve as a foundation for future, more advanced projects, and that the innovations it has introduced will have great potential for future applicability.

Bibliography

[1] S. Bensusen, S. Hill, M. Guhathakurta, and M. Malanoski. Heliophysics and space weather. [URL]. Graphic designers: Sally Bensusen; Steele Hill (Wyle Information Systems). Scientist: Madhulika Guhathakurta (NASA/HQ). Project support: Mark Malanoski (Global Science and Technology, Inc.).

[2] L. F. Burlaga, E. Sittler, F. Mariani, and R. Schwenn. Magnetic clouds in the solar wind. *Journal of Geophysical Research*, 86(A8):6673–6684, 1981. DOI.

[3] S. R. Cranmer, S. E. Gibson, and P. Riley. The origins of the solar wind: progress and problems. *Astrophysical Journal*, Nov. 2017. DOI. [URL].

[4] European Space Agency (ESA). Solar Orbiter. `https://www.esa.int/Science_Exploration/Space_Science/Solar_Orbiter`, . Accessed: 2025-05-08.

[5] European Space Agency (ESA). Solar Orbiter mission image, . [URL].

[6] D. H. Hathaway, M. Adams, J. M. Duncan, and D. E. McKenzie. The solar interior. *NASA/Marshall Solar Physics*, 2025. [URL].

[7] Johns Hopkins University Applied Physics Laboratory. STEREO mission spacecraft image. [URL].

[8] C. Kay, E. Palmerio, P. Riley, M. L. Mays, T. Nieves-Chinchilla, M. Romano, Y. M. Collado-Vega, C. Wiegand, and A. Chulaki. Updating measures of cme arrival time errors. *Space Weather*, 22(7):e2024SW003951, 2024. DOI. [URL].

[9] K. Lang and H. Zirin. Sun. *Encyclopaedia Britannica*, 2025. [URL].

[10] R. P. Lepping, L. F. Burlaga, and J. A. Jones. Magnetic field structure of interplanetary magnetic clouds at 1au. *Journal of Geophysical Research*, 95(A8):11957–11965, 1990. DOI.

[11] S. A. Maloney and P. T. Gallagher. Solar wind drag and the kinematics of interplanetary coronal mass ejections. *The Astrophysical Journal Letters*, 724(2):L127, nov 2010. DOI. [URL].

[12] NASA. Wind Mission Home Page. `https://wind.nasa.gov`. Accessed: 2025-05-08.

[13] NASA Goddard Space Flight Center. LASSO catalogs. https://science.gsfc.nasa.gov/lassos/catalogs.shtml, . Accessed: 2025-05-12.

[14] NASA Goddard Space Flight Center. NSSDC Master Catalog: Wind Probe. https://nssdc.gsfc.nasa.gov, . Accessed: 2025-05-08.

[15] NASA Goddard Space Flight Center. STEREO Mission Page. https://stereo.gsfc.nasa.gov, . Accessed: 2025-05-08.

[16] NASA Science. Coronagraph Image. [URL].

[17] T. Nieves-Chinchilla, M. G. Linton, M. A. Hidalgo, A. Vourlidas, N. P. Savani, A. Szabo, C. Farrugia, and W. Yu. A Circular-Cylindrical Flux-Rope Analytical Model for Magnetic Clouds. *The Astrophysical Journal*, 823(1):27, May 2016. DOI. [URL].

[18] T. Nieves-Chinchilla, M. G. Linton, M. A. Hidalgo, A. Vourlidas, N. P. Savani, A. Szabo, C. J. Farrugia, and W. Yu. A circular–cylindrical flux-rope analytical model for magnetic clouds. *The Astrophysical Journal*, 823(1):27, 2016. DOI. [URL].

[19] T. Nieves-Chinchilla, M. G. Linton, M. A. Hidalgo, and A. Vourlidas. Elliptic-cylindrical Analytical Flux Rope Model for Magnetic Clouds. *The Astrophysical Journal*, 861(2):139, July 2018. DOI. [URL].

[20] T. Nieves-Chinchilla, A. Vourlidas, J. C. Raymond, M. G. Linton, N. Al-haddad, N. P. Savani, A. Szabo, and M. A. Hidalgo. Understanding the Internal Magnetic Field Configurations of ICMEs Using More than 20 Years of Wind Observations. *Solar Physics*, 293 (2):25, Feb. 2018. DOI. [URL].

[21] T. Nieves-Chinchilla, M. A. Hidalgo, and H. Cremades. Distorted–toroidal flux rope model. *The Astrophysical Journal*, 947(1):79, 2023. DOI. [URL].

[22] T. Nieves-Chinchilla, S. Pal, T. M. Salman, F. Carcaboso, S. E. Guidoni, H. Cremades, A. Narock, L. A. Balmaceda, B. J. Lynch, N. Al-Haddad, L. Rodríguez-García, T. W. Narock, L. F. G. Dos Santos, F. Regnault, C. Kay, R. M. Winslow, E. Palmerio, E. E. Davies, C. Scolini, A. J. Weiss, N. Alzate, M. Jeunon, and R. Pujadas. Redefining Flux Ropes in Heliophysics. *Frontiers in Astronomy and Space Sciences*, 10:56, Mar. 2023. DOI.

[23] NOAA Space Weather Prediction Center. Coronal Mass Ejections Phenomenon. [URL].

[24] S. Odenwald. Bringing the sun to light. [URL].

[25] E. R. Priest. *Magnetohydrodynamics of the Sun*. Cambridge University Press, Mar. 2014. [URL].

[26] C. J. Schrijver and G. L. Siscoe. Figure 2.14. https://ars.els-cdn.com/content/image/1-s2.0-B9780128005361000022-f02-14-9780128005361.jpg, 2016. From *Handbook of Space Weather*, Elsevier, 2016.

[27] R. Schwenn. Space Weather: The Solar Perspective. *Living Reviews in Solar Physics*, 3 (1):2, Dec. 2006. DOI.

[28] B. Vršnak, T. Žic, T. V. Falkenberg, C. Möstl, S. Vennerstrom, and D. Vrbanec. The role of aerodynamic drag in propagation of interplanetary coronal mass ejections. *Astronomy & Astrophysics*, Mar. 2010. DOI. [URL].

[29] A. J. Weiss, C. Möstl, T. Amerstorfer, R. L. Bailey, M. A. Reiss, J. Hinterreiter, U. A. Amerstorfer, and M. Bauer. Analysis of coronal mass ejection flux rope signatures using 3dcore and approximate bayesian computation. *The Astrophysical Journal Supplement Series*, 252(1):9, 2021. DOI. [URL].

[30] A. J. Weiss, T. Nieves-Chinchilla, and C. Möstl. Distorted magnetic flux ropes within interplanetary coronal mass ejections. *The Astrophysical Journal*, 2024. [URL]. Draft version June 21, 2024; submitted to ApJ.

[31] Wikipedia contributors. Parker Solar Probe spacecraft model image, . [URL].

[32] Wikipedia contributors. Solar Orbiter. https://en.wikipedia.org/wiki/Solar_Orbiter, . Accessed: 2025-05-08.

[33] Wikipedia contributors. STEREO. https://en.wikipedia.org/wiki/STEREO, . Accessed: 2025-05-08.

[34] Wikipedia contributors. Wind spacecraft probe image, . [URL].

[35] D. R. Williams. Sun fact sheet. *NASA Goddard Space Flight Center*, 2013. [URL].

A . Amount of Mass Consumed by Solar Nuclear Fusion

For purely illustrative purposes, this section justifies the comparison made in the introduction.

The mass of Mount Everest can be estimated by approximating its shape as a circular cone with a base radius $r \approx 10\,\text{km}$ and height $h \approx 8,848\,\text{m}$, assuming a typical rock density of $\rho \approx 2,700\,\text{kg}\,\text{m}^{-3}$.

The volume V of the cone is calculated as follows:

$$V \approx \frac{1}{3}\,\pi\,r^2\,h = \frac{1}{3}\,\pi\,(10,000\,\text{m})^2\,(8,848\,\text{m}) \approx 9.3 \cdot 10^{11}\,\text{m}^3,$$

The mass m is then obtained by multiplying the volume by the density:

$$m = \rho\,V \approx 2.7 \cdot 10^3\,\text{kg}\,\text{m}^{-3} \cdot 9.3 \cdot 10^{11}\,\text{m}^3 \approx 2.5 \cdot 10^{15}\,\text{kg}.$$

Thus, the mass of Mount Everest is on the order of:

$$2 \cdot 10^{15}\,\text{kg} \quad \text{(approx.)}.$$

Assuming the Sun consumes approximately 600 billion kg of hydrogen per second, the time required for the Sun to consume an amount of matter equivalent to the mass of Mount Everest is calculated as follows:

$$2 \cdot 10^{15}\,\text{kg} \cdot \frac{1\,\text{s}}{600 \cdot 10^9\,\text{kg}} \cdot \frac{1\,\text{h}}{3,600\,\text{s}} = 0.9259\,\text{h} \approx 1\,\text{h}. \tag{A.1}$$

B . Determinant of the Metric Tensor

Given the metric tensor in the coordinate system (r, y, φ):

$$g = \begin{pmatrix} a^2(\cos^2\varphi + \delta^2 \sin^2\varphi) & 0 & a^2 r \sin\varphi\cos\varphi(\delta^2 - 1) \\ 0 & 1 & 0 \\ a^2 r \sin\varphi\cos\varphi(\delta^2 - 1) & 0 & a^2 r^2(\sin^2\varphi + \delta^2\cos^2\varphi) \end{pmatrix}$$

We compute the determinant:

$$\det(g) = [a^2(\cos^2\varphi + \delta^2\sin^2\varphi)][a^2r^2(\sin^2\varphi + \delta^2\cos^2\varphi)] - [a^2 r\sin\varphi\cos\varphi(\delta^2 - 1)][a^2 r\sin\varphi\cos\varphi(\delta^2 - 1)]$$

$$= a^4 r^2 \left[(\cos^2\varphi + \delta^2\sin^2\varphi)(\sin^2\varphi + \delta^2\cos^2\varphi) - \sin^2\varphi\cos^2\varphi(\delta^2 - 1)^2\right]$$

Simplify the expression inside the brackets:

$$(\cos^2\varphi + \delta^2\sin^2\varphi)(\sin^2\varphi + \delta^2\cos^2\varphi) - \sin^2\varphi\cos^2\varphi(\delta^2 - 1)^2$$

$$= \delta^2(\cos^4\varphi + \sin^4\varphi + 2\sin^2\varphi\cos^2\varphi) = \delta^2 \cdot 1 = \delta^2$$

Thus:

$$\det(g) = a^4 r^2 \delta^2$$

Therefore:

$$\boxed{\sqrt{\det(g)} = a^2\, r\, \delta} \tag{B.1}$$

C . Correction to apply for the Circular Cylindrical Model

The distances and angles involved when crossing the section are the following:

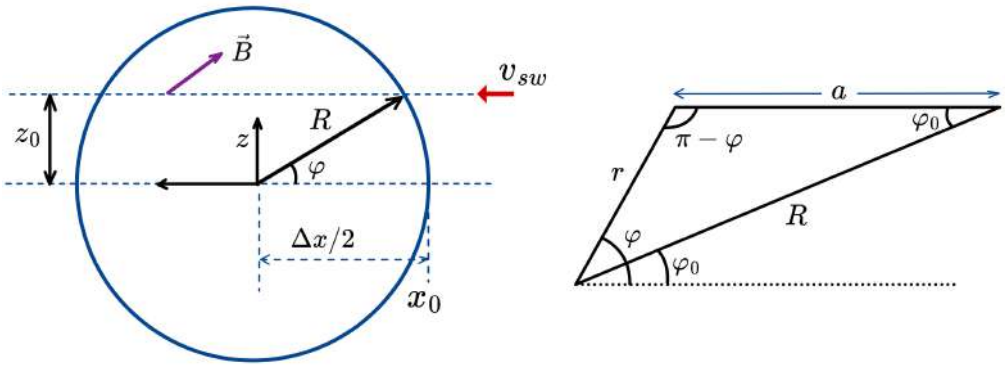

Figure C.1: Scheme of the cut in a section of the MO

The system can be described as follows:

$$\Delta x = v_{sw} t_s \qquad \bar{z}_0 = z_0/R \qquad \varphi_{sat_0} = arctg\left(\frac{z_0}{x_0}\right)$$

However, as the cylinder is not necessarily perpendicular to the satellite's trajectory, and its rotation angles, θ and Φ, will cause the section perceived by the spacecraft upon entering the cylinder to be an ellipse rather than a circle.

This can be interpreted as a distortion of the coordinates at the point of entry, but the correction for this is straightforward.

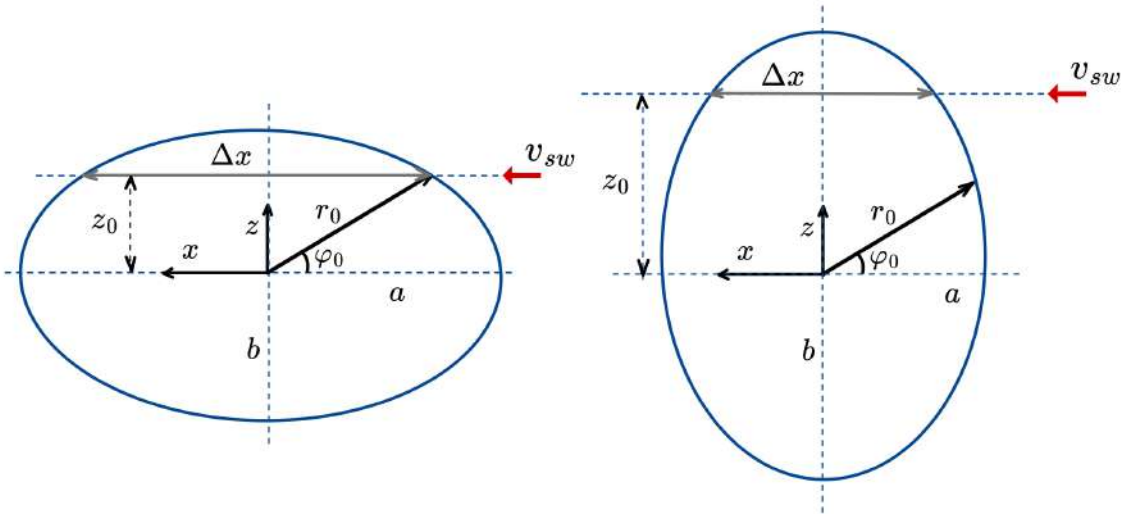

Figure C.2: Distortion of the entrance section.

It is observed that an increase in the angle θ generates a distortion in the vertical lengths (the b axis increases in size), while an increase in the angle Φ distorts the ellipse horizontally.

In the case of horizontal distortion, all vertical lengths will retain their magnitude, but the horizontal lengths will be rescaled by a factor of $cos\Phi$ in division.

A similar phenomenon will occur with vertical distortion. In this case, the horizontal components will remain unchanged, but the vertical components will be rescaled by a factor of $cos\theta$ in division.

Therefore, in the combined case, it will be necessary to rescale the vertical and horizontal components with their corresponding scaling factors.

$$\varphi_0 = arctg\left(\frac{z_0/cos\theta}{x_0/cos\Phi}\right) = arctg\left(\frac{2\bar{z}_0\, R\, cos\Phi}{v_{sw}t_s cos\theta}\right) \tag{C.1}$$

$$r_0 = \frac{v_{sw}t_s}{2cos\varphi_0} \tag{C.2}$$

$$\frac{x_0^2}{a^2} + \frac{z_0^2}{b^2} = 1 \Rightarrow a = \frac{x_0}{\sqrt{1-\frac{z_0^2}{b^2}}} = \frac{R}{cos\Phi} \Rightarrow \boxed{R = cos\Phi \frac{v_{sw}t_s}{\sqrt{1-\bar{z}_0^2}}} \tag{C.3}$$

However, the satellite's trajectory is defined by a, and we need to express a as a function of φ and r. To do so, we will use the cosine theorem and the sine theorem:

◇ **Cosine Theorem:** $r^2 = a^2 + R^2 - 2aR\,\cos(\varphi_0)$

◇ **Sine Theorem:** $\frac{a}{\sin(\varphi - \varphi_0)} = \frac{r}{\sin(\varphi_0)}$

By substituting and simplifying, we obtain the following expression:

$$r^2 \left[\left(\frac{sin(\varphi - \varphi_0}{sin\varphi_0} \right)^2 - 1 \right] + 2R\,cos(\varphi - \varphi_0) \cdot r = R^2 \;\Rightarrow\; r = r(\varphi) \tag{C.4}$$

At the moment of the section cut, the spacecraft follows the trajectory defined by a. However, what we want is to express it in terms of the polar variables φ and r. Let us now examine the relationship these variables have with a:

$$\frac{x_0^2}{a^2} + \frac{z_0^2}{b^2} = 1 \Rightarrow a = \frac{x_0}{\sqrt{1 - \frac{z_0^2}{b^2}}} = \frac{R}{cos\Phi} \Rightarrow \boxed{R = cos\Phi \frac{v_{sw} t_s}{\sqrt{1 - \bar{z}_0^2}}} \tag{C.5}$$

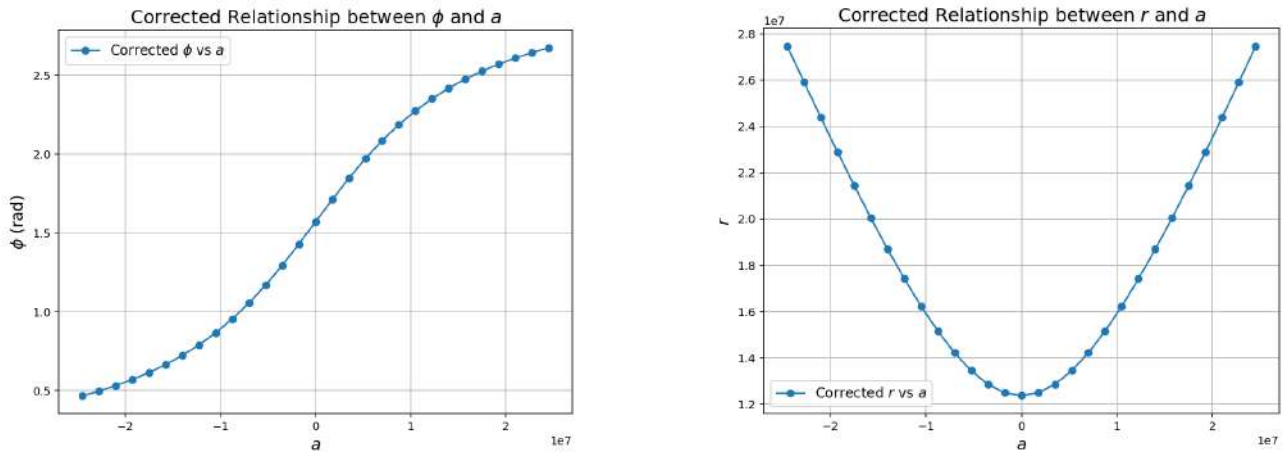

Figure C.3: Dependencies of $\varphi(a)$ and $r(a)$ for $\varphi_0 = \pi/4$

in particular, working with the previous expressions for the Sinus Theorem and Cosinus Theorem, we get to:

$$a = \frac{sin(\varphi - \varphi_0)}{sin(\varphi_0)} \sqrt{a^2 + R^2 - 2aR\,cos(\varphi_0)} \;\Rightarrow\; a = a(\varphi) \tag{C.6}$$

With these relationships, we would now have the necessary arrays to perform the coordinate transformation from GSE to cylindrical and vice versa.